2009

In situ High-pressure Study of Hydrogen Storage Materials by Vibrational Spectroscopy

Shuntai Xie

In situ High-pressure Study of Hydrogen Storage Materials by Vibrational Spectroscopy

(Spine Title: High Pressure Study of Hydrogen Storage Materials)

(Thesis Format: Integrated-Article)

by

Shuntai Xie

Graduate Program in Chemistry

A thesis submitted in partial fulfillment
of the requirements for the degree of
Master of Science

School of Graduate and Postdoctoral Studies
The University of Western Ontario
London, Ontario, Canada

Abstract

Pressure-induced structural transformations of two potential hydrogen storage materials, i.e., ammonia borane ($NH_3 \cdot BH_3$) and calcium borohydride [$Ca(BH_4)_2$] were investigated in diamond anvil cells by Raman and IR spectroscopy at ambient temperature up to 14 GPa and 10 GPa, respectively. By monitoring the profile evolutions of Raman and IR modes as well as changes of pressure coefficients, ammonia borane and calcium borohydride were found to undergo several phase transitions upon compression. Decompression measurements suggest those pressure-induced phase transitions were reversible for both materials. Structures of the new phases at different pressure ranges were analyzed based on our Raman and IR data. Our work on ammonia borane complements previous high pressure study on this material by providing new information on the structures and stabilities, while that on calcium borohydride constitutes the first high-pressure experimental study.

Keywords

High pressure · Hydrogen storage materials · Vibrational spectroscopy · Diamond anvil Cell · Ammonia borane · Calcium borohydride

The Co-authorship Statement

I hereby declare that this thesis incorporates material that is result of collaborative research, as follows: Chapter 2 of this thesis incorporates the outcome of a collaborative research with Dr. Zhenxian Liu, a beamline scientist at U2A of the National Synchrotron Light Source, Brookhaven National Laboratory. His contribution as a co-author was primarily through the provision of synchrotron IR system and technical supports for IR experiments. For Chapter 3, an undergraduate student S. Dabiran-Zohoory performed the preliminary experiments based on which I performed the synthesis and bulk spectroscopic measurements. In both cases, the key ideas, primary contributions, experimental designs, data analysis and interpretation, and writing were performed by me.

I am aware of the University of Western Ontario Policy on Authorship and I certify that I have properly acknowledged the contribution of other researchers to my thesis.

I certify that, with the above qualification, this thesis, and the research to which it refers, is the product of my own work.

Acknowledgement

First and foremost, I would like to thank my supervisor Dr. Yang Song for leading me into this field. Thanks for all his invaluable support, encouragement and suggestions throughout the past two years. His continuous guidance enabled me to complete my work successfully. I have furthermore to thank Dr. Robert H. Lipson and Dr. Nicholas C. Payne, for their teaching and help in and outside their courses.

I would also like to thank all the members of the Song group, especially Zhaohui, who helped me with the first measurement in my project.

Special thanks to my friends and classmates. It is you who drive the loneliness away from me and leave a happy and memorable time to me.

Finally I would thank my parents for their love, understanding and support throughout the years.

Table of Contents

List of Figures

List of Tables

List of Abbreviations

Atm	Atmosphere
asym.	Asymmetric
CCD	charge-coupled device
cm^{-1}	Wavenumber
DAC	diamond anvil cell
Fig.	Figure
GPa	Gigapascal
INS	inelastic neutron scattering
IR	Infrared
Mm	Millimeter
MPa	Megapascal
Mrad	Milliradian
Nm	Nanometer
Ppm	parts per million
sym.	Symmetric
THF	Tetrahydrofuran
Mm	Micrometer

Chapter 1 Introduction

1.1 Hydrogen economy and hydrogen storage

1.1.1 Hydrogen economy

Since industrial revolution, human being has been greatly consuming fossil fuels without too much thinking about the environmental impacts and possible consequences. The major problem of using fossil fuels is global warming, which causes dangerous climate changes and leads to higher cardiovascular mortality and more frequent outbreaks of infectious disease.[1-2] To meet increasing global demands for energy and to allow for the depletion of fossil fuel supplies in the coming years, alternative "clean" energy sources, which can be regenerated and which have a tolerable environment impact, should be developed.

Hydrogen, as it has the highest energy density per mass of all chemical fuels[3] with little emissions of CO_2, NO_x or SO_x and can carry energy almost without any loss during long distance transportation, is a good candidate as an energy source for both on-board and stationary applications.[4] Through combination with oxygen in a fuel cell, hydrogen can be used to provide electricity, with water being its only byproduct. Also, hydrogen can be burned in an internal combustion engine in the same way as gasoline or natural gas, providing 8% higher efficiency than that by gasoline.[5]

Although in many ways hydrogen is an attractive alternative for fossil fuels, the realization of "hydrogen economy",[6-8] in which energy is mainly stored and transported using hydrogen, still faces many challenges. For example, today, nearly half of the hydrogen produced in the world is derived from natural gas via a steam-reforming process, during which CO and CO_2 are generated as the byproduct. To eliminate the high level of greenhouse gas emissions associated with using natural gas, in the future, hydrogen needs to be produced from renewable energy sources. Meanwhile, the currently

relatively high cost of hydrogen production and transportation also impedes the widespread use of hydrogen.

1.1.2 Hydrogen storage

Among the prominent issues in the hydrogen economy, efficient hydrogen storage, which flexibly links the production of hydrogen and its eventual use, is particularly a challenging one. Conventionally, hydrogen can be stored as compressed gas in high-pressure gas canisters (up to 800 bar) or as liquid in cryogenic tanks (at ~21 K).[3] However, high-pressure gaseous H_2 storage is limited by the weight of the storage canisters and the potential of developing leaks. In addition, near 40 % of the heating value of hydrogen is required for liquefaction and maintaining the cryogenic state for liquid-hydrogen storage. Moreover, storage of hydrogen in liquid or gaseous forms poses important safety problems for on-board applications. Instead, the situation has prompted an extensive effort to develop a considerably safe way to store hydrogen in solid hydrogen storage materials.[9] To promote this type of research, the US Department of Energy (DOE) has set ambitious goals for hydrogen storage applications, e.g., by 2015, a gravimetric density of 9.0 wt % H and a volumetric density of 82 g $H{\cdot}L^{-1}$ should be reached.[10]

Currently, solid hydrogen storage materials include carbon-based materials, metal hydrides, chemical hydrides and complex hydrides, etc.[11] The storage of hydrogen in carbon-based materials, such as activated carbons and carbon nanotubes, takes the advantage of the highly effective porosity of carbon structure at ambient pressure and room temperature.[12] The reported hydrogen storage capacity for carbon materials ranges from 0.2 to 10 wt % H.[13-18] However, the experiments claiming high hydrogen densities[13-14] have not been independently repeated by other laboratories.

By reacting with metal elements or alloys (e.g., Mg and Al), hydrogen can be stored in forms of metal hydrides (e.g., MgH_2 and AlH_3). Generally, metal hydrides are composed of metal atoms that constitute a host lattice and hydrogen atoms that are

trapped in interstitial sites, such as lattice defects. The formation of metal hydrides is typically exothermic and hydrogen can be desorbed under certain temperature and pressure conditions.[19-20]

Unlike carbon materials and metal hydrides, chemical hydrides (e.g., $NH_3 \cdot BH_3$ and B_2H_6) generally require a chemical reaction pathway to be regenerated. Therefore they could not be directly refueled with hydrogen on a vehicle.

Complex hydrides, such as alanates and metal borohydrides, are another kind of hydrogen storage materials.[21] They were not considered for hydrogen storage since they were regarded to be irreversible until recently when the reversible dehydration of $NaAlH_4$ by doping with a Ti catalyst was discovered by Bogdanovic.[22] Since then, the development of complex hydrides has become the focus of many studies.[23-29]

More recently, development of hydrogen storage materials by high pressure has received increasing attention.[30] In the following sections, general principles of high pressure and its application on the production of potential hydrogen storage materials are discussed.

1.2 High pressure science and technology

1.2.1 High pressure phenomena

As one of the three fundamental thermodynamic parameters, pressure is of vital importance in physics and chemistry. Pressure spans over 60 orders of magnitude in the universe. However, its study has been limited to relatively low pressure gaseous systems until decades ago when adequate high-pressure technologies, such as diamond anvil cell,[31] were invented. Since then, high pressure studies have entered into a new exciting and prosperous era. Currently, static high pressures in excess of 300 GPa (1 GPa = 10^9 Pa = 10,000 atm), a pressure close to that in the earth core (~330–360 GPa), have been achieved in some laboratories.[32]

Free energy change in materials can be as high as 10 eV under extreme compression, far exceeding the energy of the strongest chemical bond.[32] Consequently, bonding properties and bonding patterns established for materials at ambient pressure can be greatly altered by high pressure. Under high-pressure conditions, materials are driven to a state with lower volume, which leads to an interruption of intra- or inter-molecular interactions and therefore stabilities of materials. As the effective volume occupied by the constituent particles is reduced, the structure of crystal may be altered, resulting in phase transitions. As a result, novel functional materials, such as superhard material and high temperature superconductor, can be formed under high pressure by means of chemical reactions or via mechanisms that are significantly different from those at ambient pressure. Moreover, high pressure serves as an important means to carefully tune electronic, magnetic, optical and mechanical properties for testing fundamental theory and a wide range of new applications.[33]

1.2.2 Diamond anvil cell technology

Of all the advances in high pressure technology, that involving diamond anvil cell (DAC), a device to generate and maintain static high pressure, is perhaps the most significant one that has led to a massive explosion of high pressure studies. The predecessor of modern DAC is the Bridgman anvil device invented by Bridgman in the 1940s. In the Bridgman anvil device, an opposing-anvil configuration which is now widely used in DAC, was first employed. Based on that configuration, modern DAC in which diamonds were used as anvils was developed by Weir and his colleagues in the National Bureau of Standards. Diamonds are used because they are the hardest material known in nature, and therefore could sustain very high pressure. In addition diamonds are transparent to a broad spectral range, and thus their use would facilitate the structural characterization of materials under high pressure by various probes such as infrared (IR) and X-ray diffraction (XRD). Based on the kinds of probe used, different types of diamond can be chosen. Type II diamonds which only have IR absorption around 2000

cm^{-1} are employed in IR measurements, while less costly type I (with higher impurity, e.g., nitrogen) diamonds are widely used in Raman and XRD measurements.

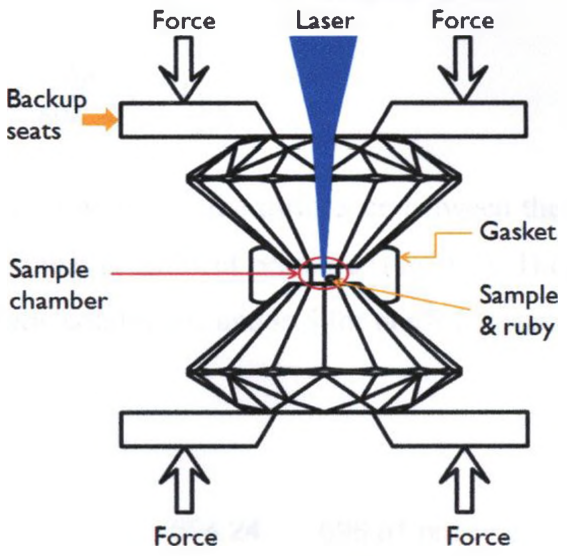

Fig. 1.1. General schematics of a symmetric diamond anvil cell. The force is applied symmetrically via a screw system.

Today many types of DACs are custom designed or specially made by various laboratories according to requirements of experiments, such as symmetric DAC and Merrill-Bassett type DAC. The schematic of a symmetric DAC is shown in Fig. 1.1. A pair of diamonds the main part of the DAC is placed between two supporting anvils. A pre-indented gasket with a hole drilled in the center serves as sample chamber, and is placed between the two diamonds. Once a small force is applied onto DAC, the backup seats will generate a pressure that is amplified by the shape of the diamond, yielding a high pressure on the diamond tip and an even higher pressure in the gasket and sample. The pressure can be calibrated by the ruby gauge described below.

1.2.3 The ruby pressure gauge

A precise and reliable way to determine the pressure inside a DAC is important

for all high-pressure experiments. Based on Mao's work,[34] pressure in DAC can be determined by measuring ruby (α-Al_2O_3 doped with Cr^{3+}) fluorescence spectra (Fig. 1.2) with an accuracy of ± 0.05 GPa using the following equation:[34]

$$P = \frac{1904}{B}\left[(1+\frac{\Delta\lambda}{694.24})^{B} - 1\right] \tag{1.1}$$

where P is pressure in GPa and $\Delta\lambda$ is the difference between the wavelength of the ruby R_1 line at pressure P and that at ambient pressure (Fig. 1.2). The parameter B is equal to 7.665 for quasi-hydrostatic conditions, and is 5 for non-hydrostatic conditions.

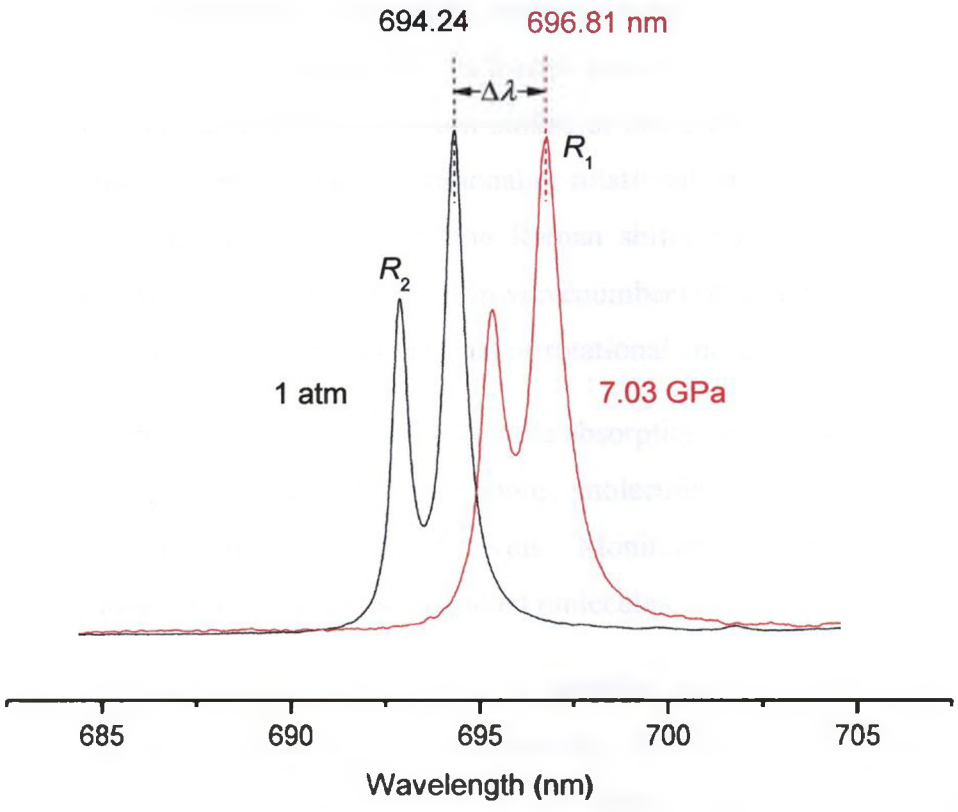

Fig. 1.2. Ruby fluorescence spectra at 1 atm (in black) and at 7.03 GPa (in red) at room temperature. Positions of R_1 fluorescence lines are labeled with dash lines.

1.2.4 High-pressure vibrational spectroscopy

Due to the wide spectral transparency of diamonds, different types of radiations are accessible to samples loaded in DACs. The two most commonly used methods for spectroscopic characterizations under high pressure *in situ* are Raman and IR spectroscopy.[35] They both are used to study the vibrations of various materials.[36]

Raman spectroscopy relies on the scattering of monochromatic light, usually from a laser in visible, near infrared, or near ultraviolet range. When a beam of laser is shining on the sample, some laser photons will be scattered during interactions with atoms or molecules in the sample. Most of the scattering photons, which we referred as Rayleigh scatterings, have the same frequency as the incident beam and therefore carry no spectroscopic information. Meanwhile, some photons are scattered with frequencies higher or lower than the incident beam; the former are referred to as anti-Stokes while the latter are called Stokes. Energies between stokes or anti-stokes and the incident beams fall into the gaps between different vibrational or rotational energy levels of the molecule in sample. Thus, the measurement of the Raman shifts (energy differences between Stokes/anti-Stokes and the incident beam in wavenumber) of a sample provides valuable spectroscopic information for the vibrational or rotational energy levels of that sample.

IR spectroscopy is mainly based on the absorption of the incident infrared beam in molecules. By absorbing infrared phonons, molecules will be excited to various discrete vibrational or rotational energy levels. Monitoring the absorption can lead to spectroscopic data for the vibrations of studied molecules.

Vibrational spectra can be used to monitor structural changes under high pressure and pressure-induced phase transitions. By plotting the Raman shift or wavenumber as a function of pressure, one can identify possible phase transitions. If there is a distinct change of pressure coefficient (slope of the Raman shift or wavenumber as a function of pressure) among different pressure regions, it suggests a phase transition exists between these pressure regions.

1.3 High pressure studies of hydrogen storage materials

The technological developments in high pressure materials research have allowed the synthesis and characterization of novel hydrogen storage materials under high pressures *in situ*. For instance, although some hydrogen storage materials (i.e., MgH_2) have high hydrogen contents, their hydrogenation and dehydrogenation kinetics are very slow, thus usually requiring high operation temperatures. As a result, their potential practical uses are greatly hindered. Using high-pressure technology, new hydrogen storage materials with improved hydrogenation or dehydrogenation properties were synthesized. For example, by reacting a mixture of MgH_2 with Cr (3:1 in molar ratio) in a multi anvil device at 873 K and 8 GPa for 1 to 5 hours, Kyoi *et al.* successfully synthesized Mg_3CrH_x hydride.[37] The dehydrogenation temperature of synthesized Mg_3CrH_x hydride is near 598 K, which is about 150 K lower than that of MgH_2. Similarly, other hydride systems with lower dehydrogenation temperatures, such as Mg-M systems (M = Li, Pd),[38] Ca-Mg-Ni systems,[39] and Mg-TM systems (TM = Ti – Zn),[40] were also developed.

In addition to metal hydride and complex hydride, recent studies showed that hydrogen can also be stored in some crystalline molecular compounds using high pressure technology. For instance, Mao[30] compressed a mixture of H_2 and H_2O to around 180 – 220 MPa (1 MPa = 10^6 Pa = 10 atm). Upon cooling to near 249 K, a hydrogen clathrate hydrate in which a large amount of H_2 is trapped within the crystal structure of H_2O was formed. This synthestic hydrogen clathrate hydrate was found to hold 50 $g \cdot L^{-1}$ hydrogen or 5.3 wt %, and can be preserved at ambient pressure up to 145 K. Besides hydrogen clathrate hydrate (H_2-H_2O system), other hydrogen-molecular systems, such as H_2-CH_4 system,[41] H_2-SiH_4 system,[42] were also prepared.

Not only could hydrogen storage materials be synthesized under high pressure, they could also exhibit structural evolutions (e.g., phase transition) upon compression or decompression. For example, $LiBH_4$, a high hydrogen content hydride, crystallizes in space group *Pnma* at ambient pressure. Upon compression to 1.2 GPa, a phase transition

was observed associated with a 6.6% volume collapse.[43] Starting at 10 GPa, $LiBH_4$ undergoes another phase transition to a new structure with space group $Fm\bar{3}m$.[43] By X-ray diffraction and neutron diffraction spectroscopy, phase transitions of other hydrides, such as MgH_2,[44] BaH_2,[45] α-AlH_3,[46] ErH_3,[47] $NaBH_4$,[48] $Mg(BH_4)_2$,[23] and $ErMn_2H_{4.6}$,[49] were also identified. Although all phase transitions of $LiBH_4$ were found to be fully reversible, the reversibility varies significantly for other hydrides. For example, the transition of $Mg(BH_4)_2$ at 14.4 GPa is reversible while the one between 2.4 and 3.3 GPa was found completely irreversible.[23] The stability and reversibility of potential hydrogen storage materials are important factors that profoundly affect their hydrogen storage capacity. In the case where the detailed crystal structure information is lacking, their pressure behaviors have been efficiently monitored by means of Raman and IR spectroscopy.[50-54] In addition, using first-principles calculations, high pressure structures and their stabilities have been predicted theoretically for some hydrides.[48,55-56] Overall, high pressure has been proven as a powerful driven force for the production of novel structures with strong promises for hydrogen storage applications.

1.4 Motivation and thesis structure

The development of efficient hydrogen storage materials is a key to the final success of using hydrogen as an efficient clean fuel. Ammonia borane ($NH_3{\cdot}BH_3$) and calcium borohydride ($Ca(BH_4)_2$) are two promising hydrogen storage materials whose hydrogen contents (i.e., 19.6 wt % H and 9.7 wt %, respectively) exceed the 2015 U.S. Department of Energy target for on-board hydrogen storage system. There have been extensive studies on the structures, reactivities as well as hydrogen storage capacities at ambient pressure. However, there exist only a few works on their behaviors under high pressure.[52,57] Understanding the structures, stabilities as well as modifications of $NH_3{\cdot}BH_3$ and $Ca(BH_4)_2$ with pressure not only can help us to understand structural relationships in hydrogen storage materials, but also can extend our knowledge to design new hydrogen storage materials.

The theme of this thesis is to study the behavior of $NH_3 \cdot BH_3$ and $Ca(BH_4)_2$ under high pressure using DAC technology by Raman and IR spectroscopy. Interesting and novel pressure-induced phase transitions were observed and possible structures, stability and reversibility of $NH_3 \cdot BH_3$ and $Ca(BH_4)_2$ under high pressure are discussed in Chapter 2 and Chapter 3, respectively. The $NH_3 \cdot BH_3$ work has been published in the Canadian Journal of Chemistry **2009**, *87*, 1235, while the $Ca(BH_4)_2$ work will be submitted to Journal of Physical Chemistry C. In addition, concurrent with the manuscript preparation, we obtained some higher quality IR data using a local FTIR spectrometer. We also conducted X-ray diffraction measurements at a synchrotron facility at HPCAT of advanced photon source of Argonne National Lab. The IR spectra and X-ray patterns are reported in Appendices as supplement. Finally, in Chapter 4, my works are summarized and future work is discussed.

1.5 References

(1) Patz, J. A.; Campbell-Lendrum, D.; Holloway, T.; Foley, J. A. *Nature* **2005**, *438*, 310.

(2) Patz, J. A.; Hulme, M.; Rosenzweig, C.; Mitchell, T. D.; Goldberg, R. A.; Githeko, A. K.; Lele, S.; McMichael, A. J.; Le Sueur, D. *Nature* **2002**, *420*, 627.

(3) Zuttel, A. *Naturwissenschaften* **2004**, *91*, 157.

(4) Masel, R. *Nature* **2006**, *442*, 521.

(5) Berger, E. In *BMW Clean Energy. CARB ZEV Technology Symposium* 2006, p 12.

(6) Bockris, J. O. M. *Science* **1972**, *176*, 1323.

(7) Ames, A. E. *Sciences* **1991**, *31*, 55.

(8) Bockris, J. O. M. *Int. J. Hydrogen Energ.* **2002**, *27*, 731.

(9) Graetz, J. *Chem. Soc. Rev.* **2009**, *38*, 73.

(10) Satyapal, S.; Petrovic, J.; Read, C.; Thomas, G.; Ordaz, G. *Catal. Today* **2007**, *120*, 246.

(11) Schlapbach, L.; Zuttel, A. *Nature* **2001**, *414*, 353.

(12) Darkrim, F. L.; Malbrunot, P.; Tartaglia, G. P. *Int. J. Hydrogen Energ.* **2002**, *27*, 193.

(13) Dillon, A. C.; Jones, K. M.; Bekkedahl, T. A.; Kiang, C. H.; Bethune, D. S.; Heben, M. J. *Nature* **1997**, *386*, 377.

(14) Chambers, A.; Nemes, T.; Rodriguez, N. M.; Baker, R. T. K. *J. Phys. Chem. B* **1998**, *102*, 2251.

(15) Liu, C.; Fan, Y. Y.; Liu, M.; Cong, H. T.; Cheng, H. M.; Dresselhaus, M. S. *Science* **1999**, *286*, 1127.

(16) Liu, C.; Cheng, H. M. *J. Mater. Sci. Technol.* **2002**, *18*, 124.

(17) Chen, Y.; Shaw, D. T.; Bai, X. D.; Wang, E. G.; Lund, C.; Lu, W. M.; Chung, D. D. L. *Appl. Phys. Lett.* **2001**, *78*, 2128.

(18) Liu, C.; Yang, Q. H.; Tong, Y.; Cong, H. T.; Cheng, H. M. *Appl. Phys. Lett.* **2002**, *80*, 2389.

(19) Grochala, W.; Edwards, P. P. *Chem. Rev.* **2004**, *104*, 1283.

(20) Imamura, H.; Masanari, K.; Kusuhara, M.; Katsumoto, H.; Sumi, T.; Sakata, Y. *J Alloy. Compd.* **2005**, *386*, 211.

(21) Marrero-Alfonso, E. Y.; Beaird, A. M.; Davis, T. A.; Matthews, M. A. *Ind. Eng. Chem. Res.* **2009**, *48*, 3703.

(22) Bogdanovic, B.; Schwickardi, M. *J. Alloy. Compd.* **1997**, *253*, 1.

(23) George, L.; Drozd, V.; Saxena, S. K.; Bardaji, E. G.; Fichtner, M. *J. Phys. Chem. C* **2009**, *113*, 486.

(24) Mao, J. F.; Yu, X. B.; Guo, Z. P.; Liu, H. K.; Wu, Z.; Ni, J. *J. Alloy Compd.* **2009**, *479*, 619.

(25) Cakanyildirim, C.; Guru, M. *Renew. Energ.* **2009**, *34*, 2362.

(26) Blanchard, D.; Shi, Q.; Boothroyd, C. B.; Vegge, T. *J. Phys. Chem. C* **2009**, *113*, 14059.

(27) Choudhury, P.; Bhethanabotla, V. R.; Stefanakos, E. *J. Phys. Chem. C* **2009**, *113*, 13416.

(28) Yu, X. B.; Shi, Q.; Vegge, T.; Grant, D. M.; Walker, G. S. *Scripta. Mater.* **2009**, *61*, 359.

(29) Cento, C.; Gislon, P.; Prosini, P. P. *Int. J. Hydrogen Energ.* **2009**, *34*, 4551.

(30) Mao, W. L.; Mao, H. K.; Goncharov, A. F.; Struzhkin, V. V.; Guo, Q. Z.; Hu, J. Z.; Shu, J. F.; Hemley, R. J.; Somayazulu, M.; Zhao, Y. S. *Science* **2002**, *297*, 2247.

(31) Weir, C. E.; Lippincott, E. R.; Vanvalkenburg, A.; Bunting, E. N. *J. Res. Nbs. a Phys. Ch.* **1959**, *63*, 55.

(32) Hemley, R. J.; Mao, H. K. *In High-Pressure Phenomena,* Proceedings of the International School of Physics Enrico Fermi, Vol. 147; Hemeley, R. J., Chiarotti, G. L., Bernasconi, M., Ulivi, L., Eds.; IOS Press: Amsterdam, 2002.

(33) Hochheimer, H. *Frontiers of high pressure research II: application of high pressure to low-dimensional novel electronic materials*; Kluwer Academic Publishers: New York, 2001.

(34) Mao, H. K.; Xu, J.; Bell, P. M. *J. Geophys. Res-Solid.* **1986**, *91*, 4673.

(35) Ferraro, J. R. *Coord. Chem. Rev.* **1979**, *29*, 1.

(36) Gardiner, D.; Graves, P.; Bowley, H. *Practical Raman Spectroscopy*; Springer-Verlag: New York, 1989.

(37) Kyoi, D.; Ronnebro, E.; Kitamura, N.; Ueda, A.; Ito, M.; Katsuyama, S.; Sakai, T. *J. Alloy. Compd.* **2003**, *361*, 252.

(38) Goto, Y.; Kakuta, H.; Kamegawa, A.; Takamura, H.; Okada, M. *J. Alloy. Compd.* **2005**, *404*, 448.

(39) Takamura, H.; Kakuta, H.; Goto, Y.; Kamegawa, A.; Okada, M. *Mater. Trans.* **2001**, *42*, 1301.

(40) Watanabe, H.; Goto, Y.; Kakuta, H.; Kamegawa, A.; Takamura, H.; Okada, M.; *Mater. Trans.* **2004**, *45,* 1350.

(41) Somayazulu, M. S.; Finger, L. W.; Hemley, R. J.; Mao, H. K. *Science* **1996**, *271*, 1400.

(42) Strobel, T. A.; Somayazulu, M.; Hemley, R. J. *Phys. Rev. Lett.* **2009**, *103*.

(43) Filinchuk, Y.; Chernyshov, D.; Nevidomskyy, A.; Dmitriev, V. *Angew. Chem. Int. Edit.* **2008**, *47*, 529.

(44) Vajeeston, P.; Ravindran, P.; Hauback, B. C.; Fjellvag, H.; Kjekshus, A.; Furuseth, S.; Hanfland, M. *Phys. Rev. B* **2006**, *73*.

(45) Smith, J. S.; Desgreniers, S.; Tse, J. S.; Klug, D. D. *J. Appl. Phys.* **2007**, *102*.

(46) Graetz, J.; Chaudhuri, S.; Lee, Y.; Vogt, T.; Muckerman, J. T.; Reilly, J. J. *Phys. Rev. B* **2006**, *74*.

(47) Palasyuk, T.; Tkacz, M. *Solid State Commun.* **2004**, *130*, 219.

(48) Kim, E.; Kumar, R.; Weck, P. F.; Cornelius, A. L.; Nicol, M.; Vogel, S. C.; Zhang, J. Z.; Hartl, M.; Stowe, A. C.; Daemen, L.; Zhao, Y. S. *J. Phys. Chem. B* **2007**, *111*, 13873.

(49) Makarova, O. L.; Goncharenko, I. N.; Le Bihan, T. *Solid State Commun.* **2004**, *132*, 329.

(50) Trudel, S.; Gilson, D. F. R. *Inorg. Chem.* **2003**, *42*, 2814.

(51) Li, B.; Li, Y. W.; Yang, K. F.; Cui, Q. L.; Ma, Y. M.; Zou, G. T. *J. Phys-Condens. Mat.* **2007**, *19*.

(52) Custelcean, R.; Dreger, Z. A. *J. Phys. Chem. B* **2003**, *107*, 9231.

(53) Kume, T.; Ohura, H.; Sasaki, S.; Shimizu, H.; Ohmura, A.; Machida, A.; Watanuki, T.; Aoki, K.; Takemura, K. *Phys. Rev. B* **2007**, *76*.

(54) Talyzin, A. V.; Sundqvist, B. *High Pressure Res.* **2006**, *26*, 165.

(55) Vajeeston, P.; Ravindran, P.; Kjekshus, A.; Fjellvag, H. *Appl. Phys. Lett.* **2004**, *84*, 34.

(56) Majzoub, E. H.; Ronnebro, E. *J. Phys. Chem. C* **2009**, *113*, 3352.

(57) Trudel, S.; Gilson, D. F. R. *Inorg. Chem.* **2003**, *42*, 2814.

Chapter 2 *In situ* high-pressure study of ammonia borane by Raman and IR spectroscopy

A version of this chapter has been published in *Can. J. Chem.* **2009,** *87,* 1235.

2.1 Introduction

The ammonia borane complex ($NH_3 \cdot BH_3$) has received intensive investigation in recent years because of its promising potential as a hydrogen storage material.[1-2] Ammonia borane is a chemical hydride with high gravimetric (19.6 wt. % H) and volumetric (145 gH L^{-1}) hydrogen density and low molecular weight (30.7 g mol^{-1}). At room temperature and ambient pressure, $NH_3 \cdot BH_3$ is a stable solid, neither flammable nor explosive. Heating $NH_3 \cdot BH_3$ releases hydrogen at temperatures from 350 K to 410 K to yield polyaminoborane $(BH_2NH_2)_x$.[3-5] The reaction is moderately exothermic (ΔH = −21 kJ mol^{-1}).[6] Continued heating releases a second equivalent hydrogen at temperatures from 380 K to 470 K, yielding polyiminoborene $(BHNH)_x$ and trace quantities of borazine $(B_3N_3H_6)$.[6-9]

In addition to the hydrogen storage development, the molecular and electronic structures of ammonia borane are of fundamental interest. Although the ammonia borane complex is isoelectronic with gaseous ethane at ambient conditions, it contains a highly polarized dative N→B bond (μ = 5.1 D) formed by the electron donor-acceptor pair. The N→B bond has a dissociation energy of ~130 kJ mol^{-1},[10] which is much stronger than a typical van der Waals interaction. In addition, this dative bond is much shorter (1.58 Å)[11] in the molecular solid than in the gas phase (1.67 Å).[12] As a result, ammonia borane forms a stable molecular solid under ambient conditions that is characterized by strong dipole-dipole interactions in the crystalline network. More significantly, this complex is known to contain "dihydrogen" bonding. A dihydrogen bond is an unconventional

hydrogen bond with, for example, N-H···H-B intermolecular interactions in $NH_3{\cdot}BH_3$ crystals, with 2.02 Å being the shortest H-H distance.[11] Typically, dihydrogen bonding is characterized by a short H-H contact distance (<2.2 Å) and a strongly bent angle (i.e., the angle between N-H and H-B). The effects of dihydrogen bonding on the vibrational dynamics of the molecular crystal were recently demonstrated using incoherent inelastic neutron scattering.[13] These structural characteristics, including bond strength, bond length and the directionality of dihydrogen bonding, critically determine the molecular and crystal symmetries and, therefore, the stabilities of $NH_3{\cdot}BH_3$.

$NH_3{\cdot}BH_3$ crystal structures have been examined using x-ray diffraction techniques.[14-16] At room temperature, $NH_3{\cdot}BH_3$ adopts a tetragonal structure with the space group *I*4*mm* (C_{4v}^9) and cell parameters a = b = 5.240 Å and c = 5.028 Å.[15-18] Each unit cell contains two molecules occupying 2*a* Wyckoff sites with a C_{3v} molecular axis that coincides with the C_{4v} site symmetry (Fig. 2.1*a*).[16-18] This molecular crystal undergoes a phase transition from an orientationally disordered tetragonal phase to an orthorhombic structure (Fig. 2.1*b*) when cooled to 225 K, resulting in a significant

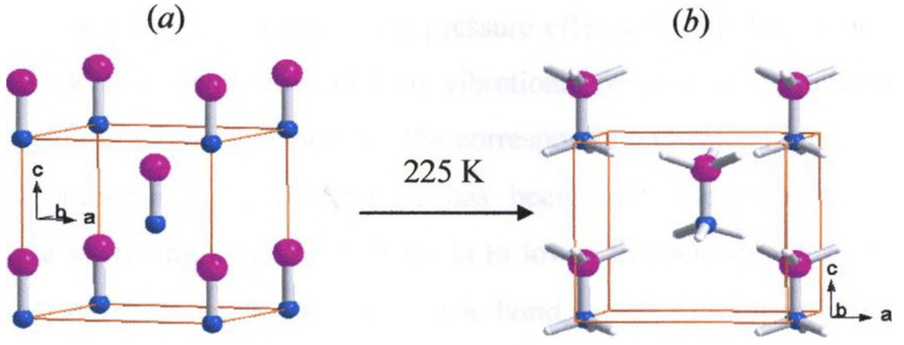

Fig. 2.1. Ambient-pressure crystal structures and temperature induced transitions of $NH_3{\cdot}BH_3$. The coordinate systems to show the orientations of the unit cell are indicated. The color codes for atoms are: boron (pink); nitrogen (blue) and hydrogen (white). (*a*) shows the tetragonal structure of $NH_3{\cdot}BH_3$ with space group *I*4*mm* (Z = 1) at room temperature. Due to the orientational disorder associated with the free rotation of the NH_3 and BH_3 groups, the hydrogen atoms are not shown. (*b*) The ordered orthorhombic structure of $NH_3{\cdot}BH_3$ formed at 225 K with space group $Pmn2_1$ (Z = 2) is shown.

change in the lattice dynamics. However, the molecular structure of the $NH_3{\cdot}BH_3$ molecule is preserved.[19] This orthorhombic structure was shown to have the space group $Pmn2_1$ with two molecules per unit cell and the parameters a = 5.517 Å, b = 4.742 Å and c = 5.020 Å. At this temperature the NH_3 and BH_3 groups are 'frozen' such that an ordered structure with a staggered conformation is formed with coinciding N-B and c-axes. The crystal structure reveals that the complex has C_s symmetry only, although a recent low-temperature ^2H NMR study suggests that the symmetry of the molecule is very close to C_{3v} and therefore it largely retains its symmetric gas-phase structure.[20]

Furthermore, $NH_3{\cdot}BH_3$ has been studied extensively using vibrational spectroscopy under varying conditions. Early IR and Raman studies on ammonia borane and its isotopologues focused on the nature and behaviour of the B-N bond.[21-23] Subsequent studies investigated the vibrational frequencies of ammonia borane (and its isotopologues) using an argon matrix[21] and by performing computational work on free molecules.[24-25] More recently, Hess *et al.*[19] have used Raman spectroscopy to study single -crystal ammonia borane complexes at temperatures as low as 88 K. In addition, ammonia borane has been studied under pressures as high as 4 GPa using Raman spectroscopy,[22,26] in order to investigate the pressure effects of dihydrogen bonds on the crystalline network. It is well known that the vibrational frequencies of molecular solids under pressure exhibit a blue shift because the corresponding chemical bonds stiffen as a result of the compression. In contrast, it has been well documented that, during compression, the stretching mode of A-H shifts to lower frequencies when A-H acts as the proton donor and forms an A-H···A hydrogen bond, which subsequently weakens the A-H bond. By analogy, an N-H···H-B dihydrogen bond is expected to form in the ammonia borane complex because of the short distance between the two hydrogens, where N-H acts as the proton donor and H-B acts as the proton acceptor. This dihydrogen bond model is confirmed by the observation of a red shift in the N-H stretch frequency and a blue shift in the B-H stretch frequency with increasing pressures.[22,26] In addition, pressure-induced phase transitions were reported in both studies, but with different transition pressures and detailed spectroscopic features.[22,26]

Although ammonia borane has been studied extensively, more questions remain about the structures and properties of ammonia borane at higher pressure regions. For example, will ammonia borane form any other structures in addition to the observed tetragonal and orthorhombic phases? Will the continuous weakening of the N-H bond when compressed result in dissociation or other chemical transformations in which hydrogen is discharged? Addressing these questions, especially the possibility of hydrogen discharge and reverse processes with pressure variations, is of fundamental interest for developing this potential hydrogen storage material. Therefore, it is critical to investigate the stability, inter- and intra-molecular interactions, transformations and reversibility of ammonia borane subjected to greater compression. Here we report the *in situ* high-pressure study of $NH_3 \cdot BH_3$ by Raman and IR spectroscopy using synchrotron light sources up to 14 GPa using the diamond anvil cell (DAC) technique.[27] We note that this complex was recently studied under pressures as high as 20 GPa using Raman spectroscopy by Lin *et al.*[28] In this study, two new possible phase transitions were identified at 5 and 12 GPa. Although we observed some similar ammonia borane transitions, we also observed new pressure-induced structural transformations. To our knowledge, this is the first time that IR measurements, which provide sensitive and quantitative structural information, have been performed on this complex at high pressures *in situ*. In addition, we obtained the first high-quality spectroscopic data in the lattice region, especially in the far-IR spectral measurements. The combined spectroscopic techniques used allowed us to perform an in-depth analysis on the high-pressure structures and stabilities of the complex. Compared with previous Raman studies, this study provides the most comprehensive understanding of the pressure behaviors and structures of $NH_3 \cdot BH_3$.

2.2 Experimental

2.2.1 Sample preparation

Ammonia borane as a fine crystalline white powder with ~97% purity was purchased from Sigma-Aldrich and used without further purification. The purity was checked by ambient-pressure Raman spectroscopy and all observed Raman modes were found to be associated with the complex without any unassignable modes that originated from impurities. A symmetrical DAC with two type-I diamonds each with a 400 μm culet was used for the high-pressure Raman measurements, while a pair of type II diamonds with a culet size of 300 μm was used for the IR measurements. A stainless steel gasket sample chamber was pre-indented to 70 μm thicknesses, and a 150 μm wide hole was drilled in the center. $NH_3 \cdot BH_3$ was loaded in a MBraun LABmaster 130 glove box equipped with a 20× microscope on the front panel. A dry inert atmosphere of <20 ppm O_2 and H_2O was maintained to accommodate the hygroscopicity of the material. The samples were loaded at room temperature with slightly elevated ambient pressures and then carefully pressurized incrementally. After each pressure change the samples were allowed to equilibrate for a few minutes before subsequent spectroscopic measurements were taken. A few ruby (Cr^{3+} doped α-Al_2O_3) chips were used as a pressure calibrant and carefully placed inside the gasket chamber before the sample was loaded. The pressure was determined by using the R_1 ruby fluorescence line pressure shift with an accuracy of ±0.05 GPa under quasi-hydrostatic conditions.[29] For the entire pressure region, ruby fluorescence spectra obtained on different ruby chips across the sample chamber indicated no significant pressure gradient. The ruby spectral profiles suggested no obvious non-hydrostatic effects, particularly at the lower pressure regions (e.g., <10 GPa). Therefore, no pressure transmission media were used.

2.2.2 High-pressure Raman measurements

Raman experiments were carried out with a customized Raman micro-spectroscopy system constructed in our lab. A 488 nm line from an Innova Ar^+ laser (Coherent Inc.) was used as the excitation source. The laser was focused to <5 μm on the

sample by an Olympus 20× objective, and a 15× eyepiece and a digital camera allowed precise alignment of the focused laser beam. The Raman scattering signal was collected by the same objective lens with backscattering geometry. The Rayleigh scattering was removed by a pair of notch filters that enabled a spectral >100 cm^{-1} to be measured before the total scattered photons were focused on the entrance slit of a spectrometer. The scattered light was then dispersed using an imaging spectrograph that housed a 0.5 m focal distance monochromator equipped with multiple gratings. An 1800 lines/mm grating with 0.1 cm^{-1} resolution was used. The Raman signal was recorded using an ultrasensitive liquid nitrogen cooled, back-illuminated, charge-coupled device (CCD) detector from Acton. The system was calibrated using neon lines with an uncertainty of 1 cm^{-1}. As a result of the strong diamond T_{2g} Raman mode at 1334 cm^{-1}, the spectra were collected in ranges of 50 to 1300 cm^{-1} and 1400 to 3500 cm^{-1} in several dispersive collection windows. These frequency ranges allowed all active ammonia borane Raman modes to be observed. The Raman signal was collected for 20 s for each window, and the average laser power on the sample was maintained at ~30 mW. Pressure effects on ammonia borane were examined both in the compression and decompression directions. All experiments were conducted at room temperature at pressures of up to 13.5 GPa and reproduced several times.

2.2.3 High-pressure IR measurements

Infrared experiments were performed at the U2A beamline at the National Synchrotron Light Source (NSLS) at Brookhaven National Laboratory (BNL). The IR beam from the storage ring was extracted through a wedged diamond window from a source in a 40 × 40 mrad solid angle and was collimated to a 3.8 cm diameter beam before entering a Bruker IFS 66V vacuum FT-IR spectrometer in conjunction with three microscope systems. The spectrometer was equipped with a number of beam splitters and detectors including a silicon bolometer and MCT. For mid-IR measurements, the IR beam was focused on to the sample by a Bruker IR microscope and then the spectrum

was collected in transmission mode by the MCT detector in the 600 – 4000 cm^{-1} spectral range. The far-IR spectra of $NH_3 \cdot BH_3$ were collected using a customized IR microscope with high collection efficiency and recorded by the bolometer in the 100 – 600 cm^{-1} spectral region. A resolution of 4 cm^{-1} was used in all IR measurements. For IR measurements, a sample thickness of 35 μm was used to allow sufficient IR transmission measurements. For all measurements, mid-IR spectra were collected through a 30 × 30 μm^2 aperture, whereas the effective IR transmission area covered the entire sample (i.e., a circle of ~90 μm in diameter) for the far-IR measurements. The reference spectrum, i.e., the diamond anvil absorption at ambient pressure, was later subtracted as background from each sample spectrum to obtain the absorbance. IR spectra in the decompression sequence (in ~2 GPa decrements) were also collected to investigate the reversibility of the pressure effect.

2.3 Results and discussion

2.3.1 Raman spectra of $NH_3 \cdot BH_3$ during compression

Raman spectra of ammonia borane were collected from ambient pressures up to 13.5 GPa. Selected spectra are shown in Fig. 2.2 in four regions based on the molecular nature of the complex: the lattice region (50 – 600 cm^{-1}), the B–N stretching, the BH_3/NH_3 deformations and NBH rocking region (600 – 1650 cm^{-1}), the B–H stretching region (2100 – 2700 cm^{-1}) and the N–H stretching region (2750 – 3400 cm^{-1}).

At ambient pressure and room temperature $NH_3 \cdot BH_3$ crystallizes into a tetragonal phase with space group *I4mm* with two $NH_3 \cdot BH_3$ molecules per unit cell.[16-18] Using factor group analysis,[19] 12 distinct modes, including 11 internal modes plus one lattice librational mode, are predicted to be both Raman and IR active for the tetragonal phase of $NH_3 \cdot BH_3$. Initially, a Raman spectrum measured at room temperature and

Table 2.1. Raman modes of ammonia borane observed under different conditions

This work[a]	Ether solution[b]	Crystal[c]	Crystal[d]	Powder[e]	Assignment	Mode
3319	3309	3316	3316	3312	ν_7 (E)	Asym. N-H stretch
3253	3183	3250	3255	3245	ν_1 (A_1)	Sym. N-H stretch
2376	2316	2328	n.o.	2316	ν_8 (E)	Asym. B-H stretch
2280	2285	2279	2280	2277	ν_2 (A_1)	Sym. B-H stretch
1595	1600	1600	1596	1597	ν_9 (E)	NH_3 deformation
1377	n.o.	1357	1375	1374	ν_3 (A_1)	NH_3 deformation
1188	1175	1189	1185	1165	ν_{10} (E)	BH_3 deformation
1161	n.o.	1155	1158	n.o.	ν_4 (A_1)	BH_3 deformation
1067	1060	1065	1066	1058	ν_{11} (E)	NBH rock
798	n.o.	800	798	790	ν_5' (A_1)	^{10}B-N stretch
783	787	784	782	776	ν_5 (A_1)	^{11}B-N stretch
728	n.r.	727	726	715	ν_{12} (E)	NBH rock
141	n.r.	n.r.	175[f]	n.r.	Lattice mode	

Note: n.o., not observed; n.r., not reported.

[a] Measured at room temperature and ambient pressure.

[b] Reference 21.

[c] Reference 19.

[d] Reference 22.

[e] Reference 23, at low temperature.

[f] Raman shift at 1.9 GPa (see text).

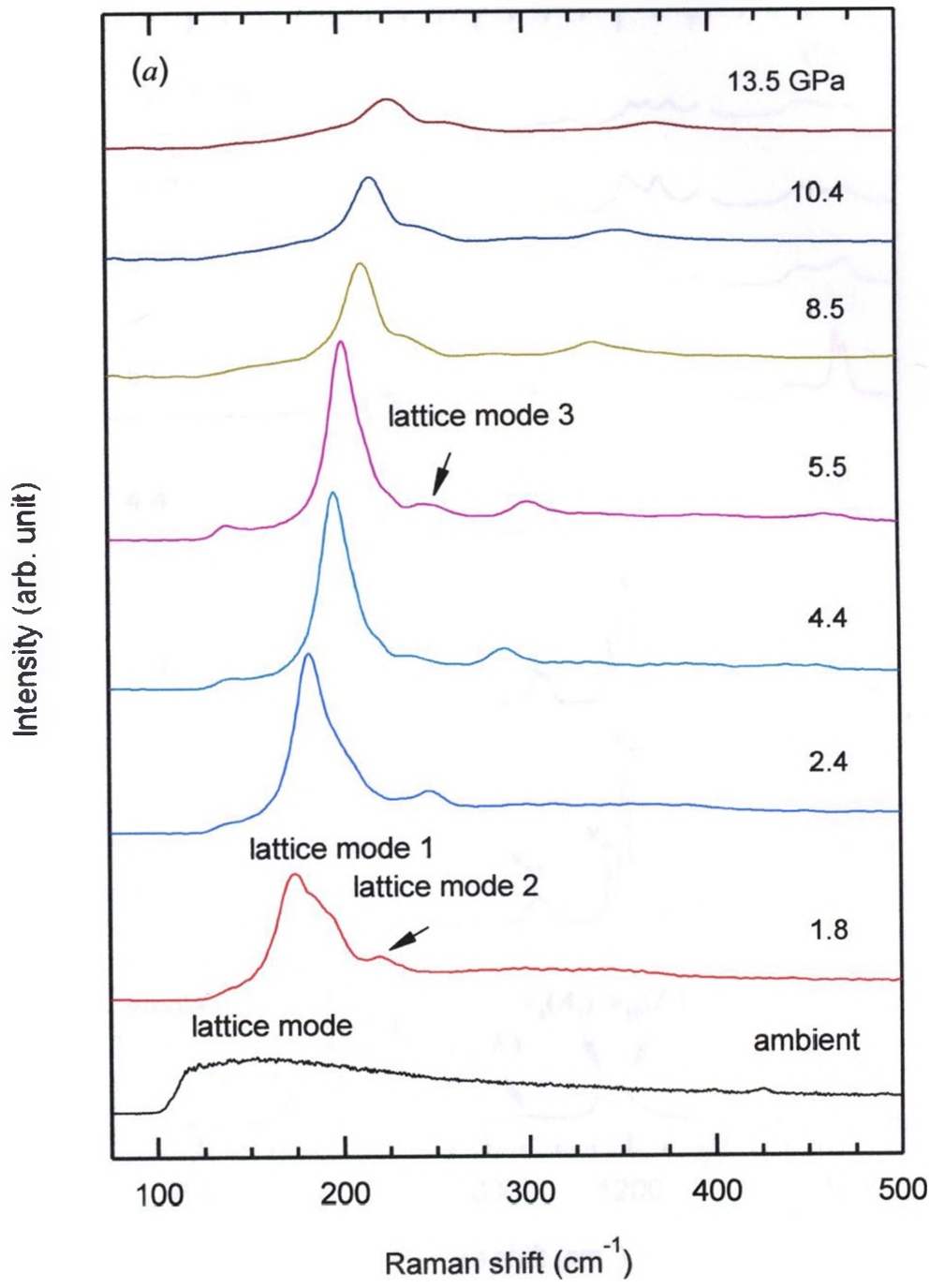
(a)
13.5 GPa
10.4
8.5
lattice mode 3
5.5
4.4
2.4
lattice mode 1
lattice mode 2
1.8
lattice mode
ambient
Intensity (arb. unit)
100
200
300
400
500
Raman shift (cm-1)

Fig. 2.2

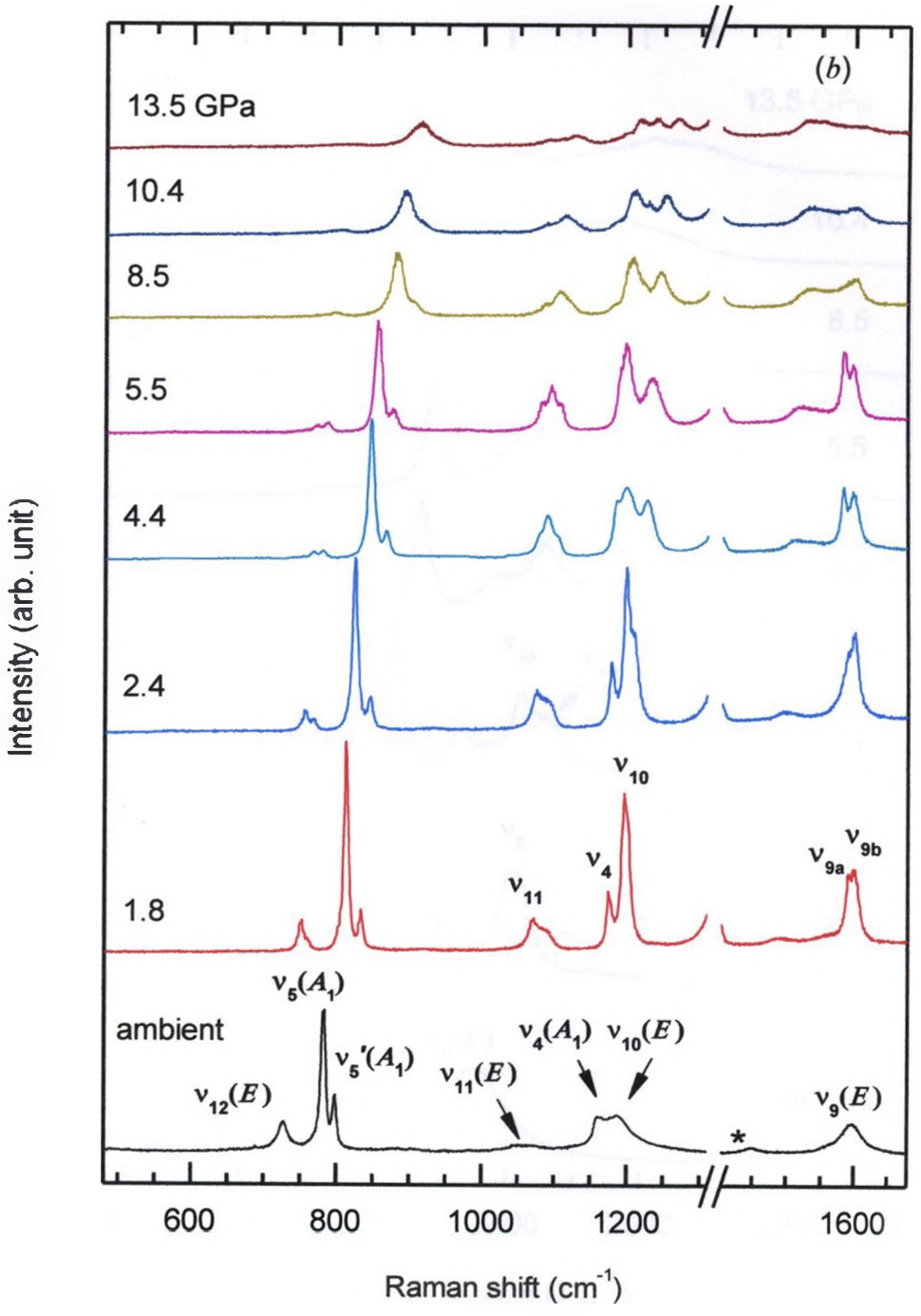

Fig. 2.2, continued

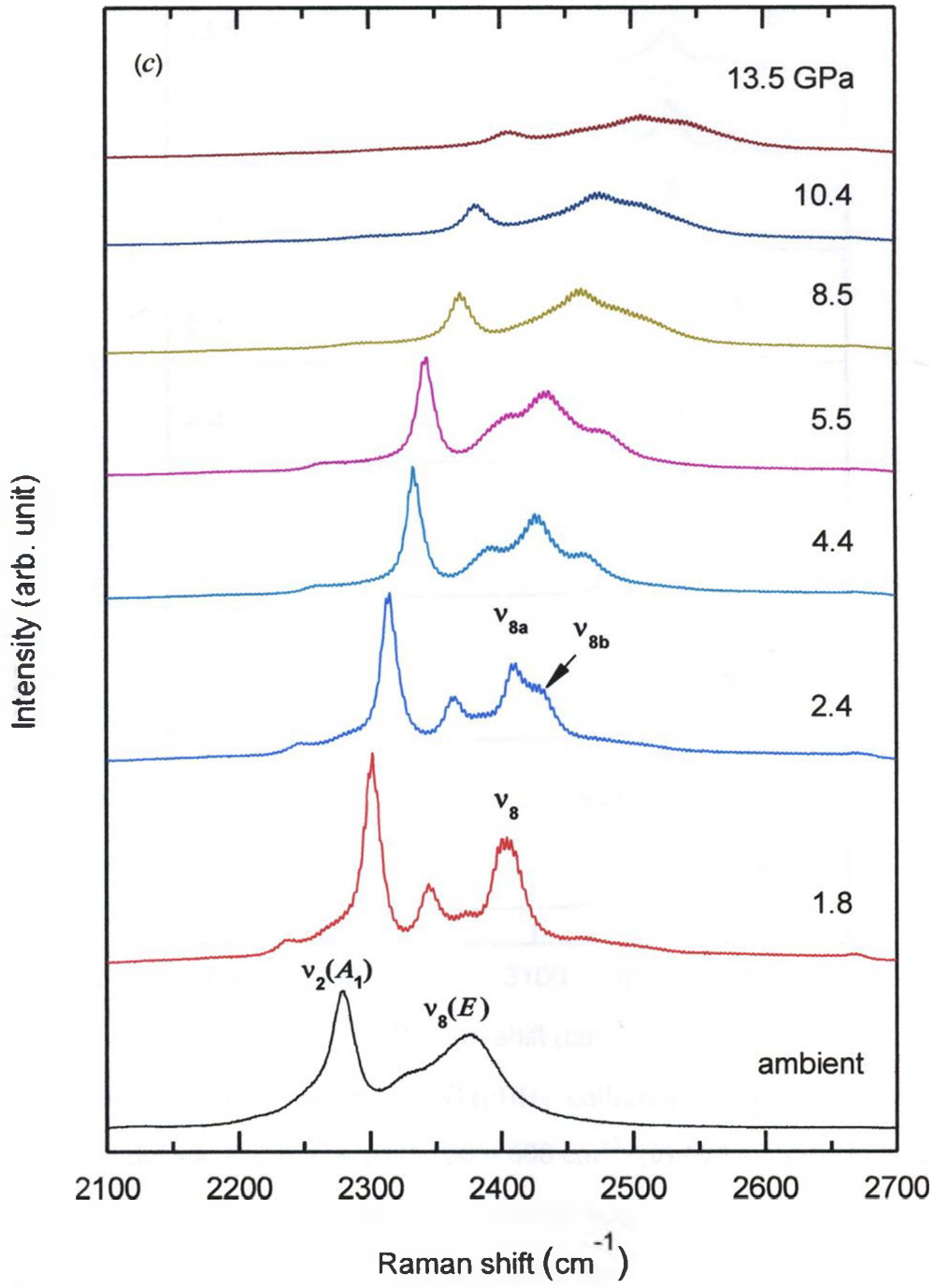

Fig. 2.2, continued

Continued

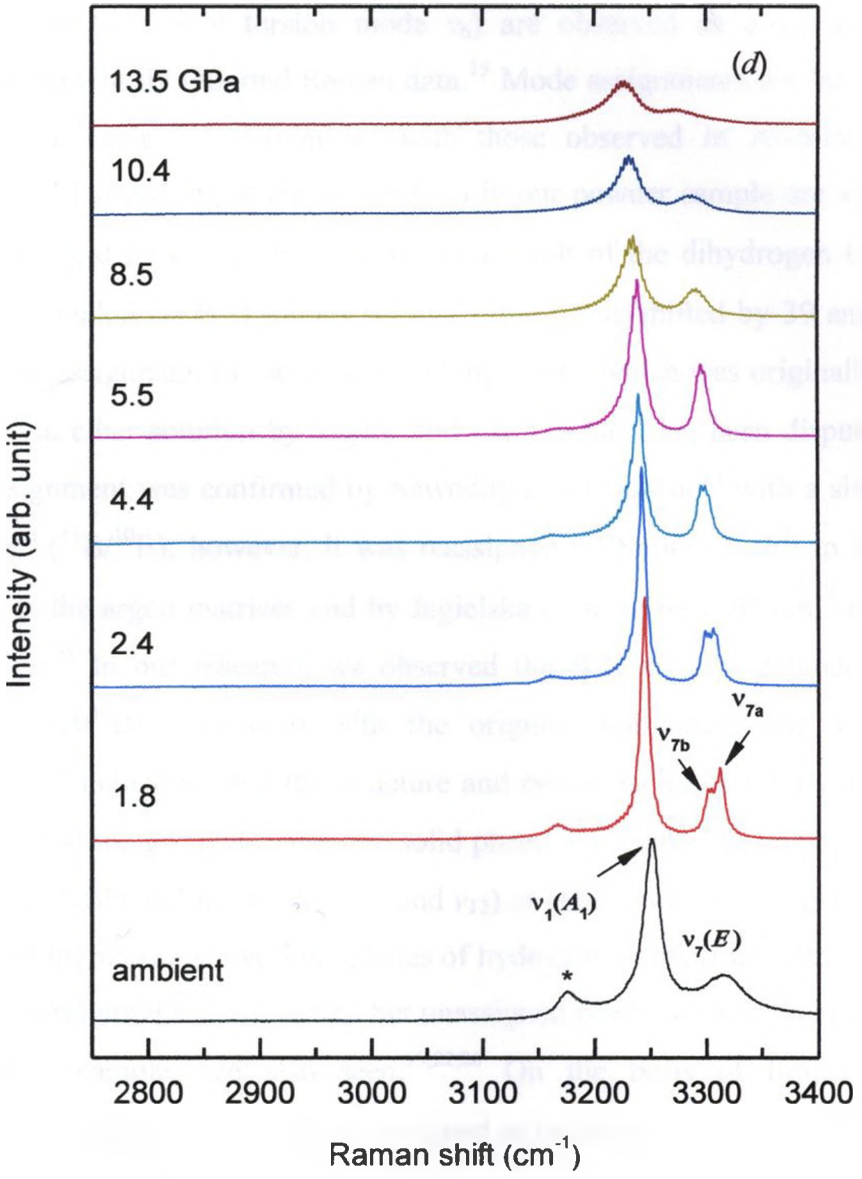

Fig. 2.2. Selected Raman spectra of $NH_3 \cdot BH_3$ collected at room temperature on compression in the spectral region of (*a*) 50 – 600 cm^{-1}, (*b*) 600 – 1650 cm^{-1}, (*c*) 2100 – 2700 cm^{-1} and (*d*) 2750 – 3400 cm^{-1}. The relative intensities are normalized and thus are directly comparable. Because of the intense T_{2g} Raman mode of the diamond anvil at 1332 cm^{-1}, the region of 1270 – 1440 cm^{-1} is truncated in (b).The pressures in GPa are labeled for each spectrum. The assignments of Raman modes are labeled for several spectra. Unassigned peaks are labeled with asterisks (see text). The spectra are offset vertically for clarity.

ambient pressure is depicted at the bottom of Fig. 2.2*a-d*. As shown, all Raman active modes except one (i.e., B-N torsion mode ν_6) are observed as predicted, in good agreement with previously reported Raman data.[19] Mode assignments are labeled in Fig. 2.2 and listed in Table 2.1. Compared with those observed in Ar-matrix isolated molecules, the N-H stretching modes (ν_7 and ν_1) in our powder sample are significantly red-shifted by 67 and 84 cm^{-1}, respectively, as a result of the dihydrogen bond in the solid phase. The analogous B-H modes (ν_8 and ν_2) are blue-shifted by 39 and 60 cm^{-1}, respectively. The assignment of the B-N stretching mode, which was originally assigned to be 787 cm^{-1} in ether solution by Taylor and Cluff,[21] has long been disputed. Taylor and Cluff's assignment was confirmed by Sawodny and Goubeau[23] with a similar value of 776/790 cm^{-1} ($^{11}B/^{10}B$); however, it was reassigned by Smith *et al.*[30] to be 968/987 cm^{-1} ($^{11}B/^{10}B$) in the argon matrices and by Jagielska *et al.* to be 1005 cm^{-1} using an *ab initio* calculation.[31] In our research, we observed the B-N stretching mode (ν_5/ν_5') at 783/798 cm^{-1} ($^{11}B/^{10}B$), consistent with the original assignment and some recent observations,[22,26,28] indicating that the structure and behaviour of $NH_3 \cdot BH_3$ in the argon matrices is closer to the gas phase than the solid phase. For peaks at 1067 and 728 cm^{-1}, the assignment as NBH rocking modes (ν_{11} and ν_{12}) of Hess *et al.* was adopted. which are described as rocking motions involving planes of hydrogen atoms from both the NH_3 and BH_3 groups. Several previously observed but unassigned peaks, such as those at 3175 and 1447 cm^{-1}, for example, are also seen.[19,22,26] On the basis of limited polarized measurements,[19] the peak at 3175 cm^{-1} is assigned as polarized whereas the peak at 1447 cm^{-1} is a depolarized mode.

Upon compression from ambient pressure to 1.8 GPa, a phase transition can be identified by the splitting of the modes with *E* symmetry, as well as the by the significant narrowing of the lattice mode (Fig. 2.2). For instance, the doubly degenerate modes ν_7 (asymmetrical N-H stretching) at 3319 cm^{-1} and ν_9 (NH_3 deformation) at 1595 cm^{-1} each split into two modes, i.e., ν_{7a}/ν_{7b} (3303 cm^{-1}/3312 cm^{-1}) and ν_{9a}/ν_{9b} (1593 cm^{-1}/1602 cm^{-1}). The phase transition is also apparent by the development of the lattice mode near

141 cm^{-1} at ambient pressure, which becomes more pronounced and finally evolves into two lattice modes at 174 cm^{-1} and 220 cm^{-1} at 1.8 GPa. The sharp lattice modes strongly suggest a phase transition from the disordered tetragonal structure at ambient pressure to an ordered structure at 1.8 GPa. It is also noted that modes v_4 and v_{10}, which are very close to each other at ambient pressure, become sharply resolved at 1.8 GPa, whereas the very weak NBH rocking mode v_{11} (1067 cm^{-1}) is greatly enhanced. In addition, a new peak appears at 2344 cm^{-1}, which was also observed but unassigned in some earlier studies.[19,22,26,28] This unassigned mode is likely a depolarized band.[19]

Upon further compression to 13.5 GPa, rich Raman features were observed to reveal the pressure-induced structural revolutions. As seen in Fig. 2.2*a*, the most prominent peak in the lattice in the whole pressure region is lattice mode 1, which appears at 174 cm^{-1} at 1.8 GPa. This mode becomes sharper and more intense as pressures increase to 5.5 GPa, at which point it noticeably broadens with decreasing intensity when compressed to 13.5 GPa. Lattice mode 2, though very weak at 1.8 GPa, is a characteristic mode of the new phase that is different than the disordered tetragonal structure and remains distinct as pressures increase to 13.5 GPa. The most prominent change in the lattice region is the observation of a third lattice mode at 245 cm^{-1} at 5.5 GPa, indicating a possible transformation of the crystal structure of $NH_3 \cdot BH_3$. In addition, a clearly developed mode at 140 cm^{-1} was also observed at this pressure. These new modes, together with lattice mode 2, become weaker with increasing pressure such that only lattice mode 1 remains the dominant mode at 13.5 GPa. We note that in previous Raman studies only two lattice modes are observed in all pressure regions,[28] which is in strong contrast to our results. It is likely that the missing mode at 140 cm^{-1} is associated with the detection limit achieved.

The internal modes in the spectral region 600 to 1650 cm^{-1} (Fig. 2.2*b*), including the v_{12}, v_{11}, v_{10}, and v_9 modes when compressed to 2.4 GPa, are characterized by further splitting of the doubly degenerate modes with *E* symmetry during compression. Upon further compression to 5.5 GPa, these modes exhibit the maximum splitting with

the exception of ν_7, which merged into a singlet. Continuous compression from 5.5 to 8.5 GPa results in merging with a markedly reduced intensity for most of the modes. All modes are significantly broadened when compressed above 13.5 GPa. These observations are in general agreement with those of Lin *et al.*,[28] except for the detailed profile of a few bands. For instance, the NH_3 deformation mode (ν_9) at approximately 1600 cm^{-1} that exhibits clear splitting up to 5.5 GPa shows a drastically different profile: no splitting was observed in the entire pressure region.[28]

The splitting at ν_5 mode is due to an isotopic effect rather than the removal of degeneracy. The ^{11}B and ^{10}B contributions to the B-N symmetric stretch (ν_5 and ν_5') are readily apparent up to 8.5 GPa. Both ^{11}B-N (ν_5) and ^{10}B-N (ν_5') stretching modes are sharp in the pressure region under 5.5 GPa, while ν_5' is much weaker than ν_5 because of the lower abundance of ^{10}B (19.9%). The frequency difference at 8.5 GPa is approximately 19 to 21 cm^{-1}, which is larger than that observed under ambient conditions (i.e., 15 cm^{-1}). However, this value is still in agreement with the frequency difference of 18 cm^{-1} reported by Custelcean[22] and of 20 cm^{-1} observed by Lin.[28]

The symmetric B-H stretching mode ν_2 (A_1), one of the most intense Raman bands at ambient pressure, exhibits a pressure-induced blue shift and weakening (Fig. 2.2*c*); it becomes significantly broadened above 8.5 GPa. The doubly degenerate asymmetric B-H stretching mode ν_8 readily splits when compressed to 2.4 GPa, exhibiting a strongly asymmetric doublet labeled as ν_{8a} and ν_{8b}. As pressures continue to increase, mode ν_{8a} becomes most pronounced at 4.4 GPa and subsequently becomes much broader at higher pressures (e.g, 8.5 GPa) due to coalescence with ν_{8b} and a nearby depolarized peak.[19] In contrast to the B-H stretching modes, both the symmetric and asymmetric N-H stretching modes shift to red with increasing pressures (Fig. 2.2*d*). The symmetric N-H stretching mode ν_1 with A_1 symmetry, the most intense $NH_3{\cdot}BH_3$ Raman band in the entire pressure region, becomes much broader and weaker when compressed to 8.5 GPa. The asymmetric N-H stretching mode ν_7 (E) that displays a doublet (ν_{7a} and ν_{7b}) at 1.8 GPa becomes a convoluted mode on compression. Similar to the ν_1 mode, this

mode also broadens markedly beyond 8.5 GPa. Above 13.5 GPa, this mode is barely visible. These observations are consistent with those of Lin *et al.*[28]

2.3.2 Pressure effects on Raman modes of $NH_3 \cdot BH_3$

To confirm the possible phase transformations on compression, the pressure dependence (i.e., Raman shift vs. pressure) of selected Raman modes are depicted in Fig. 2.3. Calculated pressure coefficients [$d\nu / dP$ ($cm^{-1} \cdot GPa^{-1}$)] for the monitored peaks obtained by linear regression of the experimental data are listed in Table 2.2. Phase transitions are further indicated when sharp differences in pressure coefficients are observed. Compared with previous analysis,[28] more phase boundaries were identified in this study.

In general, most Raman modes exhibit pressure-induced blue shifts, consistent with the finding that the bonds stiffen upon compression. However, both the symmetric and asymmetric N-H stretching modes (ν_7 and ν_1) undergo red shifts with increasing pressures in all pressure regions (i.e., $d\nu / dP < 0$), indicating the weakening of the N-H bond. This is believed to be a result of the lengthening of the N-H bond due to the formation and strengthening of the dihydrogen bonding (N-H···H-B) as pressures increase. In strong contrast, the stretching modes (ν_8 and ν_2) involving the B-H proton acceptor group in the dihydrogen bond exhibit large blue shifts with pressure. For example, $d\nu_8 / dP$ has the largest pressure coefficients (16.1 and 10.3 cm^{-1} GPa^{-1} in the 2.4 to 5.5 GPa and >10.4 GPa pressure regions, respectively) indicating the significant strengthening of B-H bonding with decreasing bond length. Because the N-H and B-H bond strengths become strongly disproportionate when compressed, and the B-N bond is strengthened ($d\nu_5 / dP > 0$), it is reasonable to speculate that at certain high pressures, the N-H bond may break and new materials may form.

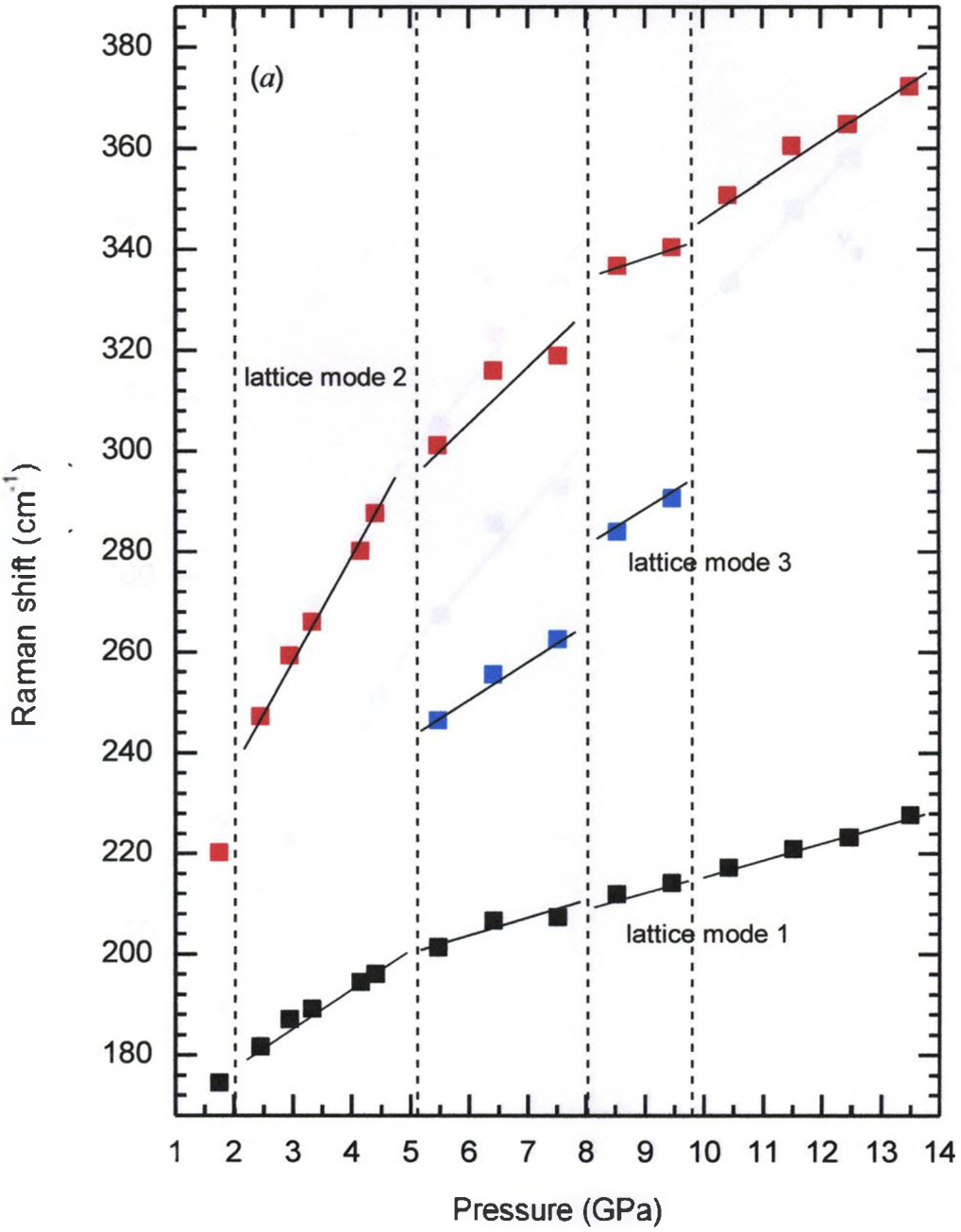
(a)
lattice mode 2
lattice mode 3
lattice mode 1
Raman shift (cm^{-1})
Pressure (GPa)
380
360
340
320
300
280
260
240
220
200
180
1
2
3
4
5
6
7
8
9
10
11
12
13
14

Fig. 2.3

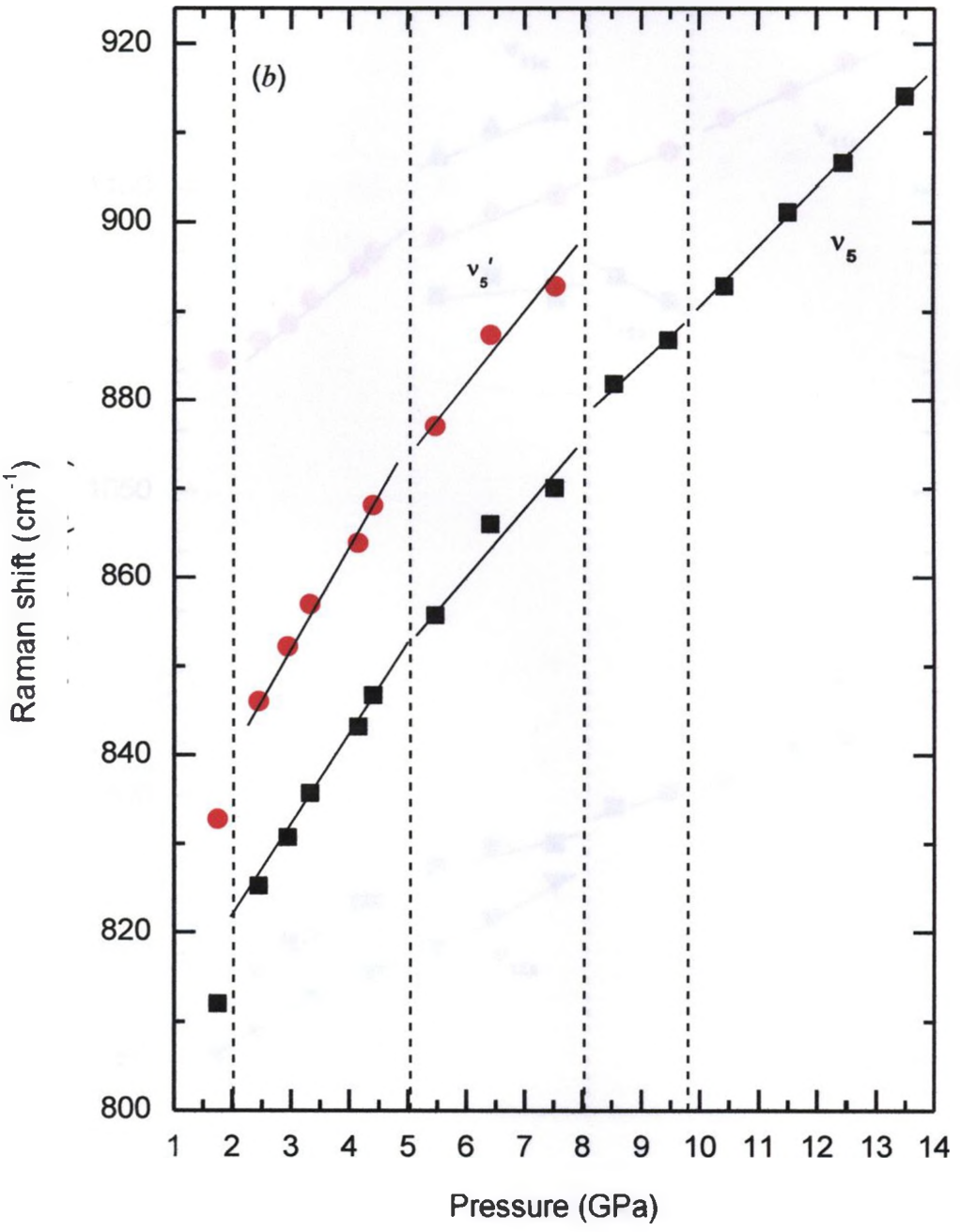

Fig. 2.3, continued

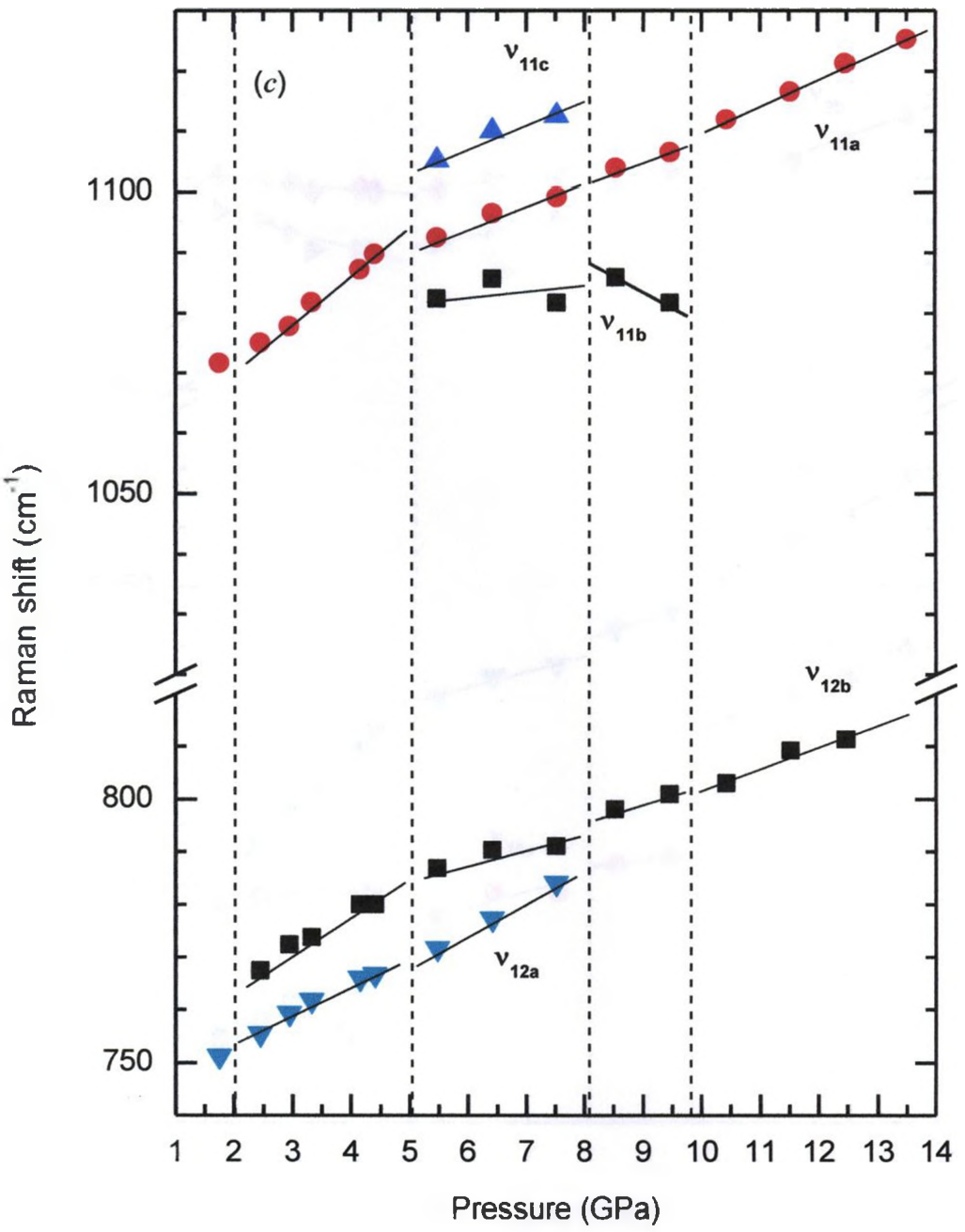

Fig. 2.3, continued

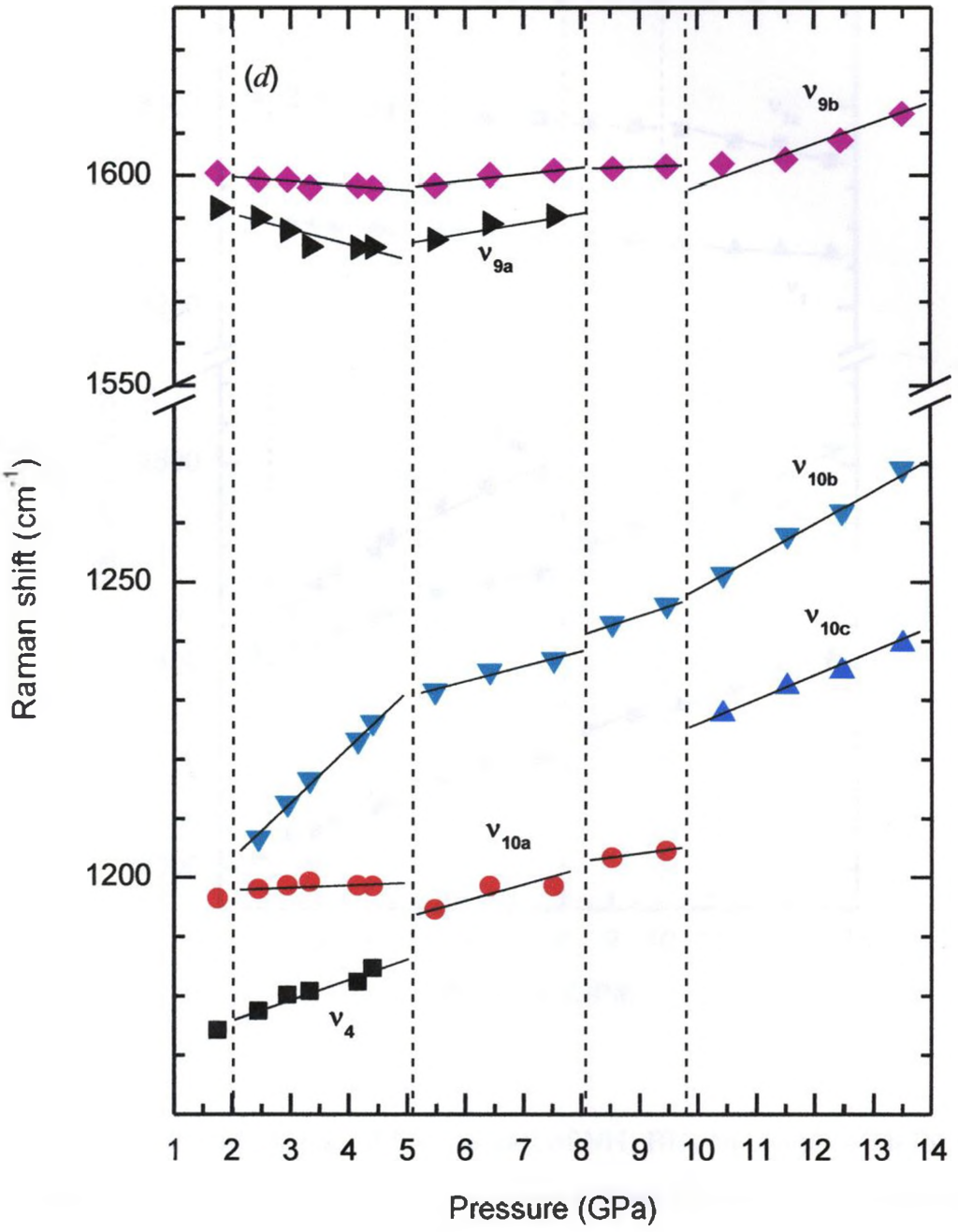

Fig. 2.3, continued

Continued

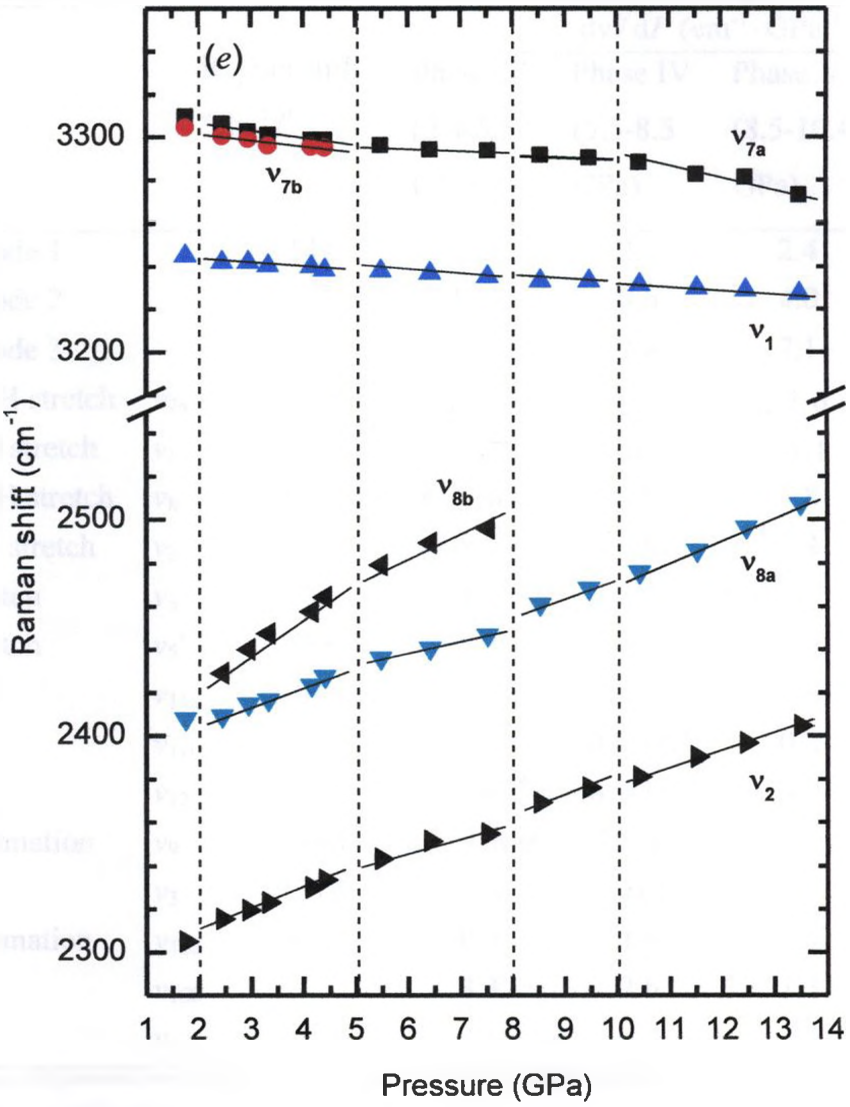

Fig. 2.3. Pressure dependences of Raman shift of $NH_3 \cdot BH_3$ on compression for (*a*) the lattice modes; (*b*) the BH_3 deformation (v_{10a}, v_{10b} and v_4) and NH_3 deformation (v_{9a} and v_{9b}) modes; (*c*) the ^{11}B-N/^{10}B-N stretch (v_5/v_5') modes; (*d*) the NBH rock (v_{12a}, v_{12b}, v_{11a}, v_{11b} and v_{11c}) modes; and (*e*) the N-H stretch (v_{7a}, v_{7b} and v_1) and B-H stretch (v_{8a}, v_{8b} and v_2) modes. Different symbols denote Raman modes with different origins. The solid lines crossing the solid symbols are based on linear fit. The vertical dashed lines indicate the proposed phase boundaries.

Table 2.2. Pressure dependence of the Raman modes of $NH_3 \cdot BH_3$ on compression

Mode		Raman shift (cm^{-1})[a]	dv/dP ($cm^{-1} \cdot GPa^{-1}$)			
			Phase III (2.4-5.5 GPa)	Phase IV (5.5-8.5 GPa)	Phase V (8.5-10.4 GPa)	Phase VI (>10.4 GPa)
Lattice mode 1		141	6.3	2.9	2.4	3.3
Lattice mode 2			17.8	8.6	4.0	6.7
Lattice mode 3				7.8	7.1	8.2
Asym. N-H stretch	v_{7a}	3319	–3.1/–2.7[b]	–1.2	–1.6	–4.6
Sym. N-H stretch	v_1	3253	-1.5	–0.9	–1.1	–1.3
Asym. B-H stretch	v_8	2376	8.7/16.1[c]	5.3/8.3[c]	7.8	10.3
Sym. B-H stretch	v_2	2280	9.2	5.6	7.4	7.6
^{11}B-N stretch	v_5	783	5.2	3.7	5.3	6.8
^{10}B-N stretch	v_5'	798	6.2	5.0		
NBH rock	v_{11a}	1067	6.1	3.3	2.8	4.4
	v_{11b}			0.6/3.6[d]	0.2	
	v_{12}	728	5.2/6.2[e]	6.1/2.0[e]	3.0	4.1
NH_3 deformation	v_9	1595	–2.3/–0.6[f]	2.7/1.7[f]	0.5	3.9
	v_3	1377	–0.3	–0.8		
BH_3 deformation	v_{10a}	1067	0.3	1.9	1.2	
	v_{10b}		8.3	2.6	1.3	5.6/3.7[k]
	v_4	1161	3.1			

[a] Measured at ambient pressure and room temperature.

[b] v_{7a}/v_{7b}.

[c] v_{8a}/v_{8b}.

[d] v_{11b}/v_{11c}.

[e] v_{12a}/v_{12b}.

[f] v_{9a}/v_{9b}.

[g] v_{10b}/v_{10c}.

As shown in Fig. 2.3 and Table 2.2, the pressure dependences of the major Raman modes collectively indicate several distinct pressure regions at which $NH_3 \cdot BH_3$ could exist as different phases. These pressure regions are 2.4 to 5.5 GPa, 5.5 to 8.5 GPa, 8.5 to 10.4 GPa and above 10.4 GPa, which we label as phases III, IV, V and VI, respectively (phases I and II are the known room-temperature tetragonal phase and low-temperature orthorhombic phase, respectively). In general, the pressure coefficients of the stretching modes are noticeably larger for phase III than for phase IV, which are larger than those for phase V. The pressure coefficients of the rocking and deformation modes, however, do not exhibit consistent trends along phase transformations. Interestingly, the pressure coefficients of these modes seem to become larger again when compressed beyond 10.4 GPa. In summary, although the phase boundaries of 2.4 and 5.5 GPa observed in this study can be roughly aligned with those at 2 and 5 GPa noted previously,[28] new phase boundaries along with more high-pressure phases are observed in the present study.

2.3.3 Raman spectra of $NH_3 \cdot BH_3$ during decompression

The reversibility of pressure effects on molecular structures provides important information on transformation mechanisms. Therefore, upon compression of $NH_3 \cdot BH_3$ to the highest pressure of 13.7 GPa, we conducted Raman measurements on decompression all the way down to a near ambient pressure. Selective spectra depicted in Fig. 2.4. In general, the change in the Raman profile is very gradual on decompression. At 13.7 GPa, one lattice mode and ν_5, ν_4, ν_{10}, ν_9, ν_8, ν_1 and ν_7 modes resolve. Starting at 6.2 GPa, the ν_2 mode at 2362 cm^{-1} recovers from decompression. Simultaneously, the ν_1 and ν_7 modes are completely deconvoluted. Further decompression to 4.0 GPa results in the development of ν_5', ν_{11} and $\nu_{9a,b}$ modes. The onset pressure for the observation of ν_{12} and ν_4 along decompression is 2.3 GPa. When the pressure is reduced to 0.8 GPa, the Raman

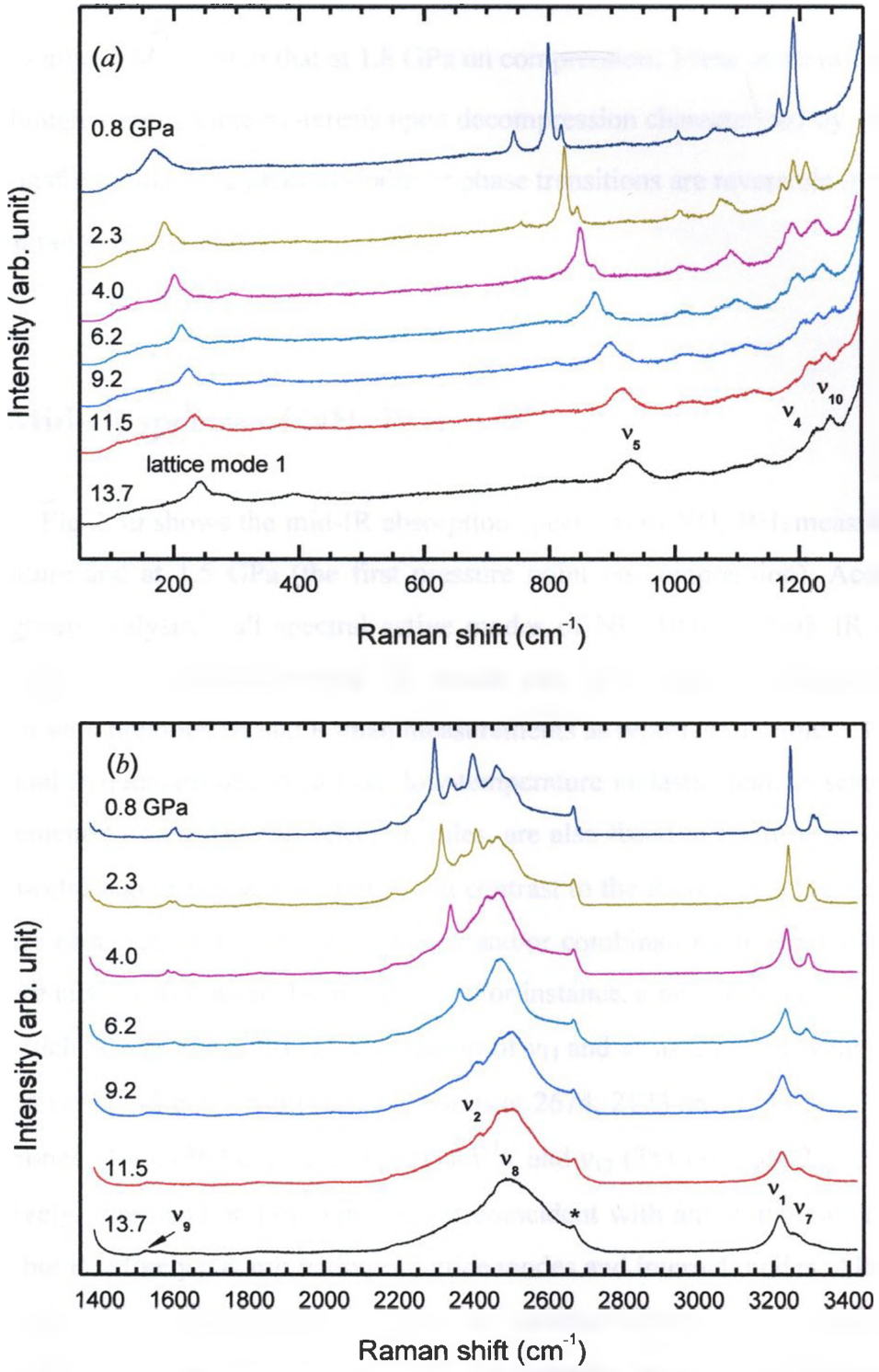

Fig. 2.4. Selected Raman spectra of $NH_3 \cdot BH_3$ on decompression from 13.7 GPa all the way down to ambient pressure. The relative intensities are normalized and thus are directly comparable. The pressures in GPa are labeled for each spectrum. The spectra are offset vertically for clarity.

profile is almost identical to that at 1.8 GPa on compression. These observations suggest that although there is some hysteresis upon decompression characterized by 'delayed' back-transformations, the pressure-induced phase transitions are reversible in the entire pressure range in this study.

2.3.4 Mid-IR spectra of $NH_3 \cdot BH_3$

Fig 2.5*a* shows the mid-IR absorption spectrum of $NH_3 \cdot BH_3$ measured at room temperature and at 1.5 GPa (the first pressure point on compression). According to a factor group analysis,[19] all spectral active modes of $NH_3 \cdot BH_3$ are both IR and Raman active. Therefore, the fundamental IR modes can be assigned by comparing our IR spectrum with previous IR and Raman measurements as reported in Table 2.3. In addition, vibrational frequencies observed from low-temperature inelastic neutron scattering (INS) measurements, which have no selection rules, are also listed to confirm the assignments in the spectra region below 1400 cm^{-1}.[25] In contrast to the Raman spectra, many more IR bands are observed as a result of overtones and/or combinations of fundamental modes, which are labeled with asterisks in Fig 2.5*a*. For instance, a new band is observed at 3479 cm^{-1}, which is very close to the combination of ν_{11} and ν_3 as $2\nu_{11}+\nu_3$, where ν_{11} = 1055 cm^{-1} and ν_3 = 1362 cm^{-1}. Similarly, the bands at 2674, 2123 and 1483 cm^{-1} are likely to be overtones of ν_3 (1362 cm^{-1}), ν_{11} (1055 cm^{-1}), and ν_{12} (751 cm^{-1}) as $2\nu_3$, $2\nu_{11}$ and $2\nu_{12}$, respectively. The band at 1767 cm^{-1} is not coincident with any combination of internal modes, but it is likely a combination of lattice modes and internal modes. Although some modes could not be distinguished due to the saturated absorptions in regions 1050 to 1250 cm^{-1} and 3150 to 3400 cm^{-1}, all fundamental internal modes except a BH_3 deformation mode and an N-H stretching mode are observed, which is in agreement with previous Raman and IR data.[21-23]

Fig. 2.6*a* shows the IR absorption spectra of $NH_3 \cdot BH_3$ when compressed to 13.7

Table 2.3. Assignment of IR fundamental frequencies for $NH_3 \cdot BH_3$ at in comparison with Raman data

IR (cm^{-1})		INS (cm^{-1})	Raman (cm^{-1})		Assignment	IR bands
This work[a]	Ref. 30[b]	Ref. 25[c]	This work[d]	Ref. 19[e]		
	3386		3303/ 3312[f]	3316	ν_7 (E)	Asym. N-H stretch
	3337		3244	3250	ν_1 (A_1)	Sym. N-H stretch
2453	2415		2404	2328	ν_8 (E)	Asym. B-H stretch
2337	2340		2302	2279	ν_2 (A_1)	Sym. B-H stretch
1584/ 1610[g]	1608		1593/ 1602[g]	1600	ν_9 (E)	NH_3 deformation
1362	1343	1368	1371	1357	ν_3 (A_1)	NH_3 deformation
1216	1186	1189	1198	1189	ν_{10} (E)	BH_3 deformation
	1175	1177	1174	1155	ν_4 (A_1)	BH_3 deformation
1055	1052	1080	1070	1065	ν_{11} (E)	NBH rock
828	987		832	800	ν_5 (A_1)	^{10}B-N stretch
810	968	798	812	784	ν_5' (A_1)	^{11}B-N stretch
751	603	737	751	727	ν_{12} (E)	NBH rock

[a] Measured at room temperature and 1.5 GPa.

[b] At low temperature.

[c] Using inelastic neutron scattering at 30 K.

[d] Measured at room temperature and 1.8 GPa.

[e] At room temperature.

[f] Frequencies for ν_{7a}/ν_{7b}.

[g] Frequencies for ν_{9a}/ν_{9b}.

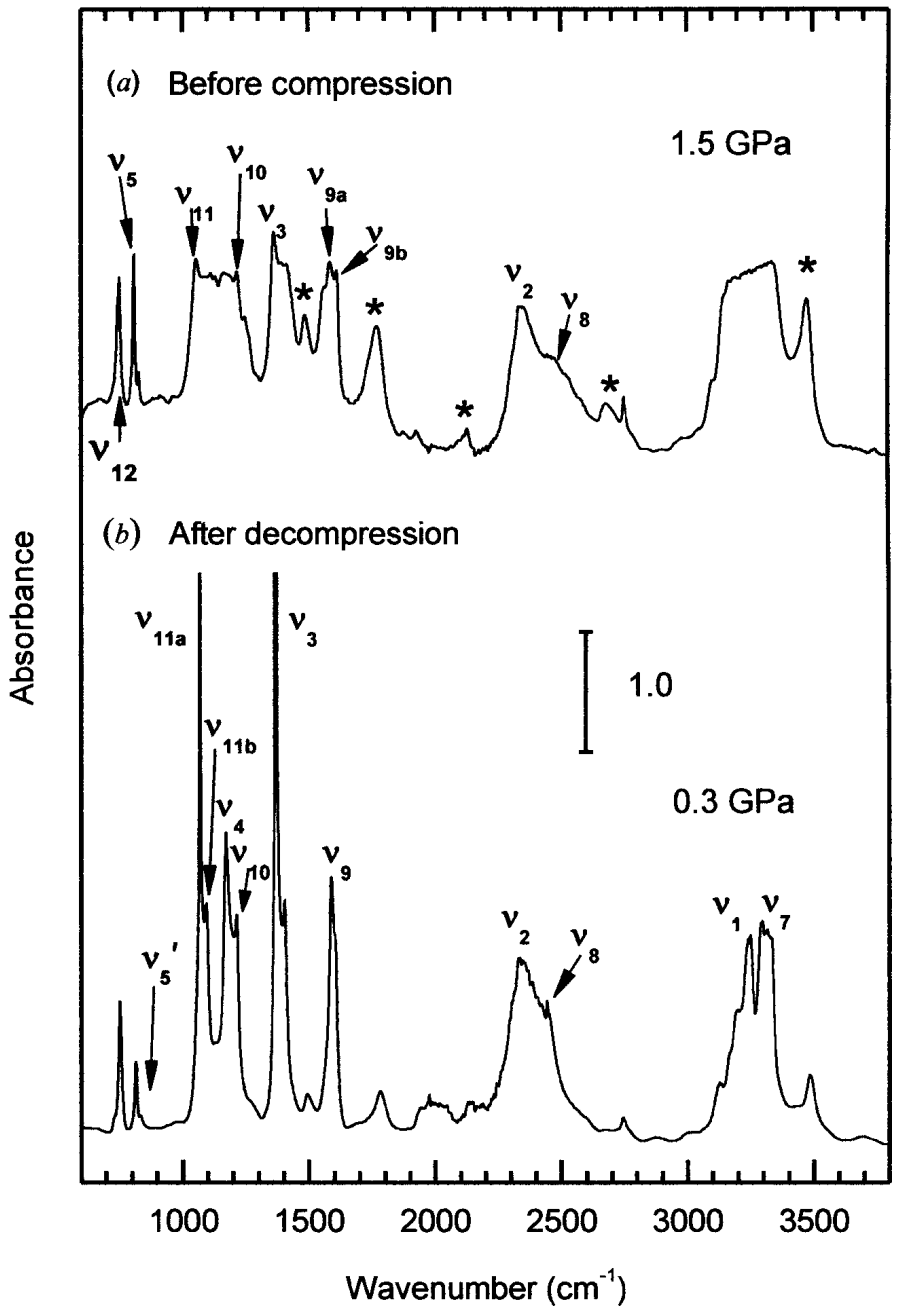

Fig. 2.5. Synchrotron mid-IR absorption spectrum of $NH_3 \cdot BH_3$ collected at room temperature and (*a*) 1.5 GPa upon compression in comparison with (*b*) 0.3 GPa upon decompression in the spectral region 600 to 3800 cm^{-1}. The assignments of the fundamental modes are shown above the corresponding IR bands. The IR bands labeled with asterisks are overtones or combinations of lattice modes and/or internal modes (see text).

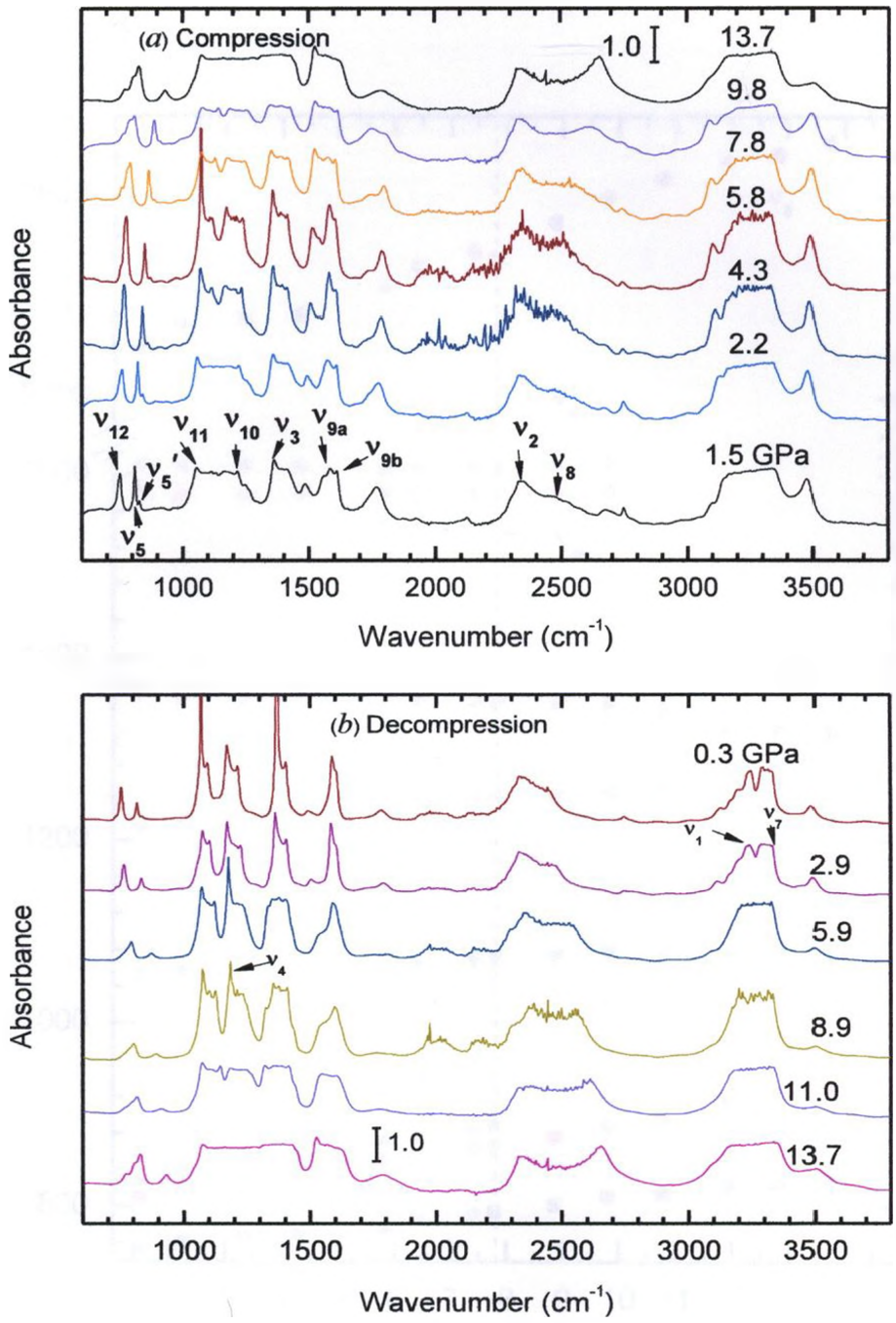

Fig. 2.6. Synchrotron mid-IR spectra of $NH_3 \cdot BH_3$ in the spectral range of 600 to 3800 cm^{-1} measured at room temperature for selected pressures (indicated in GPa above each spectrum) on (*a*) compression and (*b*) decompression. The absorbance has been normalized with respect to the beam current of the synchrotron light source. The spectra are offset vertically for clarity.

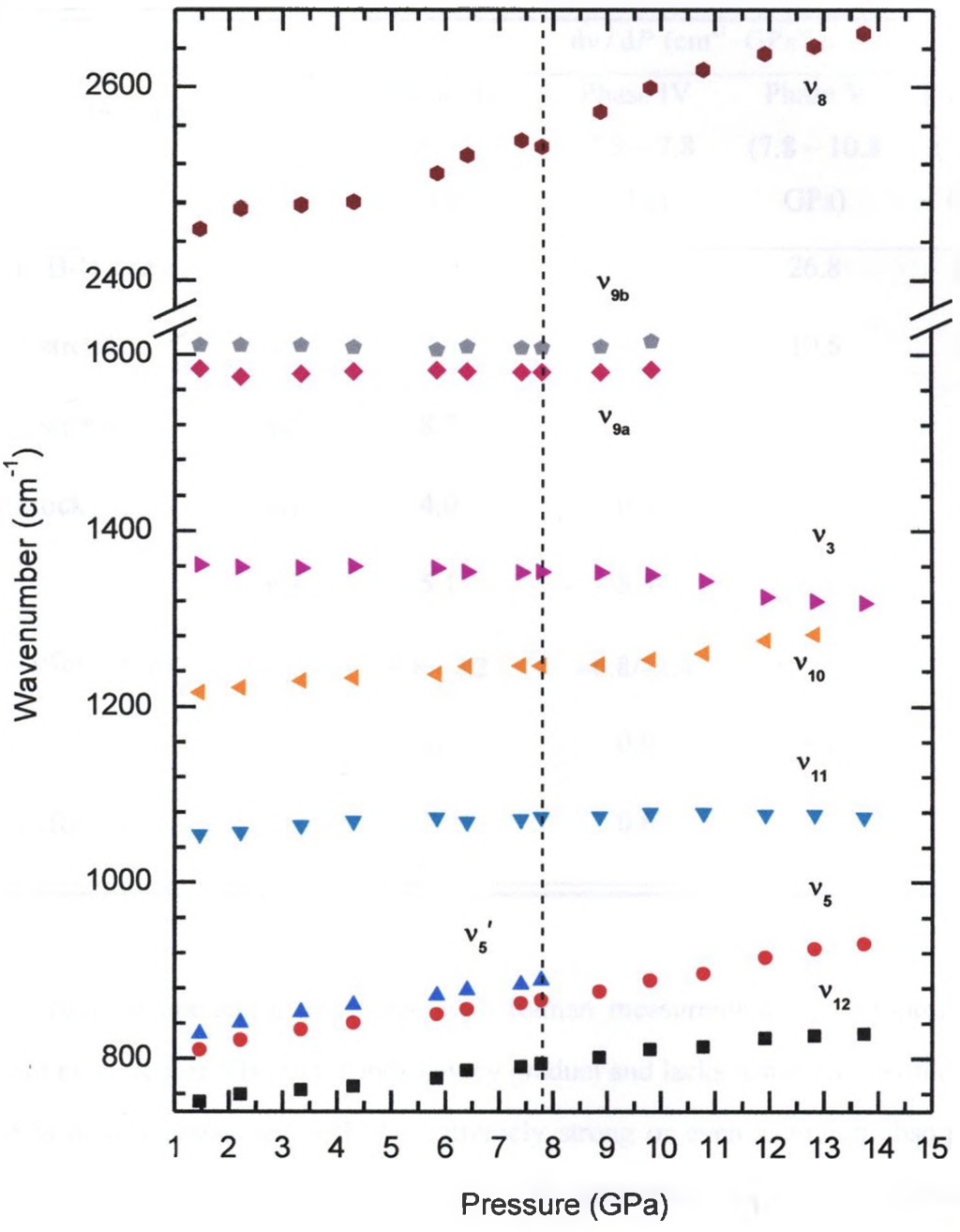

Fig. 2.7. Pressure dependences of IR frequencies of $NH_3 \cdot BH_3$ for internal modes on compression. Different symbols denote different IR origins with assignments labeled on the right hand side. The vertical dashed lines indicate one of the proposed phase boundaries.

Table 2.4. Pressure coefficients of the observed IR bands of $NH_3 \cdot BH_3$ on compression

IR bands		dv/dP ($cm^{-1} \cdot GPa^{-1}$)			
		Phase III (2.8 – 5.8 GPa)	Phase IV (5.8 – 7.8 GPa)	Phase V (7.8 – 10.8 GPa)	Phase VI (> 10.8 GPa)
Asym. B-H stretch	ν_8	12.6	14.6	26.8	12.4
^{11}B-N stretch	ν_5	7.6	8.1	10.6	8.5
^{10}B-N stretch	ν_5'	8.3			
NBH rock	ν_{11}	4.0	0.9	2.0	–1.6
	ν_{12}	5.1	5.5	6.5	2.6
NH_3 deformation	ν_{9a}/ν_{9b}	0.8/–2.2	–0.8/–1.4	1.4/3.8	
	ν_3	–0.1	0.0	–5.0	–3.8
BH_3 deformation	ν_{10}	2.9	0.6	6.6	8.0

GPa at room temperature. Compared with Raman measurements on compression, the pressure evolution of $NH_3 \cdot BH_3$ bands is very gradual and lacks distinctive profile changes, which is mainly associated with the extremely strong or even saturated absorptions in most of the spectral regions. In addition, the absorption is markedly enhanced as pressures increase such that the multiple bands in the spectral region of 1000 to 1600 cm^{-1} convolute to two broad bands at 13.7 GPa. As a result, it is difficult to visualize phase transitions from the IR spectra. The only discernable profile change occurs at 7.8 GPa as indicated by the broadening of the ν_{12} mode and by the enhanced intensity of the

ν_8 mode. However, the pressure dependences of the IR bands shown in Fig. 2.7 and Table 2.4 show roughly consistent pressure-induced phase transitions as established by our Raman measurements. Generally, most of the IR modes exhibit blue shifts with increasing pressure, consistent with the pressure-induced bond stiffening. For example, a pressure coefficient as large as 26.8 cm^{-1} GPa^{-1} is observed for the B-H stretching mode ν_8 in the pressure region of 7.8 to 10.8 GPa. Although the N-H stretching modes cannot be monitored due to strong absorption, the NH_3 deformation modes (ν_{9a}, ν_{9b} and ν_3) exhibit unambiguous red shifts, yielding consistent information obtained by Raman measurements interpreted as the weakening of N-H bonds with the formation of dihydrogen bonds.

After compressing $NH_3 \cdot BH_3$ to pressures as high as 13.7 GPa, we conducted IR measurements on decompression to near ambient pressures (e.g., 0.3 GPa). Selected spectra are depicted in Fig. 2.6*b* and compared with the compression data in Fig. 2.7. Apparently, the decompression data provide more information because the absorption is markedly reduced as the sample thins out after the compression-decompression cycle. For instance, when the pressure is reduced to 8.9 GPa, the previously saturated ν_4 and ν_{11} bands are resolved. Furthermore, IR bands ν_1 and ν_7 are clearly visible when decompressed to 2.9 GPa. Finally, as seen in Fig. 2.5*b*, all modes observed before compression at 1.5 GPa are recovered after decompression at 0.3 GPa. These observations indicate that the structural transformations upon compression are completely reversible in the entire pressure region, consistent with our Raman measurements.

2.3.5 Far-IR spectra of $NH_3 \cdot BH_3$

Using the unique synchrotron far-IR setup dedicated to *in situ* high-pressure measurements, we obtained the first far-IR $NH_3 \cdot BH_3$ absorption spectra at 13.5 GPa.

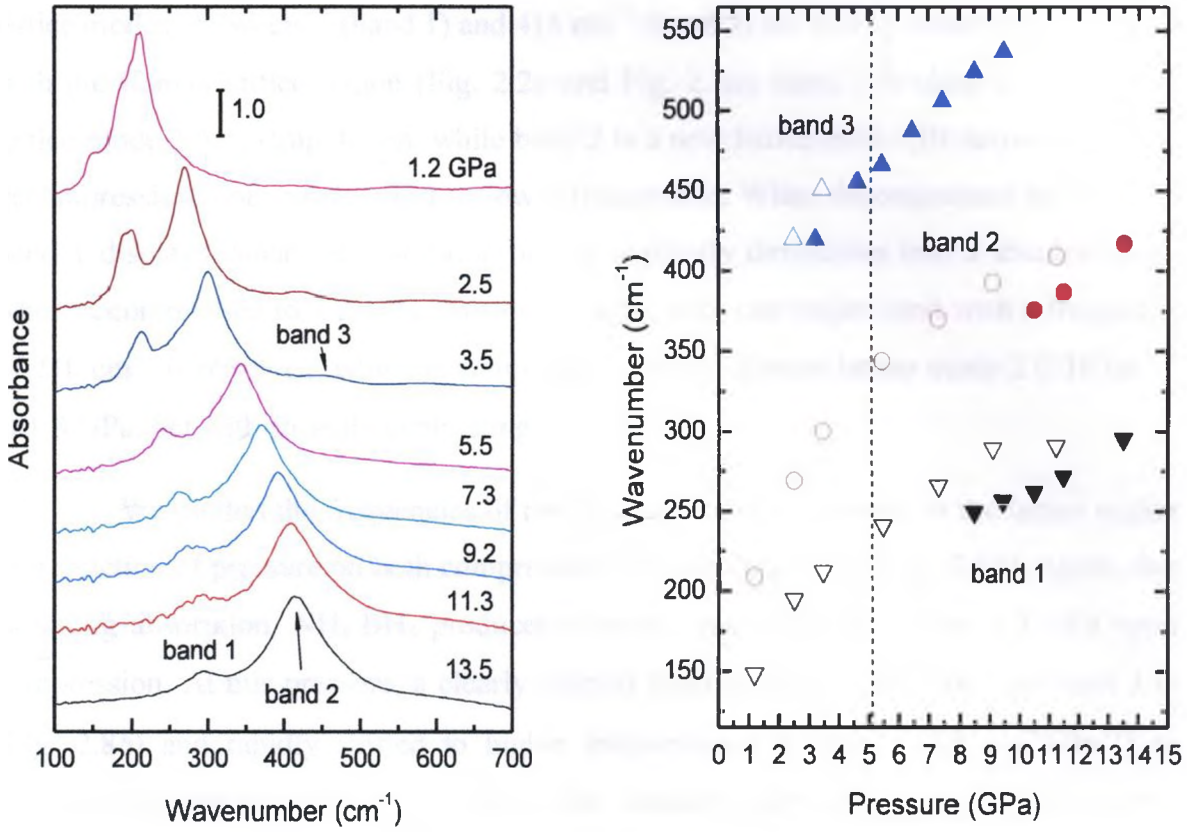

Fig. 2.8. (*a*) Synchrotron far-IR spectra of $NH_3{\cdot}BH_3$ in the spectral range of 100 to 700 cm^{-1} measured at room temperature for selective pressures (indicated in GPa above each spectrum) on decompression. The absorbance has been normalized with respect to the beam current of the synchrotron light source. The spectra are offset vertically for clarity. (*b*) Pressure dependences of IR frequencies of $NH_3{\cdot}BH_3$ for lattice modes. The solid symbols denote frequencies observed on compression while open symbols are for decompression. The vertical dashed lines indicate one of the proposed phase boundaries.

Similar to the mid-IR region, the lattice modes in the far-IR region at 100 to 600 cm^{-1} are overwhelmed by extremely strong absorptions that do not allow individual modes to be identified. Therefore, we performed a compression to 13.5 GPa stepwise (the IR spectra are not shown on compression) and then measured the IR absorption on decompression with selected spectra, shown in Fig. 2.8*a*. At the highest pressure, two

lattice modes at 294 cm^{-1} (band 1) and 415 cm^{-1} (band 2) are clearly observed. Compared with the Raman lattice region (Fig. 2.2*a* and Fig. 2.3*a*), band 1 is close to the Raman lattice mode 3 by extrapolation, while band 2 is a new lattice mode (IR active only). On decompression, both modes shift to lower frequencies. When decompressed to 3.5 GPa, band 1 displays enhanced absorption but subsequently diminishes into a shoulder peak when decompressed to 1.2 GPa. At this pressure, only one major band with a frequency of 210 cm^{-1} is observed, which is comparable with the Raman lattice mode 2 (219 cm^{-1}) at 1.8 GPa, but with strongly contrasting intensities.

We plotted the frequencies of the IR active modes observed in the lattice region as a function of pressure on both compression and decompression (Fig. 2.8*b*). Again, due to strong absorption, $NH_3 \cdot BH_3$ produces a broad, saturated band below 3.3 GPa upon compression. At this pressure, a clearly defined band evolved at 420 cm^{-1} [as band 3 in (Fig. 2.8*b*) and rapidly shifted to higher frequencies ($d\nu / dP = 18.8$ $cm^{-1}GPa^{-1}$) as pressures increased to 9.5 GPa when the intensity diminished almost completely. Interestingly, this band is not observed in this pressure region upon decompression, but only displays barely visible intensities below 3.5 GPa. As seen in (Fig. 2.8, bands 1 and 2 could not be distinguished from the saturated bands until the sample was compressed to 8.5 GPa, at which point they remain resolved up to the highest pressure. Upon decompression, however, these two modes exhibit different pressure dependences (i.e., smaller pressure coefficients) than when compressed, indicating that back transformation is more sluggish due to hysteresis. The pressure dependences of both these modes show a distinct change around 5.5 GPa, coinciding with one of the transition pressures established by our Raman measurements.

2.3.6 Discussion

In previous Raman studies of $NH_3 \cdot BH_3$ in the low pressure range (i.e., < 4 GPa),[22,26] two solid to solid transitions at 0.5 GPa and 1.4 GPa were found by Trudel,[26]

which is different from Custelcean's study[22] in which only one phase transition was found (at 0.8 GPa). This discrepancy may result from the differences in the hydrostatic conditions used in the two studies. Both of our Raman and IR measurements are in general agreement with these two studies in terms of phase regions, i.e., the spectroscopic features observed below and above 2 GPa roughly align with those before and after the phase transitions observed below 1.5 GPa in both studies, except that we extend the previously observed second high pressure phase from 4 GPa to approximately 5.8 GPa (we label this as phase III), which is in qualitative agreement with Lin's study.[28] Above this pressure, our Raman and IR measurements show two more phase transitions at 8.5 and 10.4 GPa, whereas the only transition observed in Lin's study is near 12 GPa.[28] In addition to the different boundaries, differences in Raman profiles, such as those in the lattice region, were also observed. One possible explanation is that our materials had a different purity and crystallinity: we used a reagent grade with a purity of 97% (purchased directly from Aldrich), while Lin *et al.*[28] used synthetic laboratory and heat-treated samples with an unknown purity. In addition, as discussed below, the phase transitions are characterized by subtle changes in the unit cell without major, irreversible modifications. Such transitions are generally sensitive to compression conditions and therefore may be affected by additional factors, such as kinetics. Nevertheless, our parallel measurements yielded reproducible and consistent results.

Then the remaining question is what are the possible structures of high-pressure phases of ammonia borane induced by compression and decompression. To our knowledge, no *in situ* high-pressure X-ray diffraction study of this complex has been reported. Therefore, these combined Raman and infrared spectroscopic measurements, especially in the lattice region, provide important insight for understanding the high-pressure structures of the ammonia borane complex. Unfortunately, Hess's recent low-temperature Raman study does not include lattice data[19] and lattice features were not analyzed in depth in any of the previous high-pressure Raman studies because of measurement limitations.[22,26]

For the phase below 2.4 GPa, the Raman measurement at 1.8 GPa (Fig. 2.2*a*)and IR measurement at 1.2 GPa (Fig. 2.8*a*) in the present study clearly indicate that there are at least two lattice modes associated with this phase. It is known that high pressures and low temperatures often induce similar phase transitions for many materials that have normal *P-T* phase diagrams. Therefore, to assume that the low-pressure phase has the same or similar crystal structure as the low-temperature orthorhombic phase is reasonable and can be examined for consistency by the observed spectroscopic features. Using factor group analysis, the orthorhombic structure ($Pmn2_1$) with two molecular units per unit cell has the following lattice modes:[19]

$$\Gamma_{\text{lattice vib.}}^{NH_3BH_3} = A_1 + A_2 + B_2$$

$$\Gamma_{\text{lattice lib.}}^{NH_3BH_3} = A_1 + 2A_2 + 2B_1 + B_2$$

where A_2 is Raman active and A_1, B_1, and B_2 are both IR and Raman active. Thus nine lattice modes are predicted with all Raman active modes and six are IR active. Apparently, the two lattice modes observed are only a subset of the predicted modes if the assumed crystal structure is correct. Since the notch filters used in our Raman system and far-IR setup at the synchrotron beamline do not allow unambiguous measurements below 100 cm^{-1}, it is possible that some additional lower frequency lattice modes were not detected. Nevertheless, the additional splitting features observed in the internal mode region, such as those for the ν_{11}, ν_9 and ν_7 modes, strongly suggest the structure is orthorhombic rather than tetragonal.

The next high pressure phase (phase III, 2.4 to 5.5 GPa) may have a structure very similar to the low-pressure orthorhombic phase. This is indicated by the similarity of the lattice profile both in the Raman and IR measurements as well as in the more prominent splittings observed for the ν_{12}, ν_{11}, ν_8 and ν_9 modes. These observations strongly suggest enhanced intermolecular interactions as a result of compression as manifested by the largest pressure coefficient (Table 2.2) observed among all pressure regions. In addition, the bending deformation modes for BH_3 and NH_3 (i.e., ν_{10} and ν_9,

respectively) at 2.4 GPa have a broad profile, indicating some degree of rotational disorder for NH_3-BH_3 along its molecular axis at this pressure. Upon compression, both modes split into narrower doublet peaks that suggests that the free rotation of the BH_3 and NH_3 groups is likely hindered by pressure and thus the complex may undergo a rotational disorder-order process in this pressure region. We note that our observation is in contrast to that of Lin's where the splitting of these modes is lacking in this pressure region.[28]

From 5.5 to 8.5 GPa, the complex undergoes a more prominent structural modification. In this region, up to four Raman lattice modes and three IR lattice modes are observed. The Raman frequencies are 139, 201, 246, 301 cm^{-1} at 5.5 GPa, while the IR frequencies observed at the same pressure are 241, 344, and 467 cm^{-1}. However, the IR bands at 241 and 344 cm^{-1} measured during decompression are known to exhibit higher frequencies than those measured on compression due to hysteresis. Therefore, we linearly extrapolated the high-pressure frequencies of IR bands 1 and 2 (Fig. 2.8*b*) to 5.5 GPa to obtain the corrected 'compression' data (215 and 311 cm^{-1}). As a result, these two major IR bands are roughly aligned with the two major Raman bands at 201 and 301 cm^{-1} as observed in other pressure regions, suggesting the new modes are 139 and 246 cm^{-1} for Raman measurements and 467 cm^{-1} for IR measurements. Again, because the observed Raman and IR modes are generally a subset of the predicted ones, it is difficult to perform a full factor group analysis without crystal structures. However, these observations can temporarily rule out a significant change to the factor group of $NH_3 \cdot BH_3$ crystal lattice, especially changes to centrosymmetric groups such as D_{2h} for orthorhombic or C_{2h} for monoclinic systems. The observation of new lattice modes can be interpreted as enhanced correlation field interactions within the C_{2v} factor group or even lower symmetry groups, such as those for monoclinic systems. X-ray diffraction measurements are required to understand the detailed structures of this $NH_3 \cdot BH_3$ phase.

Above 8.5 GPa, both the Raman and IR spectra are characterized by significant profile broadening in almost all spectral regions. Split Raman modes are merged into

broad bands with significantly reduced intensity (e.g., ν_{11}, ν_9 and ν_8), while the lattice modes measured both by Raman and IR spectroscopy become much weaker and broad. Above 10.4 GPa, the number of lattice modes in both Raman and IR measurements is reduced, while the remaining modes undergo continuing weakening and broadening. These observations suggest that the $NH_3 \cdot BH_3$ complex is transforming from an ordered crystalline structure to a possibly disordered or ultimately amorphous structure when compressed to high enough pressures. The phase between 8.5 and 10.4 GPa can be considered as an intermediate phase for the disordering process, while the phase above 10.4 GPa is characterized by significant disordering. Although pressure gradients at high pressure may contribute to the profile broadening, our ruby fluorescence measurements across the sample suggest that the non-hydrostatic effect contributes only very insignificantly to this broadening.

In Lin's[28] analysis of the possible high-pressure structures based on the features of a few characteristic internal modes and the observation of two lattice modes, it is proposed that the crystal structure is unaltered in the entire pressure region.[28] However, the additional lattice modes observed by our Raman and IR measurements clearly indicates that there is a possible pressure-induced formation of new crystal structures. They further speculate that the dimerization of ammonia borane complex may be associated with one of the high pressure phases. Again, if dimerization occurs, more internal modes with different vibrational frequencies are expected. In addition, dimerization implies that the number of the molecular unit Z halves per unit cell, which is contradictory to the observation that there was an increase in the number of lattice mode. *In situ* X-ray diffraction measurements are required to resolve the discrepancy between the structural interpretation of the two spectroscopic studies.

Finally, it is clear that both the Raman and IR measurements show that the pressure-induced transformations of the $NH_3 \cdot BH_3$ complex are reversible upon decompression. The almost identical spectroscopic details in both Raman and IR internal mode regions before and after compression indicate that the chemical structure of the complex is completely unaltered by pressure and thus $NH_3 \cdot BH_3$ is stable (i.e., no

hydrogen release) up to the highest pressure yielded in this study. However, the different profiles of the lattice modes from both Raman and IR measurements suggest that crystalline structures may have been modified by pressure, even if very slightly. In addition, hysteresis has been observed in most of the pressure regions upon decompression. Our observations agree with those of Custelcean,[22] who also found all pressure-induced transformations were reversible at less than 4 GPa, but that there was some hysteresis. Hysteresis is typically considered to be a result of kinetics-mediated transformations characterized by some barriers. To overcome the kinetic barrier, it would be interesting to investigate the pressure-induced transformations at elevated temperatures.

2.4 Conclusions

Using Raman and synchrotron IR spectroscopy, we investigated the pressure behaviour of the ammonia borane complex as a promising hydrogen storage material. In the low pressure region (<2 GPa), we discovered that the complex undergoes a structural transformation from a disordered tetragonal to an ordered, possibly orthorhombic, structure, consistent with previous Raman studies. Upon further compression, our Raman and IR measurements identified several solid-to-solid transformations with phase boundaries that roughly occurred at 2.4, 5.5, 8.5 and 10.4 GPa. These transformations are characterized by distinctive profiles and the pressure dependences of characteristic modes. Spectroscopic measurements on decompression suggest that these pressure-induced transformations are reversible within the intact chemical structure of the $NH_3{\cdot}BH_3$ complex, with possible modifications to the crystal structures. Analysis of combined Raman and IR measurements, especially the lattice features, suggests that $NH_3{\cdot}BH_3$ structures below 5.5 GPa resemble a low-pressure orthorhombic structure, while in the higher pressure regions, NH_3BH_3 complexes may undergo transformations to disordered or amorphous structures. Detailed high-pressure structural information needs to be confirmed by *in situ* X-ray diffraction measurements.

2.5 Acknowledgements

YS acknowledges support from a Discovery Grant and a Research Tools and Instruments Grant from the Natural Science and Engineering Research Council of Canada, the Leaders Opportunity Fund from the Canadian Foundation for Innovation and the Early Researcher Award from the Ontario Ministry of Research and Innovation. IR measurements were performed at the U2A beamline at the NSLS at BNL. The U2A beamline is supported by COMPRES, the Consortium for Materials Properties Research in Earth Sciences under NSF Cooperative Agreement EAR06-49658, U.S. Department of Energy (DOE), (CDAC), and NSF (DMR).

2.6 References

(1) Xiong, Z. T.; Yong, C. K.; Wu, G. T.; Chen, P.; Shaw, W.; Karkamkar, A.; Autrey, T.; Jones, M. O.; Johnson, S. R.; Edwards, P. P.; David, W. I. F. *Nature Mat.* **2008**, *7*, 138.

(2) Dixon, D. A.; Gutowski, M. *J. Phys. Chem. A* **2005**, *109*, 5129.

(3) Stowe, A. C.; Shaw, W. J.; Linehan, J. C.; Schmid, B.; Autrey, T. *Phys. Chem. Chem. Phys.* **2007**, *9*, 1831.

(4) Hu, M. G.; Geanangel, R. A.; Wendlandt, W. W. *Thermochim. Acta* **1978**, *23*, 249.

(5) Sit, V.; Geanangel, R. A.; Wendlandt, W. W. *Thermochim. Acta* **1987**, *113*, 379.

(6) Wolf, G.; Baumann, J.; Baitalow, F.; Hoffmann, F. P. *Thermochim. Acta* **2000**, *343*, 19.

(7) Baitalow, F.; Baumann, J.; Wolf, G.; Jaenicke-Rossler, K.; Leitner, G. *Thermochim. Acta* **2002**, *391*, 159.

(8) Baumann, J.; Baitalow, E.; Wolf, G. *Thermochim. Acta* **2005**, *430*, 9.

(9) Stephens, F. H.; Pons, V.; Baker, R. T. *Dalton Trans.* **2007**, 2613.

(10) Haaland, A. *Angew. Chem., Int. Ed. Engl.* **1989**, *28*, 992.

(11) Klooster, W. T.; Koetzle, T. F.; Siegbahn, P. E. M.; Richardson, T. B.; Crabtree, R. H. *J. Am. Chem. Soc.* **1999**, *121*, 6337.

(12) Thorne, L. R.; Suenram, R. D.; Lovas, F. J. *J. Chem. Phys.* **1983**, *78*, 167.

(13) Kathmann, S. M.; Parvanov, V.; Schenter, G. K.; Stowe, A. C.; Daemen, L. L.; Hartl, M.; Linehan, J.; Hess, N. J.; Karkamkar, A.; Autrey, T. *J. Chem. Phys.* **2009**, *130,* 024507.

(14) Hughes, E. W. *J. Am. Chem. Soc.* **1956**, *78*, 502.

(15) Shore, S. G.; Parry, R. W. *J. Am. Chem. Soc.* **1955**, *77*, 6084.

(16) Hoon, C. F.; Reynhardt, E. C. *J. Phys. C* **1983**, *16*, 6129.

(17) Demaison, J.; Lievin, J.; Csaszar, A. G.; Gutle, C. *J. Phys. Chem. A* **2008**, *112*, 4477.

(18) Bowden, M. E.; Gainsford, G. J.; Robinson, W. T. *Aust. J. Chem.* **2007**, *60*, 149.

(19) Hess, N. J.; Bowden, M. E.; Parvanov, V. M.; Mundy, C.; Kathmann, S. M.; Schenter, G. K.; Autrey, T. *J. Chem. Phys.* **2008**, *128*, 034508.

(20) Cho, H.; Shaw, W. J.; Parvanov, V.; Schenter, G. K.; Karkamkar, A.; Hess, N. J.; Mundy, C.; Kathmann, S.; Sears, J.; Lipton, A. S.; Ellis, P. D.; Autrey, S. T. *J. Phys. Chem. A* **2008**, *112*, 4277.

(21) Taylor, R. C.; Cluff, C. L. *Nature* **1958**, *182*, 390.

(22) Custelcean, R.; Dreger, Z. A. *J. Phys. Chem. B* **2003**, *107*, 9231.

(23) Sawodny, W.; Goubeau, J. *Z. Phys. Chem. (Frankfurt)* **1965**, *44*, 227.

(24) Dillen, J.; Verhoeven, P. *J. Phys. Chem. A* **2003**, *107*, 2570.

(25) Allis, D. G.; Kosmowski, M. E.; Hudson, B. S. *J. Am. Chem. Soc.* **2004**, *126*, 7756.

(26) Trudel, S.; Gilson, D. F. R. *Inorg. Chem.* **2003**, *42*, 2814.

(27) Hemley, R. J.; Mao, H. K. *In High-Pressure Phenomena,* Proceedings of the International School of Physics Enrico Fermi, Vol. 147; Hemeley, R. J., Chiarotti, G. L., Bernasconi, M., Ulivi, L., Eds.; IOS Press: Amsterdam, 2002; p. 3.

(28) Lin, Y.; Mao, W. L.; Drozd, V.; Chen, J. H.; Daemen, L. L. *J. Chem. Phys.* **2008**, *129*, 234509.

(29) Mao, H. K.; Xu, J.; Bell, P. M. *J. Geophy. Res.* **1986**, *91*, 4673.

(30) Smith, J.; Seshadri, K. S.; White, D. *J. Mol. Spectrosc.* **1973**, *45*, 327.

(31) Jagielska, A.; Moszynski, R.; Piela, L. *J. Chem. Phys.* **1999**, *110*, 947.

Chapter 3 *In situ* high-pressure study of calcium borohydride by Raman and IR spectroscopy

3.1 Introduction

Recently, alkaline earth metal borohydrides [e.g., $Ca(BH_4)_2$] have been the focus of many studies because of their potential use for hydrogen storage applications.[1-8] Among them, $Ca(BH_4)_2$, which contains 9.7 wt % hydrogen, has demonstrated partially reversible dehydriding and rehydriding ability at 620 – 660 K and 700 bar, thus is suitable for reversible applications.[9-10] The dehydriding process results in H_2, CaH_2, CaB_6 and/or B, from which $Ca(BH_4)_2$ can be synthesized under moderate pressure and temperature conditions.[9-10]

In addition, calcium borohydride can also be synthesized in several other ways. In 1955, Wiberg first reported the preparation of $Ca(BH_4)_2$ through the reaction of diborane with calcium hydride[11] or alkoxides.[12] A more convenient approach was developed by Mikheeva[13] later by using an exchange reaction between $CaCl_2$ and $NaBH_4$ in THF to form $Ca(BH_4)_2 \cdot 2THF$, from which the THF adduct could be removed easily in vacuum upon heating. Through the reaction of $CaCl_2$ with another alkali-borohydride $LiBH_4$, $Ca(BH_4)_2$ was prepared by Konoplev.[14] More recently, synthesis of $Ca(BH_4)_2$ by reacting CaH_2 with MgB_2under moderate H_2 pressures and temperatures, was reported by Barkhordarian.[15]

Depending on the synthetic technique and detailed conditions, different crystal structures were observed for $Ca(BH_4)_2$ by X-ray diffraction measurements. $Ca(BH_4)_2$ prepared by desolvation of the commercial $Ca(BH_4)_2 \cdot 2THF$ at 433K for 1 hour was reported by Miwa[5] to be α-$Ca(BH_4)_2$ with space group *Fddd* (Fig. 3.1*a*). α-phase is believed to the primary stable phase of $Ca(BH_4)_2$ at lower temperatures. However, a structure with space group *F*2*dd* was also claimed for α-phase by Filinchuk using quantitative Rietveld refinement.[1] Upon heating α-$Ca(BH_4)_2$ to about 400 K, a phase

transition to β-phase with a space group is $P\bar{4}$ as shown in Fig. 3.1, was observed.[16-17] This transition from α-phase to β-phase was found to be irreversible. During the heating process of α-$Ca(BH_4)_2$, several more phases (γ and σ phases) are also reported,[16-17] but their structures are still unknown.

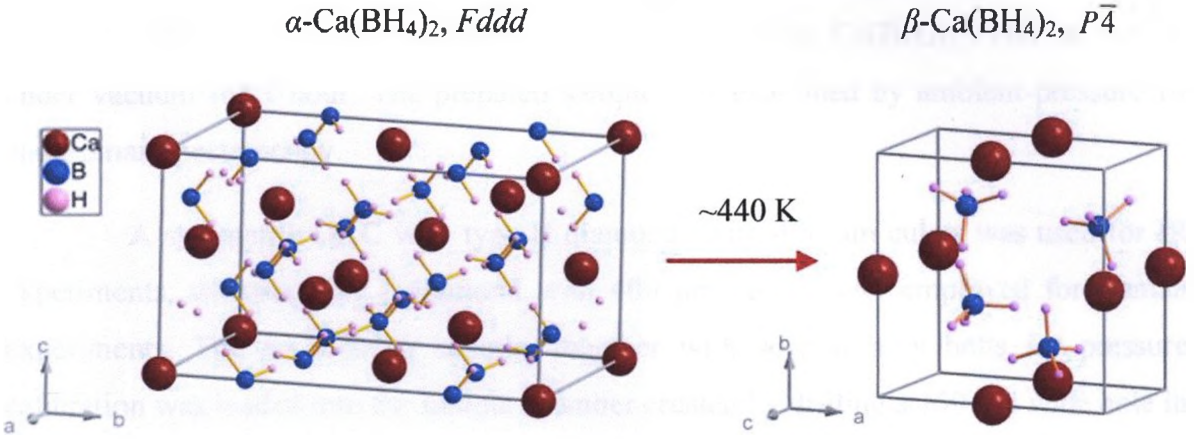

Fig. 3.1. Thermo-induced phase transition from α-$Ca(BH_4)_2$ with *Fddd* space group to β-$Ca(BH_4)_2$ with $P\bar{4}$ space group at ~440 K. The color codes for atoms are: calcium (red), boron (blue), hydrogen (pink).

Although $Ca(BH_4)_2$ has been studied extensively at ambient pressure, little is known about the structures and properties of $Ca(BH_4)_2$ at high pressure region. As the development of hydrogen storage materials by high pressure tuning has demonstrated great promises, understanding the structures, stabilities as well as reactivities under high pressure is of fundamental important. In this study, we investigated high-pressure behaviors of α-$Ca(BH_4)_2$ by reporting the first IR and Raman spectroscopic data up to 10 GPa in diamond anvil cells. From both the IR and Raman data, several new pressure-induced phase transitions were identified. The reversibility of these phase transitions was also examined. Our study thus contribute to the continuing development of $Ca(BH_4)_2$ based hydrogen storage materials.

3.2 Experimental

3.2.1 Sample preparation

The starting material was prepared from commercial $Ca(BH_4)_2 \cdot 2THF$ (98%, Aldrich). Addict-free α-$Ca(BH_4)_2$ was obtained by heating $Ca(BH_4)_2 \cdot 2THF$ at 433 K under vacuum for 1 hour. The prepared sample was examined by ambient-pressure IR and Raman spectroscopy.

A symmetric DAC with type II diamonds with 400 μm culets was used for IR experiments, whereas type I diamond with 400 μm culets were employed for Raman experiments. The α-$Ca(BH_4)_2$ sample, together with several ruby balls for pressure calibration was loaded into the sample chamber created by drilling a 150 μm wide hole in a 70 μm thick stainless steel gasket. KBr crystals were also loaded to dilute sample in IR measurements. Due to the sensitivity of $Ca(BH_4)_2$ to water, all loadings were done in a nitrogen-filled glove-box (MBraun LABmaster 130), where both water and moisture levels were maintained below 10 ppm. No pressure transmission media were used, and our ruby spectra profiles of different ruby chips across sample chamber indicated no obvious non-hydrostatic effects in the studied pressure region.

3.2.2 High-pressure mid-IR measurements

Mid-IR experiments were carried out with a customized IR micro-spectroscopy system in our lab. Basically, a commercial Fourier transform IR (FTIR) spectrometer from Bruker Optics Inc. (Model Vertex 80v) equipped with a Globar IR light source constitutes the main component of the micro-IR system, which is operated under a vacuum of <5 mbar, such that the absorption by H_2O and CO_2 is efficiently removed. Collimated IR beam with variable diameters set by apertures ranging from 0.25 mm to 8 mm was directed into a relay box through a KBr window on the spectrometer. The beam was then focused onto the sample in DAC by an iris optics and 15 × reflective objective

lens with a numerical aperture of 0.4. The DAC on the sample XYZ precision stage was aligned with the aid of an optical microscope equipped with an objective lens with variable magnifications (0.75× – 3×) and a 20 × eyepiece from Edmond Optics. The size

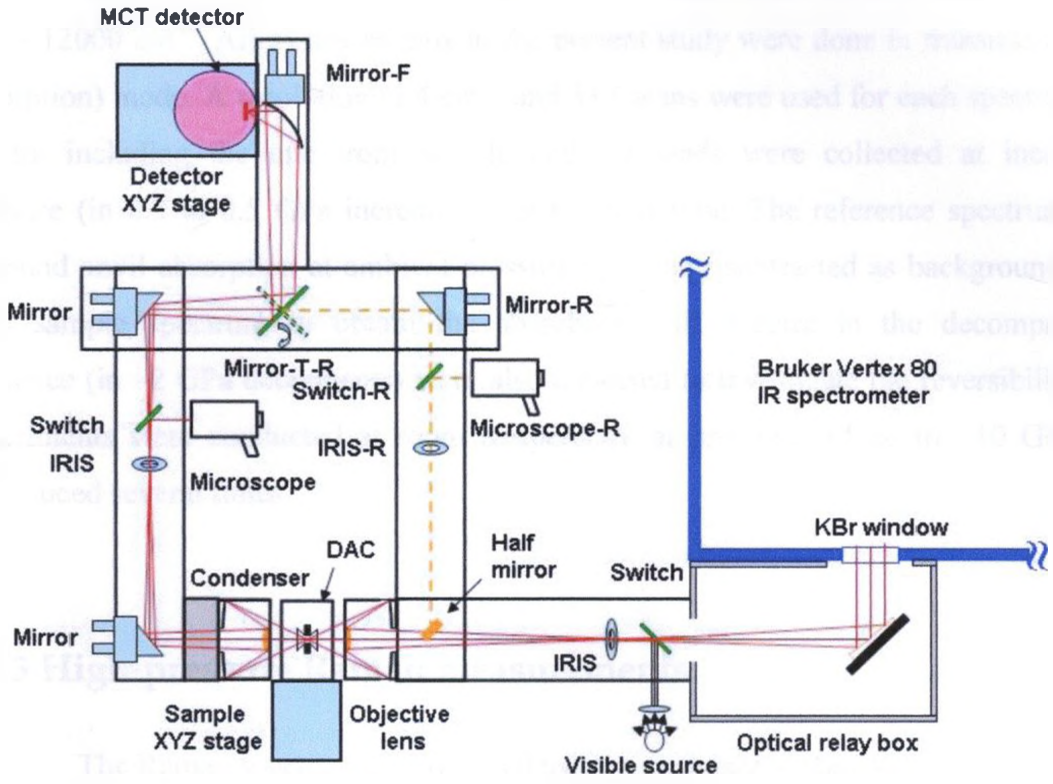

Fig. 3.2. Schematic diagram of the customized FTIR system in the Song lab. The IR spectrometer (model Vertex 80) from Bruker was operated under vacuum. The collimated IR beam comes out through a KBr window. The rest of the optics are purged using CO_2-free dry air in closed boxes or frames. All major optical components are labeled. Those with '-R' and half mirror are for reflection measurements while the rest for transmission/absorption measurements. 'Switch' refers to switchable mirrors for illumination purpose. 'Mirror-T-R' is a mirror used to switch between transmission and reflection modes. 'Mirror-F' is used to focus the IR signal to the detector.

of the IR beam was set to be identical to the entire sample size (e.g., ~150 μm) by a series of iris apertures. The transmitted IR beam was collected by another identical reflective objective as condenser, and was directed to a mid-band mercury cadmium telluride (MCT) detector equipped with ZnSe window that allows measurements in the spectral range of 600 – 12000 cm^{-1}. All measurements in the present study were done in transmission (or absorption) mode. A resolution of 4 cm^{-1} and 512 scans were used for each spectrum. IR spectra including the one from sample and diamonds were collected at increasing pressure (in 0.3 to 0.5 GPa increments) at the first time. The reference spectrum, i.e., diamond anvil absorption at ambient pressure, was later subtracted as background from each sample spectrum to obtain the absorbance. IR spectra in the decompression sequence (in ~2 GPa decrements) were also collected to investigate the reversibility. All experiments were conducted at room temperature at pressures of up to ~10 GPa and reproduced several times.

3.2.3 High-pressure Raman measurements

The Raman spectra were collected using a customized Raman system in our lab. A 514 nm Ar^{+} ion laser was used as exciting source. The maximum power of this laser was approximately 3 Watt and appropriate filters were used to ensure that only a few milli-Watts of laser power is incident on the sample to minimize possible fluorescence. The signal was detected with backscattering geometry by a liquid nitrogen cooled charge-coupled device (CCD) detector. The whole system was calibrated by neon lines. An 1800 $grating^{-1}$·mm grating with a 1 cm^{-1} resolution was used in this experiment. To avoid the strong first order Raman mode of diamond at 1334 cm^{-1}, the spectra were collected in ranges of 100 - 1300 and 1355 - 2800 cm^{-1} in several dispersive collection windows. For each spectrum, a collection time of 60 s was employed. Pressure was increased at room temperature incrementally from ambient pressure to near 10 GPa, following by a decompression in ~2 GPa decrements.

3.3 Results and discussion

3.3.1 Mid-IR spectrum of $Ca(BH_4)_2$ at ambient pressure

Mid-IR spectrum of the prepared calcium borohydride was collected at ambient condition and is depicted in Fig. 3.3. According to the previous XRD analysis,[5] $Ca(BH_4)_2$ prepared by the method described in this study is addict-free crystalline α-phase. At ambient conditions, α-$Ca(BH_4)_2$ has an orthorhombic structure with space group *Fddd* (D_{2h}^{24}).[5] In each unit cell, there are eight formula units with Ca^{2+} cations on D_2 sites and BH_4^- anions on C_2 sites. Upon factor group analysis, 66 optical modes are predicted for α-$Ca(BH_4)_2$, out of which 36 modes are associated with internal BH_4^{-1} vibrations, with the following irreducible representation:

$$\Gamma_{\text{internal vib.}}^{BH_4^-} = 5A_g + 4B_{1g} + 5B_{2g} + 4B_{3g} + 5A_u + 4B_{1u} + 5B_{2u} + 4B_{3u} \quad (3.1)$$

where all gerade modes are Raman active and ungerade modes except for A_u are IR active. These 36 internal modes can be considered to arise from the vibrations of a free BH_4^- ion due a static field splitting and a correlation field effect. However, according to previous studies,[19-21] the correlation field effect does not give measurable splitting for internal vibrations of BH_4^- at ambient pressure. Therefore, we assign these modes based on static field splitting from the original T_d symmetry ($A + E + 2T_2$), which would result in 9 both IR and Raman active modes ($5A + 4B$). Modes assignments for the ambient-pressure IR spectrum are labeled in Fig. 3.3 and listed in Table 3.1.

As shown in IR spectrum (Fig. 3.3), most of active modes are observed as predicted, in good agreement with previously reported data. The absorption features in 1000 - 1450 cm^{-1} can be assigned as the deformations modes of BH_4^- ion. For example, IR bands at 1079 cm^{-1} (ν_{4c}), 1114 cm^{-1} (ν_{4b}), 1201 cm^{-1} (ν_{4a}) are associated with out-of-plane BH_4^- bending, while the bands at 1289 cm^{-1} (ν_{2b}), 1324 cm^{-1} (ν_{2a}) are associated with in-plane BH_4^- bending.

Table 3.1. Assignment of fundamental IR modes of α-$Ca(BH_4)_2$

This work[a]	300K[b]	80K[b]	Mode[c]	Assignment	Local symmetry	T_d symmetry
	2415	2426	ν_{3a}	Asym. B-H stretch	*B*	T_2
	2356	2358	ν_{3b}	Asym. B-H stretch	*A*	T_2
2332	2332	2332	ν_{3c}	Asym. B-H stretch	*B*	T_2
2262[d]	2273	2271	ν_1	Sym. B-H stretch	*A*	*A*
1324	1327	1330	ν_{2a}	In-plane BH_4^- bend	*A*	*E*
1289	1241	1244	ν_{2b}	In-plane BH_4^- bend	*A*	*E*
1201	1204	1212	ν_{4a}	Out-of-plane BH_4^- bend	*B*	T_2
1114	1117	1119	ν_{4b}	Out-of-plane BH_4^- bend	*A*	T_2
1079	1089	1093	ν_{4c}	Out-of-plane BH_4^- bend	*B*	T_2

[a] Measured at room temperature and ambient pressure.

[b] Reference 19, measured at ambient pressure.

[c] The labels of 'a', 'b', 'c' are arbitrary.

[d] Measured at 1.4 GPa.

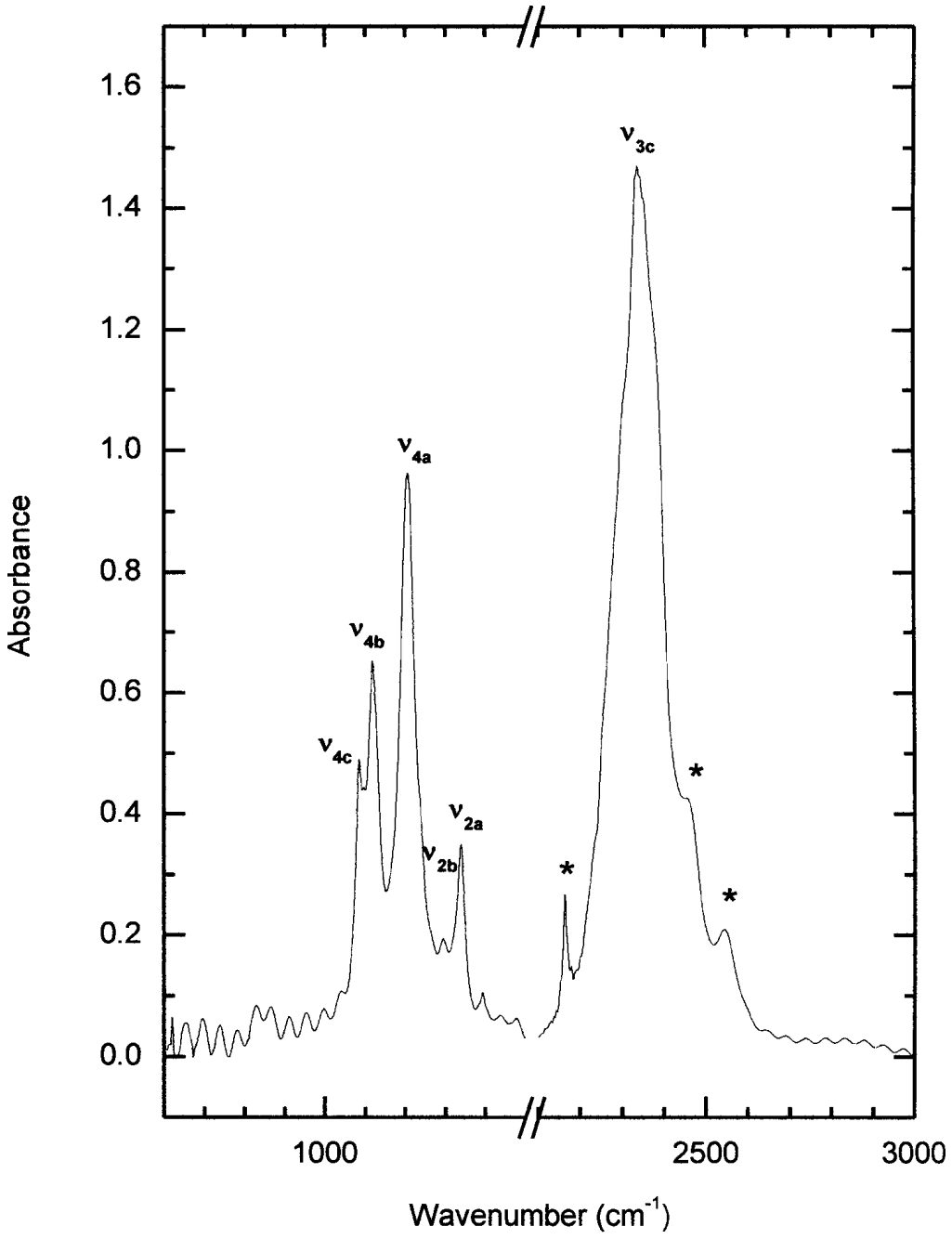

Fig. 3.3. IR absorption spectrum of α-$Ca(BH_4)_2$ at ambient condition in the spectral region of 600 – 3000 cm^{-1}. Bands labeled with asterisks are overtones or combinations of fundamental IR modes.

In the region of 2000 - 2400 cm^{-1}, the strongest absorption band with a broad profile at 2332 cm^{-1} can be assigned as an asymmetric B-H stretching (v_{3c}). Besides fundamental bands, additional IR bands are also observed as a result of overtones and/or combinations of fundamental modes, which are labeled with asterisks in Figure 3.1. For instance, a band is observed at 2159 cm^{-1}, which is very close to the overtone of v_{4c} (1080 cm^{-1}). Similarly, the bands at 2520 and 2450 cm^{-1} are likely to be combinations involving v_{2a} (1334 cm^{-1}), v_{2b} (1289 cm^{-1}) and v_{4a} (1201 cm^{-1}) modes, as well as $v_{4a} + v_{2a}$ and $v_{4a} + v_{2b}$, respectively.

3.3.2 Mid-IR spectra of $Ca(BH_4)_2$ during compression

Mid-IR spectra of $Ca(BH_4)_2$ were collected from ambient pressure up to 9.3 GPa. Selected spectra are shown in Fig. 3.4 in the region of 800 - 3000 cm^{-1}. For convenience, the IR spectra of $Ca(BH_4)_2$ are discussed in two regions based on its molecular nature: the BH_4^- deformation region, and the B-H stretching and combination modes region.

In the region below 1450 cm^{-1}, a new band (labeled as v_5) appears at 2.4 GPa upon compression, suggesting a solid-to-solid phase transition. This phase transition is further evidenced by the sudden broadening of v_{3c} band from 2.2 to 2.4 GPa. In addition, the new mode (v_5) as a shoulder of v_{4b} was resolved at 1121 cm^{-1}. As pressure was increased to 6.6 GPa, two more bands (labeled as v_7 and v_8) were observed, indicating another possible phase transition. Furthermore, the v_{4c} mode was also accompanied by a new, weak shoulder peak (labeled as v_9) at 6.6 GPa, but the position of v_9 mode could not be unambiguously determinate until 7.3 GPa.

Although four B-H stretching modes are predicted, only one band (v_{3c}) is clearly observed below 1.4 GPa. At 1.4 GPa, a shoulder peak, which can be assigned as a symmetric B-H stretching mode v_1, first appears at 2262 cm^{-1}. As pressure increases, both

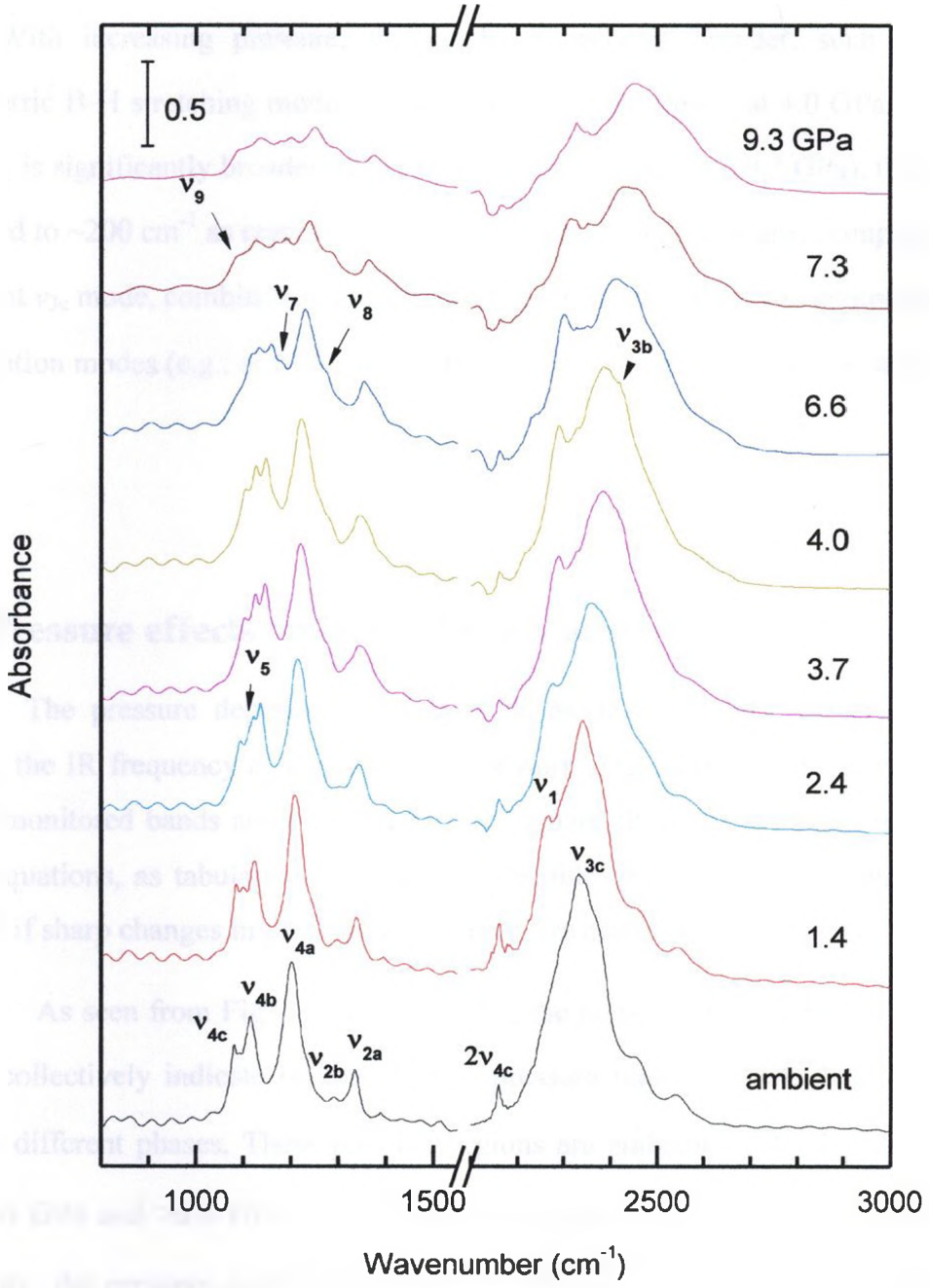

Fig. 3.4. Mid-IR spectra of $Ca(BH_4)_2$ at room temperature and selected pressures on compression in the region of 800 to 3000 cm^{-1}. The pressure in GPa are labeled for each spectrum. The assignments of IR modes are labeled for several spectra. The spectra are offset vertically for clarity.

the v_1 and v_{3c} modes shift to higher frequency and become better deconvoluted from each other. With increasing pressure, the v_{3c} band becomes broader, such that another asymmetric B-H stretching mode, v_{3b}, also becomes discernible at 4.0 GPa. At 6.6 GPa, bond v_{3c} is significantly broadened. At the highest pressure (i.e., 9.3 GPa), the bandwidth increased to ~200 cm^{-1} as compared to ~120 cm^{-1} at ambient pressure. Compared with the dominant v_{3c} mode, combination modes remain relatively weak. Upon compression, some combination modes (e.g., at 2520 and 2450 cm^{-1}) become obscured by the strong v_{3c} band nearby.

3.3.3 Pressure effects on IR modes of $Ca(BH_4)_2$

The pressure dependence of each IR mode of $Ca(BH_4)_2$ was examined by plotting the IR frequency as a function of pressure (Fig. 3.5). The pressure coefficients for the monitored bands are analyzed by least-square fitting of the experimental data to linear equations, as tabulated in Table 3.2. Possible phase transitions could be further inferred if sharp changes in pressure coefficients are observed.

As seen from Fig. 3.5 and Table 3.2, the pressure dependence of the major IR modes collectively indicate several distinct pressure regions in which $Ca(BH_4)_2$ could exist in different phases. These pressure regions are ambient – 2.4 GPa, 2.4 – 3.7 GPa, 3.7 – 6.6 GPa and >6.6 GPa, which we label as phases I, II, III and IV, respectively. Generally, the pressure coefficients of all stretching and deformation modes decrease along phase transformations from phase I to phase II, and then to phase III. From phase III to phase IV, however, most pressure coefficients except the one for v_5 dramatically increase. For instance, the pressure coefficient for the most intense band v_{3c} changes from 20.1 $cm^{-1}\cdot GPa^{-1}$ to 15.6 $cm^{-1}\cdot GPa^{-1}$ upon compression from phase I to phase II, then

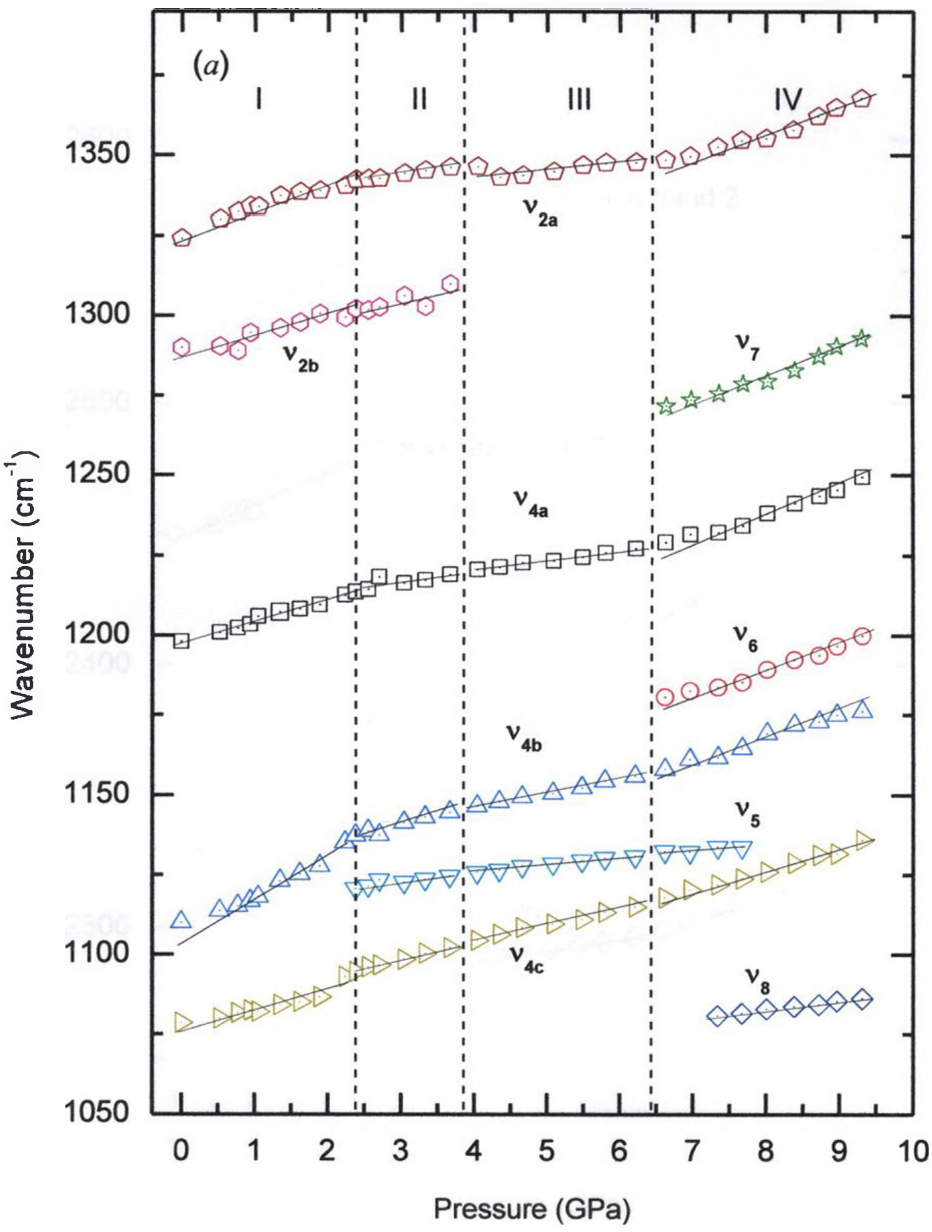
(a)
I
II
III
IV
1350
1300
1250
1200
1150
1100
1050
Wavenumber (cm^{-1})
0
1
2
3
4
5
6
7
8
9
10
Pressure (GPa)
ν_{2a}
ν_{2b}
ν_{7}
ν_{4a}
ν_{6}
ν_{4b}
ν_{5}
ν_{4c}
ν_{8}

Fig. 3.5.

Continued

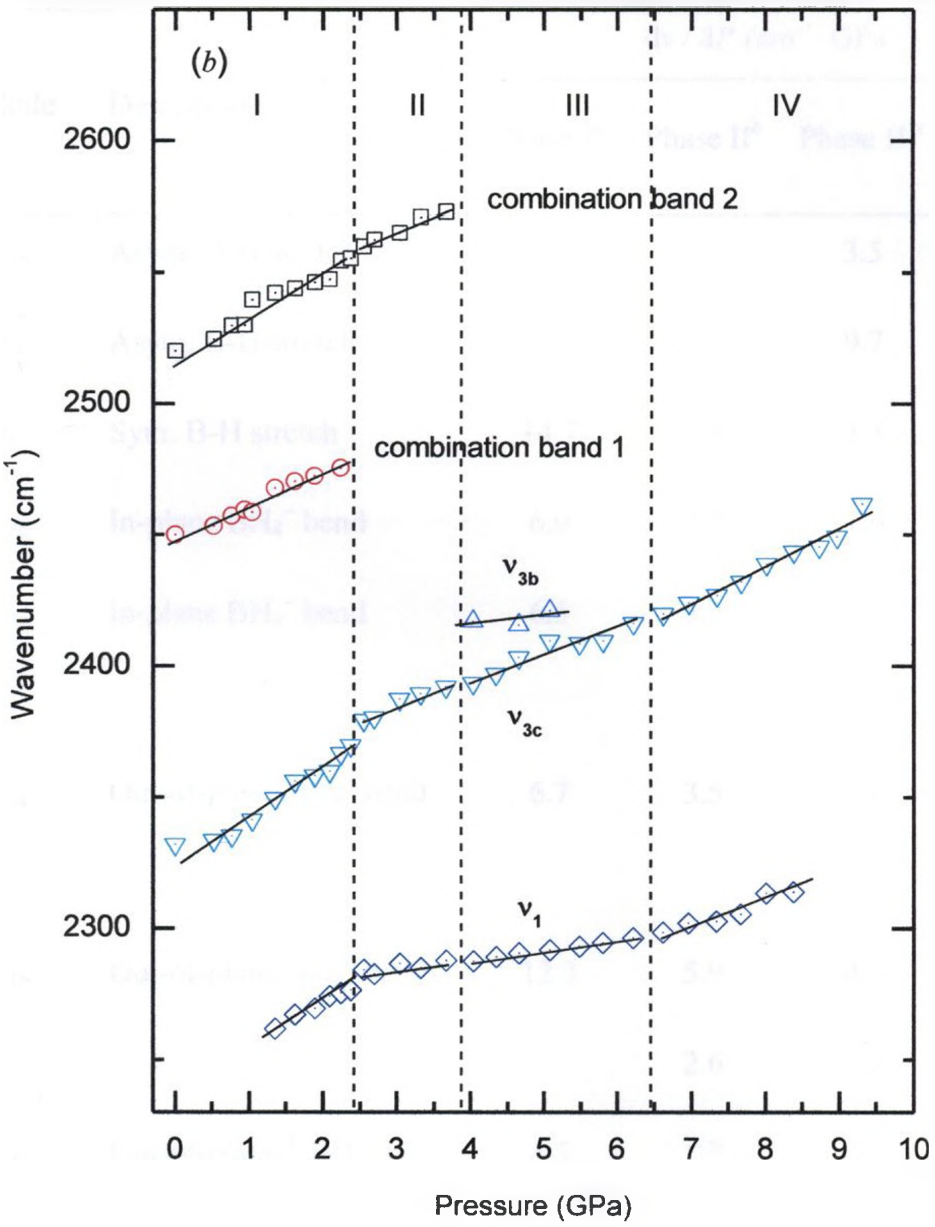

Fig. 3.5. Pressure dependences of the IR modes of $Ca(BH_4)_2$ during compression for (*a*) BH_4^- deformation modes, (*b*) B-H stretching modes and combination modes. Different symbols denote IR modes with different origins. The solid lines crossing the symbols are based on linear fit. The vertical dashed lines indicate one of the proposed phase boundaries.

Table 3.2. Pressure coefficients of selected IR bands of $Ca(BH_4)_2$ on compression

Mode	Description	dv/dP ($cm^{-1} \cdot GPa^{-1}$)			
		Phase I[a]	Phase II[b]	Phase III[c]	Phase IV[d]
v_{3b}	Asym. B-H stretch			3.5	
v_{3c}	Asym. B-H stretch	20.1	15.6	9.7	14.4
v_1	Sym. B-H stretch	14.7	6.4	3.4	9.3
v_{2b}	In-plane BH_4^- bend	6.0	3.2	1.6	7.1
v_{2a}	In-plane BH_4^- bend	6.5	5.2		
v_7					8.0
v_{4a}	Out-of-plane BH_4^- bend	6.7	3.5	3.0	7.5
v_6					7.2
v_{4b}	Out-of-plane BH_4^- bend	12.3	5.9	4.4	7.1
v_5			2.6	2.2	1.9
v_{4c}	Out-of-plane $^{11}BH_4^-$ bend	6.5	5.7	4.7	6.4
v_8					2.8

[a] 1 atm – 2.4 GPa.

[b] 2.4 GPa – 3.7 GPa.

[c] 3.7 GPa – 6.6 GPa.

[d] > 6.6 GPa.

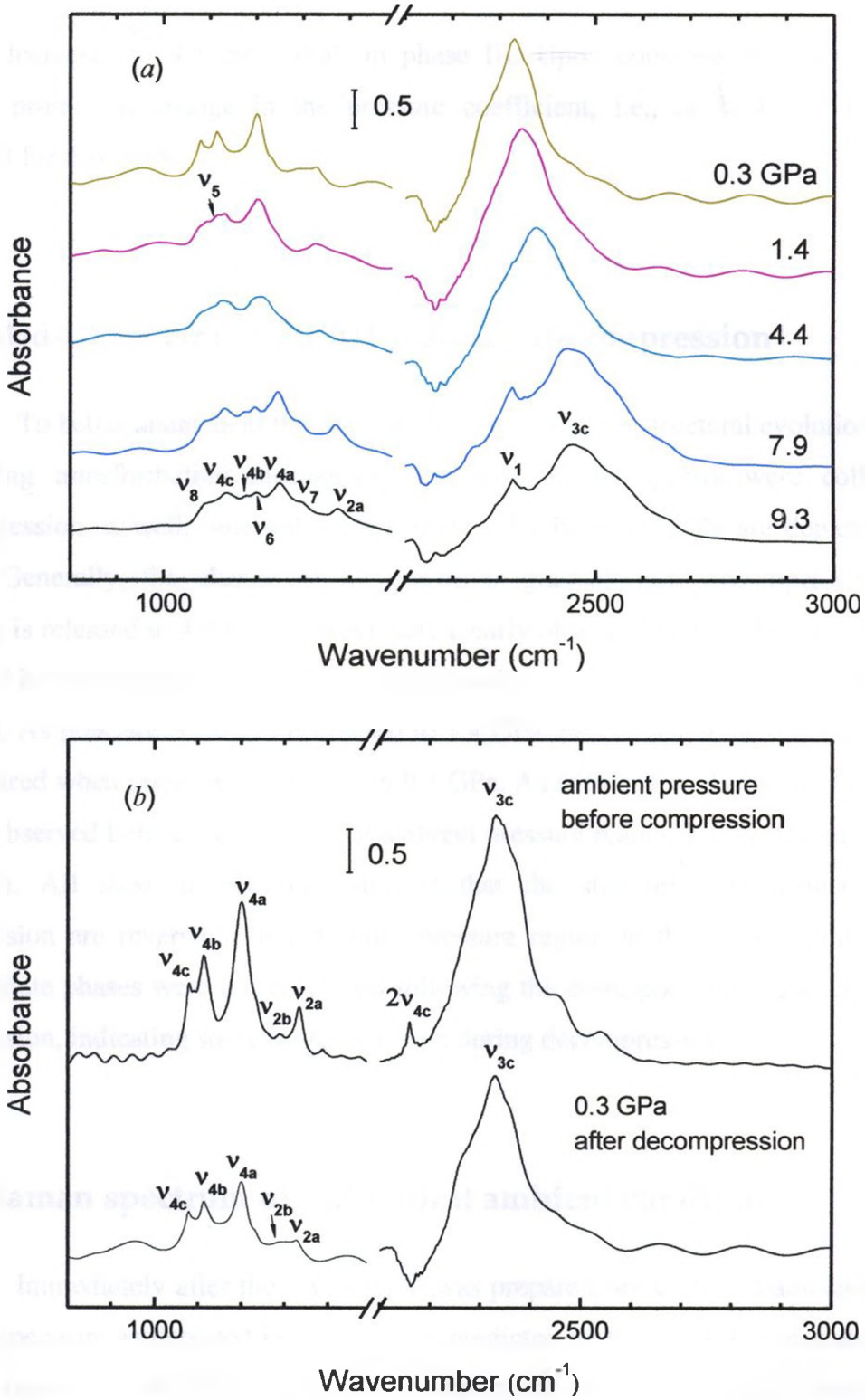

Fig. 3.6. (*a*) Mid-IR spectra of α-$Ca(BH_4)_2$ at room temperature and selected pressures on decompression in the region of 800 - 3000 cm^{-1}. (*b*) Comparison of IR spectrum at ambient pressure before compression and 0.3 GPa after decompression.

further decreases to 9.7 $cm^{-1}\cdot GPa^{-1}$ in phase III. Upon compression above 6.6 GPa, another prominent change in the pressure coefficient, i.e., to 14.4 $cm^{-1}\cdot GPa^{-1}$, was observed for this mode.

3.3.4 Mid-IR spectra of $Ca(BH_4)_2$ during decompression

To better understand the pressure-induced effect on structural evolutions and the underlying transformation mechanism of $Ca(BH_4)_2$, IR spectra were collected on decompression as well. Selected spectra from 9.3 GPa to 0.3 GPa are depicted in Fig. 3.6(*a*). Generally, the change of IR spectra is gradual upon decompression. When pressure is released to 4.4 GPa, a previously clearly observed band v_1 lost its intensity as obscured by the strong v_{3c} band. Meanwhile, bands v_6, v_7 and v_8 are no longer observed at 4.4 GPa. As pressure is further decreased to 1.4 GPa, band v_5 emerged, but subsequently disappeared when pressure is released to 0.3 GPa. As seen in Fig. 3.6(*b*), all fundamental modes observed before compression at ambient pressure reappear after decompression to 0.3 GPa. All these observations suggest that the structural transformations upon compression are reversible in the entire pressure region in this study, although some intermediate phases were not recovered following the corresponding sequence as during compression, indicating some hysteresis exist during decompression.

3.3.5 Raman spectrum of $Ca(BH_4)_2$ at ambient condition

Immediately after the α-$Ca(BH_4)_2$ was prepared, we collected ambient-pressure Raman spectrum as depicted in Fig. 3.7. As predicted by the normal modes analysis, all internal modes of α-$Ca(BH_4)_2$ are both IR and Raman active. Although Fichtner et al.[18] and Miwa et al.[5] reported Raman spectrum of α-$Ca(BH_4)_2$ at ambient conditions, detailed experimental Raman frequencies were not reported. Therefore, the assignment of Raman modes can be done by comparing with the IR analysis[19] and theoretical calculations.[5] The

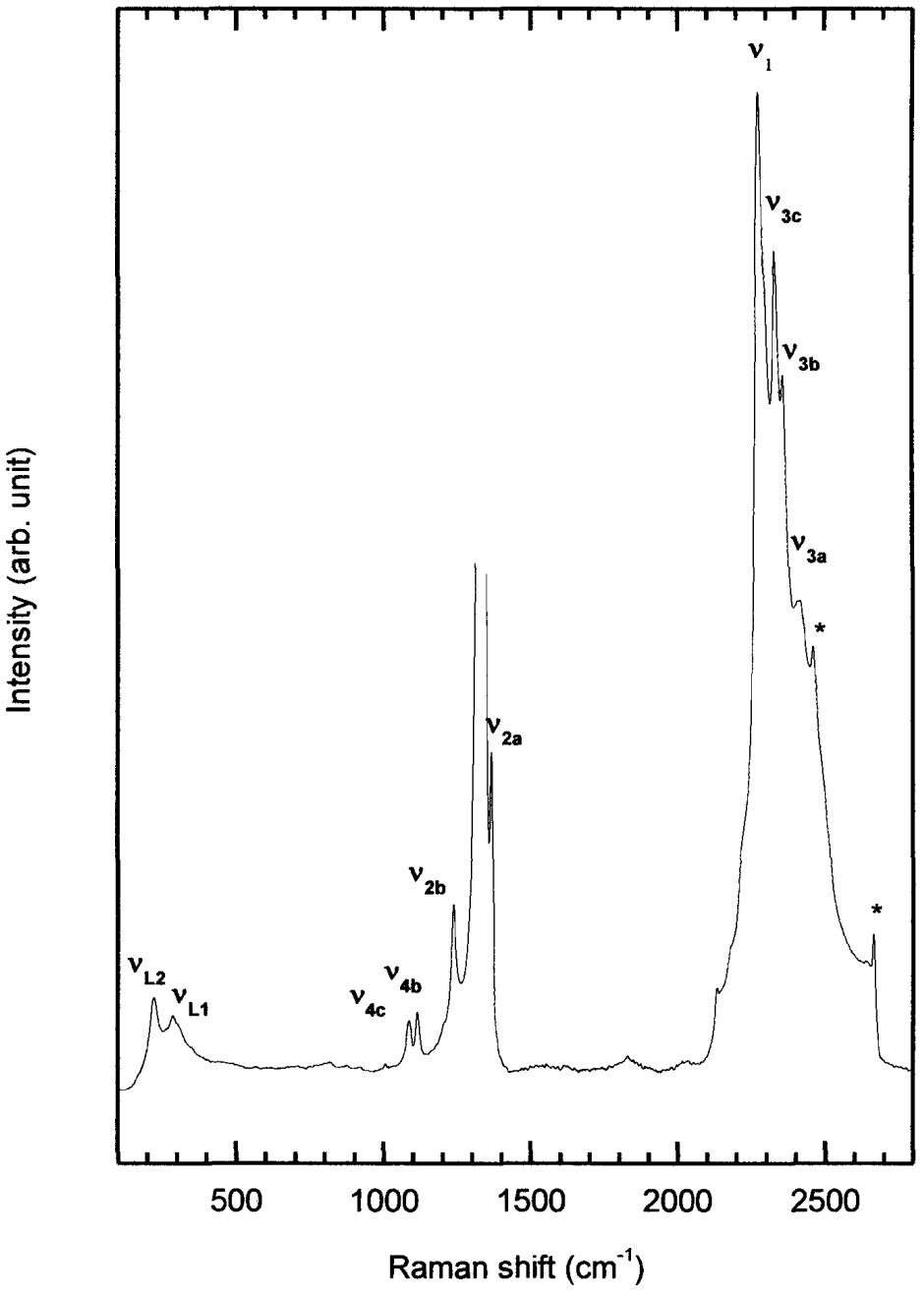

Fig. 3.7. Raman spectrum of α-$Ca(BH_4)_2$ at ambient condition in the region of 100 - 2800 cm^{-1}. The second order Raman bands from the diamonds are labeled with asterisks.

Table 3.3. Raman shifts for α-$Ca(BH_4)_2$ and the assignment at ambient pressure

Raman (cm^{-1})		IR (cm^{-1})			Assignment	
This work[a]	Ref. 5[a]	This work[b]	Ref. 19[c]	Ref. 19[d]		
2412	2373/2382	2415	2415	2426	v_{3a}	Asym. B-H stretch
2356	2368/2376	2356	2356	2358	v_{3b}	Asym. B-H stretch
2330	2311/2319	2332	2332	2332	v_{3c}	Asym. B-H stretch
2274	2283/2285	2273[e]	2273	2271	v_1	Sym. B-H stretch
1367	1265/1269	1327	1327	1330	v_{2a}	In-plane BH_4^- bend
1237	1189/1191	1241	1241	1244	v_{2b}	In-plane BH_4^- bend
		1204	1204	1212	v_{4a}	Out-of-plane BH_4^- bend
1114	1164/1166	1117	1117	1119	v_{4b}	Out-of-plane BH_4^- bend
1086	1025/1032	1089	1089	1093	v_{4c}	Out-of-plane BH_4^- bend
286	291				v_{L1}	Lattice mode
222	221				v_{L2}	Lattice mode

[a] Theoretical calculation.

[b] Measured at room temperature.

[c] Measured at 300 K.

[d] Measured at 80 K.

[e] Measured at 1.4 GPa.

assignments are tabulated in Table 3.3. In general, our observed Raman frequencies are consistent with both previous and our own IR data, but deviate from the theoretical predications by some extent. This discrepancy is likely associated with the difficulty in the alignment of the unresolved splitting in present study with the theoretical predications.

In contrast to the IR measurements, where only one B-H stretching band was observed at ambient pressure, the asymmetric B-H stretching modes were well resolved in to a triplet (v_{3c}, v_{3b}, v_{3a}) near 2350 cm^{-1} in the Raman spectrum. In addition, the symmetric B-H stretching mode v_1, which could not be observed in ambient-pressure IR spectrum, appears as the most intense peak at 2274 cm^{-1} in Raman spectrum. In the region of 1000 - 1450 cm^{-1}, four BH_4^- deformation modes (v_{4c}, v_{4b}, v_{2b} and v_{2a}) were seen at similar frequencies as in IR measurements. In addition to the internal vibrational modes, two more peaks were observed at 286 and 222 cm^{-1}, which can be assigned as lattice modes. The lattice feature is consistent with that reported by Fichtner et al. [18]

3.3.6 Raman spectra of the internal modes of $Ca(BH_4)_2$ during compression

Similar to the IR measurements, Raman spectra of $Ca(BH_4)_2$ were collected upon compression. Fig. 3.8 shows selected Raman spectra of the internal modes of $Ca(BH_4)_2$ on compression up to 10.4 GPa. Based on its molecular nature again, the Raman spectra are characterized in two regions, i.e., the B-H stretching mode region, and the BH_4^- deformation modes region.

As shown in Fig. 3.8(*a*), the symmetric stretching mode v_1 at 2274 cm^{-1} is the dominant peak at ambient pressure. However, upon compression it loses intensity rapidly and becomes a weak shoulder of v_{3c}. In contrast, the v_{3c} mode, which is a B-H asymmetric stretching mode at 2330 cm^{-1}, evolves as the most intense peak from 2.3 GPa. Similar to the weakening of mode v_1, the intensity of another B-H asymmetric stretching

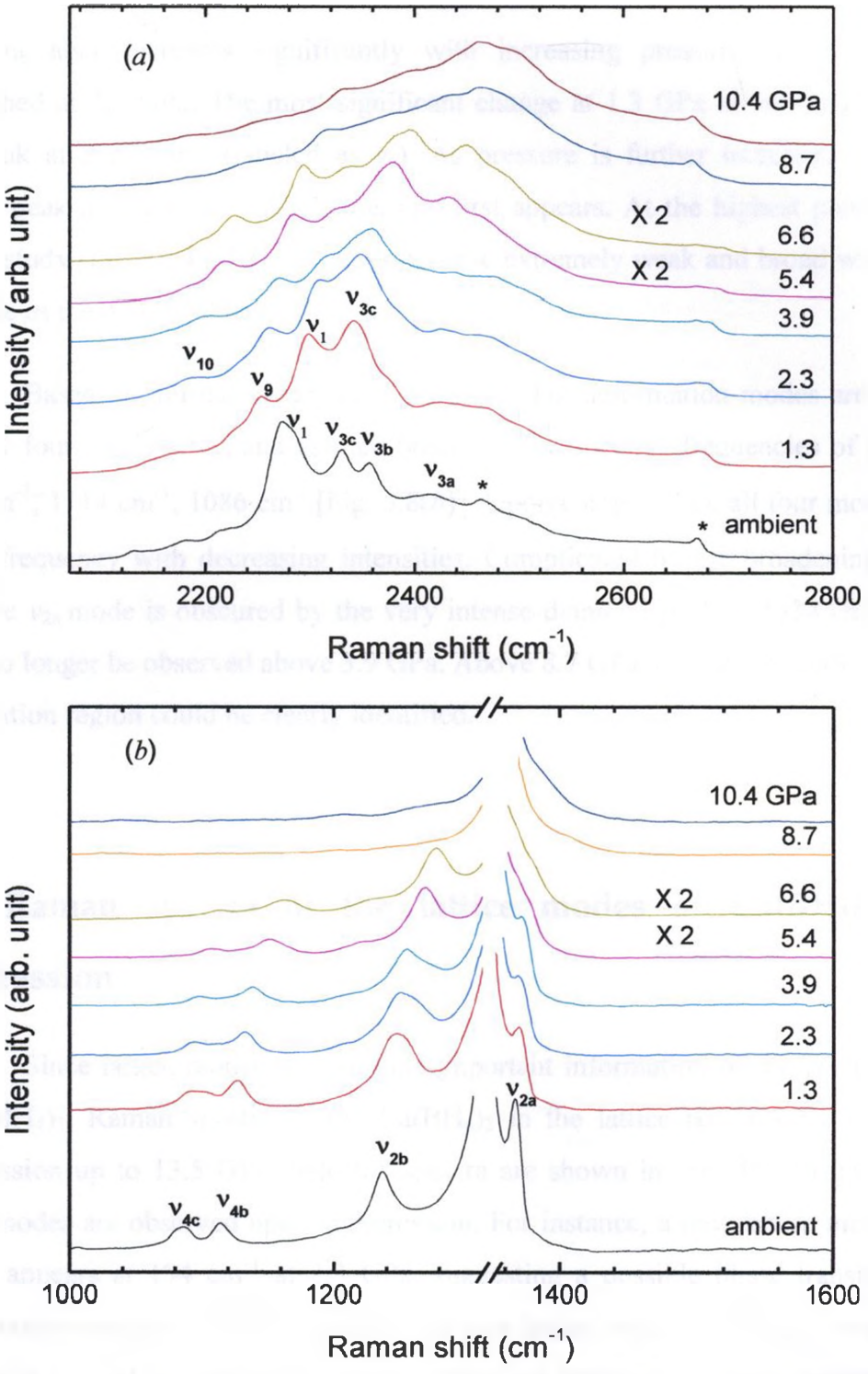

Fig. 3.8. Raman spectra of $Ca(BH_4)_2$ at room temperature and selected pressures on compression (*a*) in the B-H stretching region of 2070 to 2800 cm^{-1} and (*b*) in the BH_4^- deformation region of 1000 to 1600 cm^{-1}. Diamonds peaks are labeled with asterisks. Intensities of Raman spectra at 5.4 and 6.6 GPa are scaled by a factor of 2 for clarity.

mode v_{3b} also decreases significantly with increasing pressure and is completely diminished at 2.3 GPa. The most significant change at 1.3 GPa is the observation of a new peak at 2253 cm^{-1} (labeled as v_9). As pressure is further increased to 2.3 GPa, another peak at 2189 cm^{-1} (labeled as v_{10}) first appears. At the highest pressure of the current study (i.e., 10.4 GPa), all peaks become extremely weak and broad with only the v_{3a} mode as the dominant band.

Based on normal modes analysis, five BH_4^- deformation modes are predicted, but only four (v_{2a}, v_{2b}, v_{4b} and v_{4c}) are observed at respective frequencies of 1367 cm^{-1}, 1237 cm^{-1}, 1114 cm^{-1}, 1086 cm^{-1} [Fig. 3.8(*b*)]. Upon compression, all four modes shift to higher frequency with decreasing intensities. Complicated by the broadening and blue shift, the v_{2a} mode is obscured by the very intense diamond peak at 1334 cm^{-1} and thus could no longer be observed above 3.9 GPa. Above 8.7 GPa, no Raman modes in the B-H deformation region could be clearly identified.

3.3.7 Raman spectra of the lattice modes of $Ca(BH_4)_2$ during compression

Since lattice modes will provide important information of the crystal structure of $Ca(BH_4)_2$, Raman spectra of the $Ca(BH_4)_2$ in the lattice region were collected on compression up to 13.5 GPa. Selected spectra are shown in Fig. 3.9. In general, more lattice modes are observed upon compression. For instance, a new lattice mode (labeled as v_{L3}) appears at 194 cm^{-1} at 2.3 GPa, suggesting a possible phase transition. Upon further compression to 3.9 GPa, another two new lattice modes at 296 cm^{-1} and 320 cm^{-1} (labeled as v_{L4} and v_{L5}, respectively) were observed, indicating another transformation of the crystal structure of $Ca(BH_4)_2$. As lattice modes shift to higher frequency, v_{L4} get sharper and eventually become the most intense lattice mode at 6.6 GPa. Concurrently, a new lattice mode at 296 cm^{-1} (labeled as v_{L6}) was also observed.

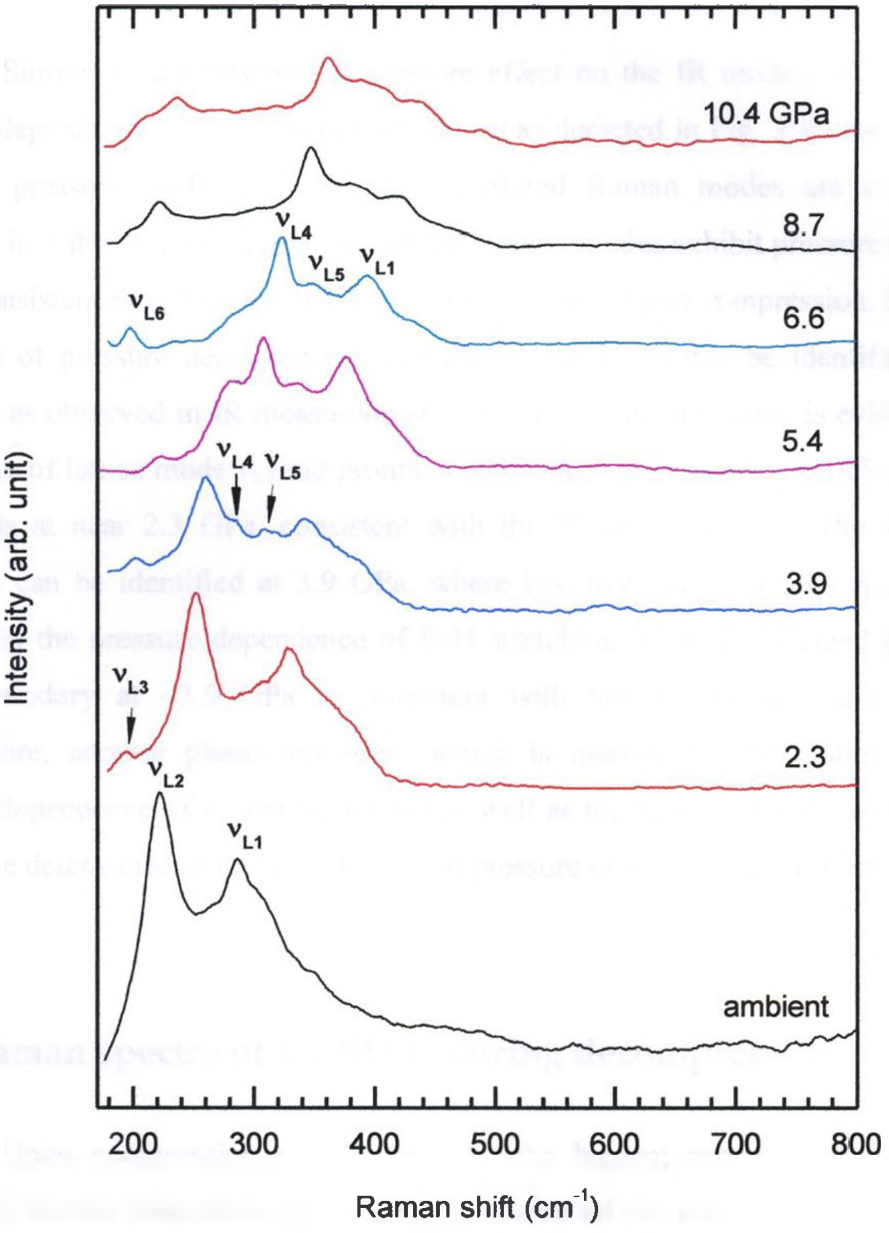

Fig. 3.9. Raman spectra of $Ca(BH_4)_2$ in the lattice region of 170 to 800cm^{-1} at room temperature and selected pressures on compression. Different symbols denote IR modes with different origins. The solid lines crossing the symbols are based on linear fit. The vertical dashed lines indicate one of the proposed phase boundaries.

3.3.8 Pressure effects on Raman modes of $Ca(BH_4)_2$

Similar to the analysis of pressure effect on the IR modes, we examined the pressure dependence of selected Raman modes as depicted in Fig. 3.10 and Fig. 3.11. In addition, pressure coefficients for the monitored Raman modes are calculated and tabulated in Table 3.4. In general, almost all Raman modes exhibit pressure-induced blue shifts, consistent with that the bonds become stiffened upon compression. Based on the evolution of pressure dependence, three phase transitions can be identified at similar pressures as observed in IR measurements. The first phase transition is evidenced by the emergence of lattice mode v_{L3} and pronounced changes in pressure coefficients of v_{L1} and v_{L2} modes at near 2.3 GPa, consistent with the IR measurements. The second phase transition can be identified at 3.9 GPa, where two new lattice modes v_{L4} and v_{L5} first appear and the pressure dependence of B-H stretching mode v_{3a} changed abruptly. The phase boundary at ~3.9 GPa is consistent with that determined in the IR study. Furthermore, another phase transition, which is marked by the distinct changes of pressure dependence of v_1 and v_{3a} modes as well as the appearance of new lattice mode v_{L6}, can be determined at the same transition pressure of 6.6 GPa as in IR measurements.

3.3.9 Raman spectra of $Ca(BH_4)_2$ during decompression

Upon compression of $Ca(BH_4)_2$ to the highest pressure of 10.4 GPa, we conducted Raman measurements on decompression all the way down to a near ambient pressure. As shown in Fig. 3.12(*b*), most Raman modes reappear upon decompression at 0.1GPa, giving a similar Raman profile to the one at ambient pressure before compression. Therefore the pressure-induced phase transformations of $Ca(BH_4)_2$ are reversible, consistent with the analysis based on our IR measurements, although some intermediate phases could not be clearly identified by Raman measurements due to the interference of the strong second order Raman band of diamond in the region of 2100 to 2700 cm^{-1} [Fig. 3.12(*a*)].

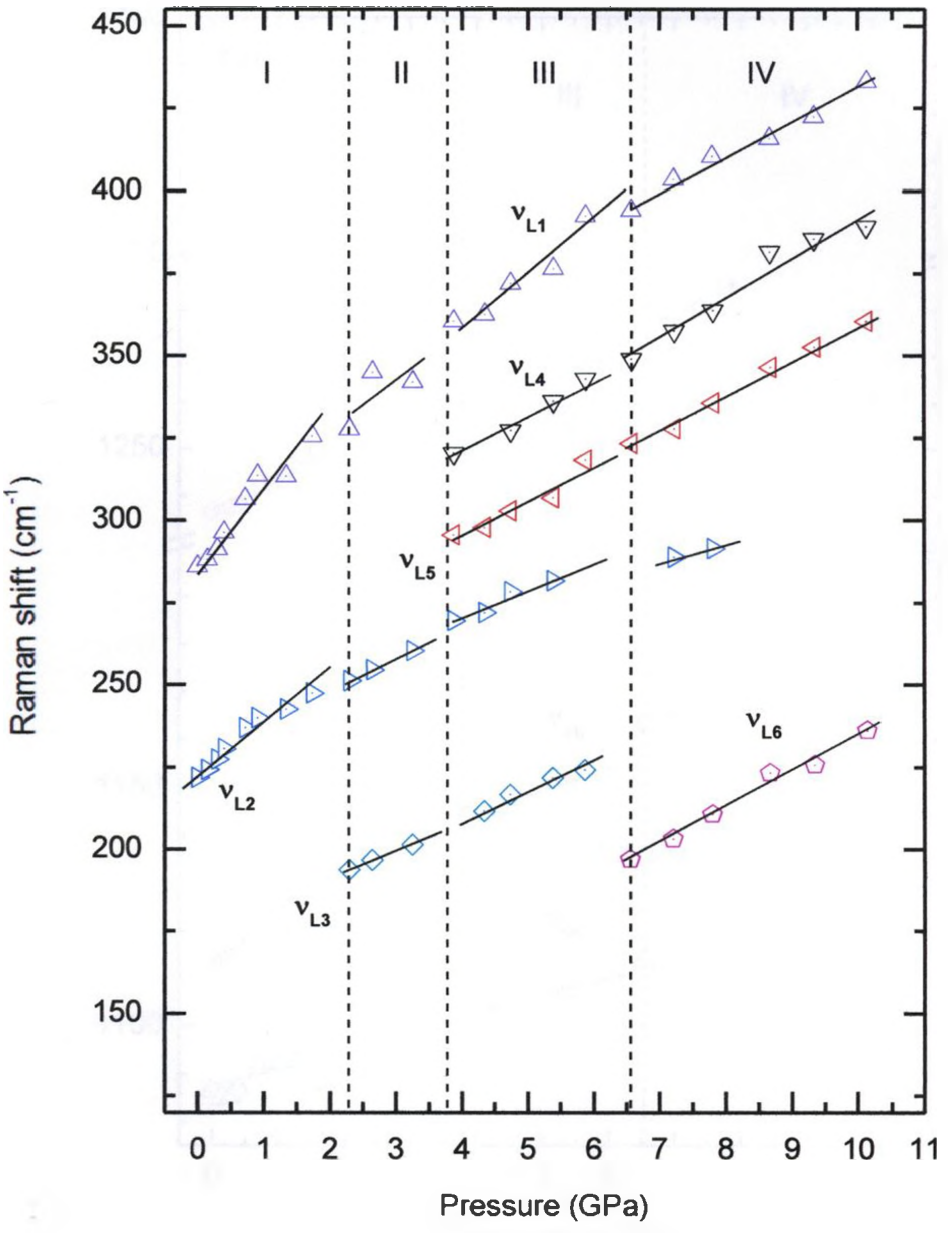

Fig. 3.10. Pressure dependences of the Raman lattice modes of $Ca(BH_4)_2$ during compression. Different symbols denote IR modes with different origins. The solid lines crossing the symbols are based on linear fit. The vertical dashed lines indicate one of the proposed phase boundaries.

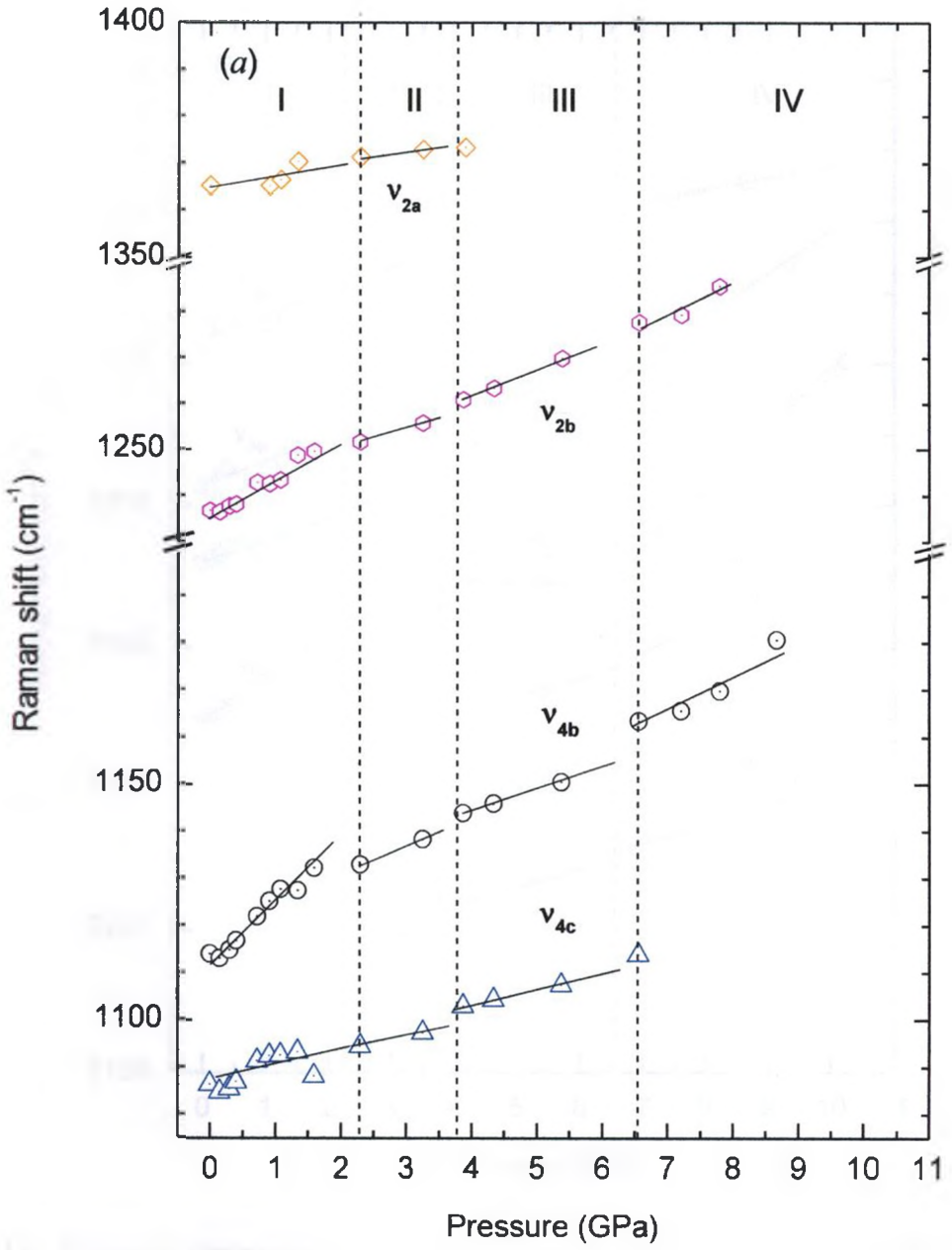
(a)
I
II
III
IV
ν_{2a}
ν_{2b}
ν_{4b}
ν_{4c}
Raman shift (cm^{-1})
Pressure (GPa)
1400
1350
1250
1150
1100
0
1
2
3
4
5
6
7
8
9
10
11

Fig. 3.11.

Continued

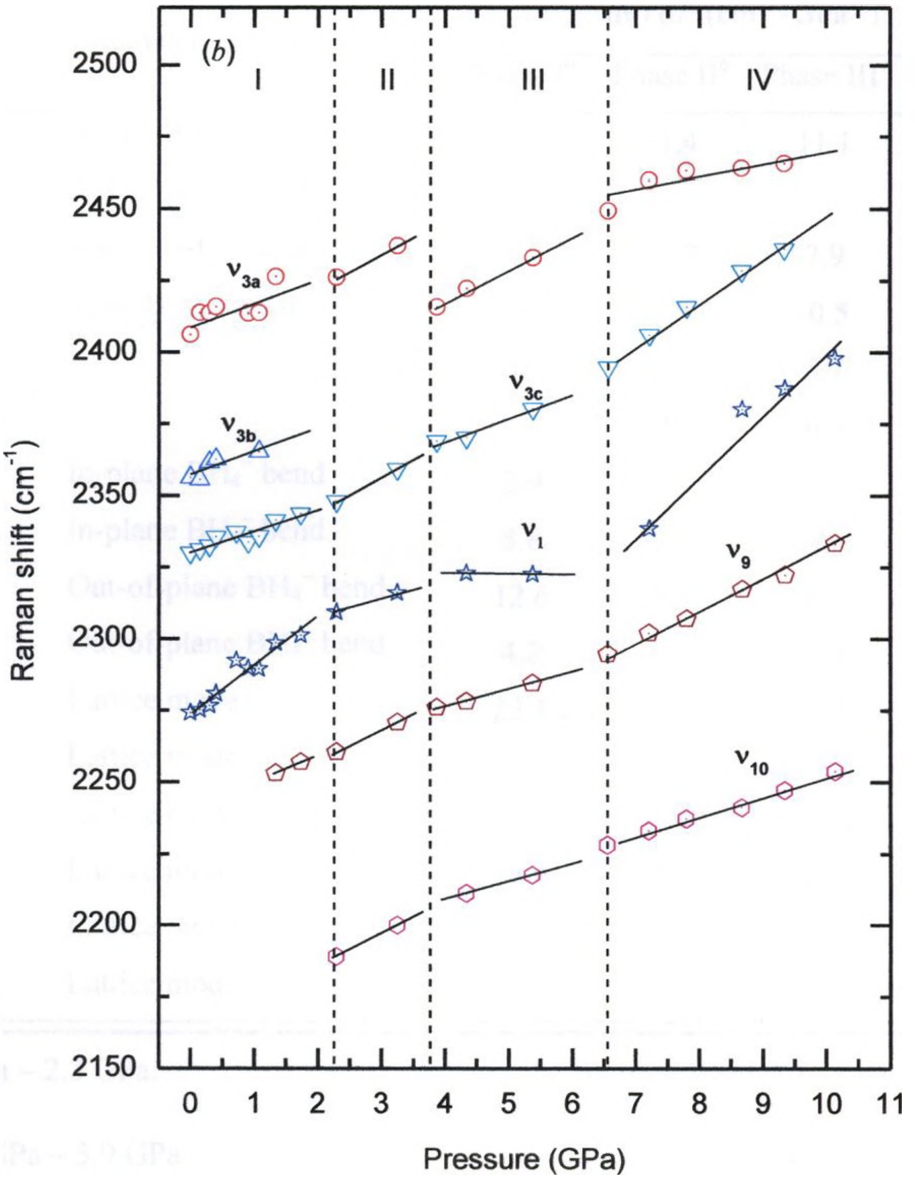

Fig. 3.11. Pressure dependences of the Raman internal modes of $Ca(BH_4)_2$ during compression for (*a*) BH_4^- deformation modes, (*b*) B-H stretching modes. Different symbols denote IR modes with different origins. The solid lines crossing the symbols are based on linear fit. The vertical dashed lines indicate one of the proposed phase boundaries.

Table 3.4. Pressure coefficients of selected Raman modes of $Ca(BH_4)_2$ on compression

	Raman mode	dv/dP ($cm^{-1} \cdot GPa^{-1}$)			
		Phase I[a]	Phase II[b]	Phase III[c]	Phase IV[d]
v_{3a}	Asym. B-H stretch	8.7	11.4	11.1	5.1
v_{3b}	Asym. B-H stretch	8.9			
v_{3c}	Asym. B-H stretch	7.2	11.7	7.9	14.9
v_1	Sym. B-H stretch	16.9	7.0	-0.5	20.4
v_9		10	10.6	5.7	10.5
v_{10}			11.5	6.3	6.9
v_{2a}	In-plane BH_4^- bend	2.9	1.6		
v_{2b}	In-plane BH_4^- bend	8.8	4.3	6.0	6.4
v_{4b}	Out-of-plane BH_4^- bend	12.6	5.6	8.2	
v_{4c}	Out-of-plane BH_4^- bend	4.2	3.0	3.0	
v_{L1}	Lattice mode	23.1	16.6	13.9	9.6
v_{L4}	Lattice mode			11.0	11.5
v_{L5}	Lattice mode			11.0	11.0
v_{L2}	Lattice mode	14.9	9.5	8.5	4.5
v_{L3}	Lattice mode		8.1	9.1	
v_{L6}	Lattice mode				10.9

[a] 1 atm – 2.3 GPa.

[b] 2.3 GPa – 3.9 GPa.

[c] 3.9 GPa – 6.6 GPa.

[d] > 6.6 GPa.

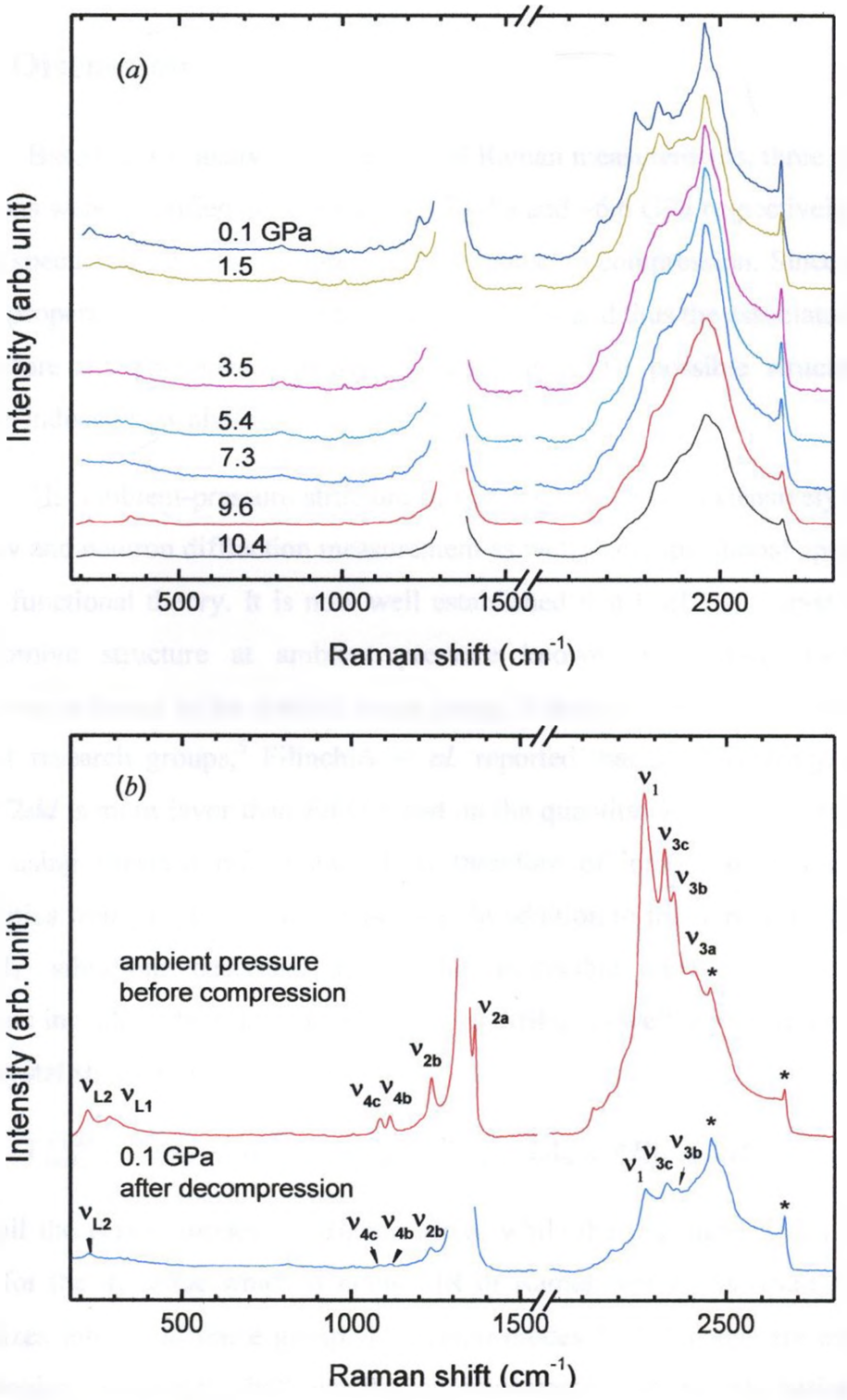

Fig. 3.12. (*a*) Raman spectra of $Ca(BH_4)_2$ at room temperature and selected pressures on decompression in the region of 170 – 2800 cm^{-1}. (*b*) Comparison of Raman spectrum at ambient pressure before compression and at 0.1 GPa after decompression. Diamond peaks are labeled with asterisks.

3.3.10 Discussion

Based on the analysis of our IR and Raman measurements, three possible phase transitions were identified at ~2.3 GPa, ~3.7 GPa and ~6.6 GPa respectively based on the distinct spectroscopic features observed in response to compression. Since the hydrogen storage properties critically depends on the structures and thus the associated stabilities, it is therefore of fundamental interest to understand the possible structures of these pressure-induced new phases.

The ambient-pressure structure of $Ca(BH_4)_2$ has been extensively characterized by X-ray and neutron diffraction measurement as well as computational approaches using density functional theory. It is now well established that $Ca(BH_4)_2$ crystallizes into an orthorhombic structure at ambient pressure known as α-phase. However, some controversy arises as to the detailed space group. Although space group *Fddd* is proposed by most research groups,[5] Filinchuk *et al.* reported that a noncentrosymmetric space group *F*2*dd* is more favor than *Fddd* based on the quantitative analysis of the diffraction pattern using Rietveld refinement.[1] It is therefore of interest to examine these two possibilities from spectroscopic perspective. In addition to the normal mode analysis for the BH_4^- vibrations described above, the irreducible representation of the lattice vibrations including the translations of Ca^{2+} and BH_4^- as well as the BH_4 rotations in the *Fddd* crystal structure is:

$$\Gamma_{lattice}^{Fddd} = 2A_g + 5B_{1g} + 3B_{2g} + 5B_{3g} + 2A_u + 4B_{1u} + 2B_{2u} + 4B_{3u} \qquad (3.2)$$

where all the gerade modes are Raman active while the ungerade modes are IR active, except for the A_u mode which is neither IR or Raman active. As result, if α-$Ca(BH_4)_2$ crystallizes into *Fddd* space group, 15 Raman modes 12 IR modes are expected in the lattice region. Apparently, both our Raman measurement where only lattice modes were observed and that by Fichtner *et al.*,[18] who observed a total of 4 lattice modes at room temperatures suggest that only a subset of the lattice modes are detectable if the assumed crystal structure is correct.

In contrast, assuming *F*2*dd* (C_{2v}^{19}) as the space group for α-$Ca(BH_4)_2$ and by using the crystal data reported by Filinchuk (i.e., Ca^{2+} on C_2 site and BH_4^- on general C_1 site), the irreducible representations for the BH_4^- internal vibrations and the lattice vibrations are:

$$\Gamma_{BH_4^- vib}^{F2dd} = (4A_1 + A_2 + 2B_1 + 2B_2)\times 2 \tag{3.3}$$

$$\Gamma_{lattice}^{F2dd} = 6A_1 + 7A_2 + 7B_1 + 7B_2 \tag{3.4}$$

where all species are Raman active and species A_1, B_1 and B_2 are IR active. As a result, a total of 18 internal and 27 lattice modes are Raman active while 16 internal and 20 lattice modes are IR active. Similarly, since the correlation field splitting is unlikely to be observed with current spectral resolution and/or very small intrinsic split magnitude, the number of observable internal modes would be halved, i.e, 9 Raman active modes and 8 IR active modes.

In addition, based to the nature of vibrations, two distinct spectral regions, i.e., bending (1000 – 1400 cm^{-1}) and stretching (2200 – 2500 cm^{-1}) can be separated from the total irreducible representations. In Table 3.5 we summarize the Raman and IR active modes in three spectral regions, i.e., bending, stretching and lattice regions, under different space groups for comparison. As can be seen, the Raman measurement in the lattice region does not allow the unambiguous identification of the space group. In addition, we observed 1 – 2 IR active modes and 4 Raman active modes in the stretching region, consistent with both space groups. However, we observed 5 IR active modes and 4 Raman active modes in the bending region, consistent with the predictions assuming Fddd, while only 4 IR modes are expected under the *F*2*dd* space group. Therefore, our measurements suggest that the crystal structure of $Ca(BH_4)_2$ in high-pressure (from ambient pressure to 2.3 GPa) phase I likely has a space group *Fddd*. To further confirm this centrosymmetry space group, measurement in the far-IR region would be helpful. In addition, we note that in Filinchuk's study, the α-phase $Ca(BH_4)_2$ structure was obtained and analyzed at 91 K. Therefore, it's likely the difference in the proposed space groups is

associated with the temperature factor and thus it would be interesting to collect the Raman and IR spectra at low temperatures.

Table 3.5. Observed number of IR and Raman active modes for α-$Ca(BH_4)_2$ in comparison with predictions using *Fddd* and *F*2*dd* space group.[a]

Spectral region	Observed		Predicted			
			Fddd		*F2dd*	
	IR	Raman	IR	Raman	IR	Raman
Lattice	—	2	12	15	20	27
Bending	5	4	5 (10)	5 (10)	4 (8)	5 (10)
Stretching	1 – 2	4	4 (8)	4 (8)	4 (8)	4 (8)

[a] Number in the parenthesis for the internal modes refers to that with correlation field splitting.

The crystal structure of another polymorph of $Ca(BH_4)_2$, produced at elevated temperatures, i.e., the β-phase, has also been studied by both experimental and theoretical approaches.[1,16] Although the space group for this phase has been primarily been determined as $P4_2/m$,[21] Filinchuk *et al.*[1] and Majzoub *et al.*[16] raised similar controversy as that for α-phase because space group $P\bar{4}$ is more favored using Rietveld analysis. To our understanding, other than the extensive diffraction studies on α- and β-phases at ambient pressures, there has been no high-pressure X-ray or neutron data for $Ca(BH_4)_2$. However, three new high-pressure phases were identified in our spectroscopic study, making β-phase structure a possible candidate for one of these high-pressure phases. This is particularly because higher pressure phases are typically characterized by smaller unit

cell volume and thus higher density, while β-phase $Ca(BH_4)_2$ exhibits a density that is ~3 % higher than that for α-phase. In addition, using first-principles calculations, Majzoub *et al.*[16] examined the enthalpy as a function of the unit cell volume for several possible structures of $Ca(BH_4)_2$. It was predicted that above 5.3 GPa, the preferred structure for $Ca(BH_4)_2$ has an orthorhombic structure with space group $P\bar{4}$, same as one of the proposed structures of β-$Ca(BH_4)_2$. In addition, the predicted transition pressure is in alignment with the pressure region of 3.3 – 6.7 GPa for which we claimed phase III. Therefore, it would be of fundamental interest to examine the spectroscopic consistency in the context of these possible proposed space groups.

For space group $P4_2/m$ (Z = 2), Ca^{2+} occupies C_{2h} site whereas BH_4^- takes C_s site. Therefore, the irreducible representation for the internal modes and lattice modes are:

$$\Gamma_{BH_4^- vib}^{P4_2/m} = 3A_g + 3B_g + 2E_g + 1A_u + 1B_u + 3E_u \tag{3.5}$$

$$\Gamma_{lattice}^{P4_2/m} = 3A_g + 3B_g + 4E_g + 3A_u + 4B_u + 3E_u \tag{3.6}$$

where all gerade modes are Raman active while the ungerade modes, except for the B_u modes, are IR active. Therefore, a total of 8 Raman modes and 4 IR modes are expected for the BH_4^- vibrations and 10 Raman modes and 6 IR modes for the lattice vibrations. In contrast, for space group $P\bar{4}$ (Z = 2), where Ca^{2+} and BH_4^- occupy C_2 and C_1 site respectively, the irreducible representation for the internal and lattice modes are:

$$\Gamma_{BH_4^- vib}^{P\bar{4}} = (2A + 3B + 2E) \times 2 \tag{3.7}$$

$$\Gamma_{lattice}^{P\bar{4}} = 7A + 6B + 7E \tag{3.8}$$

where all species are Raman active and species B and E are IR active. Therefore, a total of 14 (7 without correlation field splitting) internal and 20 lattice modes are Raman active while 10 (5 without correlation field splitting) internal and 13 lattice modes are IR active. These analyses are summarized in Table 3.6. Apparently, the observation of a total of 8 Raman and 8 IR internal modes represent a closer match to those (i.e., 14 and 10

respectively) predicted by space group $P\bar{4}$. In contrast, the observed number of active Raman and IR internal modes does not match, in most cases exceeds the predicted values in the individual bending and stretching regions under space group $P4_2/m$, suggesting that the other choice, i.e., $P\bar{4}$ is more likely the structure for high-pressure phase III from the spectroscopic perspective, if $Ca(BH_4)_2$ is to form a denser tetragonal phase. We further note that if the assumption of space group $P\bar{4}$ is correct, correlation field splitting is important to account for the total number of Raman and IR active modes, consistent with those intermolecular interactions are markedly enhanced by compression.

Table 3.6. Observed number of IR and Raman active modes for β-$Ca(BH_4)_2$ in comparison with predictions using $P4_2/m$ and $P\bar{4}$ space group.[a]

Spectral region	Observed		Predicted			
			$P4_2/m$		$P\bar{4}$	
	IR	Raman	IR	Raman	IR	Raman
Lattice	—	5	6	10	13	20
Bending	5	3	3	2	3 (6)	4 (8)
Stretching	3	5	1	6	2 (4)	3 (6)

[a] Number in the parenthesis for the internal modes refers to that with correlation field splitting.

The remaining questions concern the possible structures for phase II and IV. The phase between 2.3 and 3.7 GPa (labeled as Phase II) could be regarded as an intermediate phase for the transition Phase I to Phase III. This is evidenced by that fact that some modes (Raman ν_{2a}, ν_{3a}, ν_{L4}, ν_{L5} modes, IR ν_{2b} and ν_5 modes) which appear in Phase I or Phase III but not in both, coexist in Phase II. The Raman and IR spectra above

6.6 GPa (Phase IV) are characterized by significant band broadening and intensity reduction. At the highest pressure studied in this work (i.e. 10.4 GPa for Raman and 9.3 GPa for IR) all Raman modes and IR modes become extremely board and weak leaving significantly fewer distinguishable bands than before compression. All these observations suggest the structure of $Ca(BH_4)_2$ is becoming less ordered and may ultimately turn into an amorphous phase with further compression. Apparently, to understand the detailed structures of Phase II and IV, in situ X-ray or neutron diffraction measurements and are required with the aid of theoretical investigations.

Finally, based on the almost identical spectroscopic details in both Raman and IR spectra before compression and after decompression, we established that all the pressure-induced phase transitions are reversible, indicating that $Ca(BH_4)_2$ is chemically and structurally stable in a broad pressure region. This study thus provide a basis to investigate the possibility of forming new complex between $Ca(BH_4)_2$ and H_2 for hydrogen storage applications. Lin *et al.* has recently reported the observation of a chemical complex between $NH_3 \cdot BH_3$ and hydrogen under high pressures.[22] It would be of great interest to further explore the interactions between $Ca(BH_4)_2$ and H_2 at high pressures as well.

3.4 Conclusions

The effect of pressure on the structure of $Ca(BH_4)_2$ were investigated by Raman and IR spectroscopy up to 10 GPa. Three phase transitions upon compression were observed at near 2.3, 3.7 and 6.6 GP, as evidenced by changes in peak profiles and the pressure dependence of characteristic Raman and IR modes over various pressure ranges. Spectroscopic measurements on decompression suggest these pressure-induced transitions are reversible with the chemical structure of $Ca(BH_4)_2$ intact, indicating that $Ca(BH_4)_2$ is stable up to the pressure achieved in this study. Spectral analysis based on our combined Raman and IR measurement suggest the high-pressure phase I from

ambient pressure to ~2.3 GPa maintains the known α-phase structure with space group *Fddd*. Suggested by first-principles calculations, $Ca(BH_4)_2$ may exist as a denser tetragonal phase at high pressures, consistent with our Raman and IR measurements. The predicted transition pressure is within Phase III region of $Ca(BH_4)_2$, i.e., 3.7 – 6.6 GPa in this study. Detailed factor group analysis suggests that in the structure of Phase III $Ca(BH_4)_2$ is more likely $P\bar{4}$ rather than $P4_2/m$. The structures of Phase II and IV require further experimental and theoretical investigations.

3.5 Acknowledgements

This work is supported by a Discovery Grant and a Research Tools and Instruments Grant from the Natural Science and Engineering Research Council of Canada, a Leaders Opportunity Fund from the Canadian Foundation for Innovation and an Early Researcher Award from the Ontario Ministry of Research and Innovation. XS acknowledges the technical support from Dr. S. Ramamurthy and Mr. J. Kabel for the synthesis of Calcium borohydride at Surface Science Western, UWO.

3.6 References

(1) Filinchuk, Y.; Ronnebro, E.; Chandra, D. *Acta. Mater.* **2009**, *57*, 732.

(2) Kim, J. H.; Jin, S. A.; Shim, J. H.; Cho, Y. W. *Scripta Mater.* **2008**, *58*, 481.

(3) Kim, J. H.; Shim, J. H.; Cho, Y. W. *J. Power Sources* **2008**, *181*, 140.

(4) Nakamori, Y.; Li, H. W.; Kikuchi, K.; Aoki, M.; Miwa, K.; Towata, S.; Orimo, S. *J. Alloy Compd.* **2007**, *446*, 296.

(5) Miwa, K.; Aoki, M.; Noritake, T.; Ohba, N.; Nakamori, Y.; Towata, S.; Zuttel, A.; Orimo, S. *Phys. Rev. B* **2006**, *74*.

(6) Chlopek, K.; Frommen, C.; Leon, A.; Zabara, O.; Fichtner, M. *J. Mater. Chem.* **2007**, *17*, 3496.

(7) Makhaev, V. D.; Borisov, A. P.; Antsyshkina, A. S.; Sadikov, G. G. *Russ J. Inorg. Chem+.* **2004**, *49*, 323.

(8) George, L.; Drozd, V.; Saxena, S. K.; Bardaji, E. G.; Fichtner, M. *J. Phys. Chem. C* **2009**, *113*, 486.

(9) Ronnebro, E.; Majzoub, E. H. *J. Phys. Chem. B* **2007**, *111*, 12045.

(10) Kim, J. H.; Jin, S. A.; Shim, J. H.; Cho, Y. W. *J. Alloy Compd.* **2008**, *461*, L20.

(11) Wiberg, E.; Hartwimmer, R. *Z. Naturforsch. Pt. B* **1955**, *10*, 295.

(12) Wiberg, E.; Noth, H.; Hartwimmer, R. *Z. Naturforsch. Pt. B* **1955**, *10*, 292.

(13) Mikheeva, V. I.; Titov, L. V. *Zh. Neorg. Khim+.* **1964**, *9*, 789.

(14) Konoplev, V. N.; Silina, T. A.; Sizareva, A. S. *Koordinats. Khim+.* **1992**, *18*, 508.

(15) Barkhordarian, G.; Jensen, T. R.; Doppiu, S.; Bosenberg, U.; Borgschulte, A.; Gremaud, R.; Cerenius, Y.; Dornheim, M.; Klassen, T.; Bormann, R. *J. Phys. Chem. C* **2008**, *112*, 2743.

(16) Majzoub, E. H.; Ronnebro, E. *J. Phys. Chem. C* **2009**, *113*, 3352.

(17) Riktor, M. D.; Sorby, M. H.; Chlopek, K.; Fichtner, M.; Buchter, F.; Zuettel, A.; Hauback, B. C. *J. Mater. Chem.* **2007**, *17*, 4939.

(18) Riktor, M. D.; Sorby, M. H.; Chlopek, K.; Fichtner, M.; Hauback, B. C. *J. Mater. Chem.* **2009**, *19*, 2754.

(19) Fichtner, M.; Chlopek, K.; Longhini, M.; Hagemann, H. *J. Phys. Chem. C* **2008**, *112*, 11575.

(20) Harvey, K. B.; Mcquaker, N. R. *Can. J. Chem.* **1971**, *49*, 3272.

(21) Hagemann, H.; Gomes, S.; Renaudin, G.; Yvon, K. *J. Alloy Compd.* **2004**, *363*, 126.

Chapter 4 Summary and Future work

In this thesis, I studied the pressure effect on two hydrogen storage materials, i.e., ammonia borane ($NH_3 \cdot BH_3$) and calcium borohydride [$Ca(BH_4)_2$], by *in situ* vibrational spectroscopy. Several possible pressure-induced phase transitions were discovered for each compound, and structural stability and reversibility of these phase transitions were also examined. In addition, possible structures for different phases were discussed. Finally, the implications of their potentials in hydrogen storage application were proposed.

Although this study has provided substantial new structural information for $NH_3 \cdot BH_3$ and $Ca(BH_4)_2$ under high pressure, more detailed work need to be done. For instance, at the time when this thesis is being written, Filinchuk *et al.* has reported the structure of $NH_3 \cdot BH_3$ under pressure using X-ray diffraction, Landau theory, and *ab initio* calculations.[1] However, the structures of $Ca(BH_4)_2$ under different pressures remain unknown, and thus *in situ* high-pressure X-ray or neutron diffraction measurements are needed. In addition, both $NH_3 \cdot BH_3$ and $Ca(BH_4)_2$ were known to release H_2 via pyrolysis.[2-10] Therefore, the investigation of Raman and IR spectra as a function of temperature combined with pressure will greatly enhance our understanding of temperature-pressure-induced structural transformations and H_2 release that NH_3BH_3 and $Ca(BH_4)_2$ may undergo. Furthermore, by reacting with H_2 under high pressure, $NH_3 \cdot BH_3$ has been found to form a new hydrogen storage complex, i.e., $NH_3 \cdot BH_3$-H_2 which can store ~8 – 12 wt % more hydrogen than $NH_3 \cdot BH_3$.[11] Therefore, the synthesis of hydrogen storage materials similar to the $NH_3 \cdot BH_3$-H_2 system at high pressures should be explored in other systems, such as $Ca(BH_4)_2$-H_2. These systematic studies on $NH_3 \cdot BH_3$ and $Ca(BH_4)_2$ will aid the design and synthesis of new hydrogen storage materials.

References

(1) Filinchuk, Y.; Nevidomskyy, A. H.; Chernyshov, D.; Dmitriev, V. *Phys. Rev. B* **2009**, *79*, 732.

(2) Stowe, A. C.; Shaw, W. J.; Linehan, J. C.; Schmid, B.; Autrey, T. *Phys. Chem. Chem. Phys.* **2007**, *9*, 1831.

(3) Hu, M. G.; Geanangel, R. A.; Wendlandt, W. W. *Thermochim. Acta* **1978**, *23*, 249.

(4) Sit, V.; Geanangel, R. A.; Wendlandt, W. W. *Thermochim. Acta* **1987**, *113*, 379.

(5) Riktor, M. D.; Sorby, M. H.; Chlopek, K.; Fichtner, M.; Hauback, B. C. *J. Mater. Chem.* **2009**, *19*, 2754.

(6) Kim, J. H.; Jin, S. A.; Shim, J. H.; Cho, Y. W. *J. Alloy Compd.* **2008**, *461*, L20.

(7) Wolf, G.; Baumann, J.; Baitalow, F.; Hoffmann, F. P. *Thermochim. Acta* **2000**, *343*, 19.

(8) Baitalow, F.; Baumann, J.; Wolf, G.; Jaenicke-Rossler, K.; Leitner, G. *Thermochim. Acta* **2002**, *391*, 159.

(9) Baumann, J.; Baitalow, E.; Wolf, G. *Thermochim. Acta* **2005**, *430*, 9.

(10) Stephens, F. H.; Pons, V.; Baker, R. T. *Dalton Trans.* **2007**, 2613.

(11) Lin, Y.; Mao, W. L.; Mao, H. K. *P Natl. Acad. Sci. USA* **2009**, *106*, 8113.

Appendix

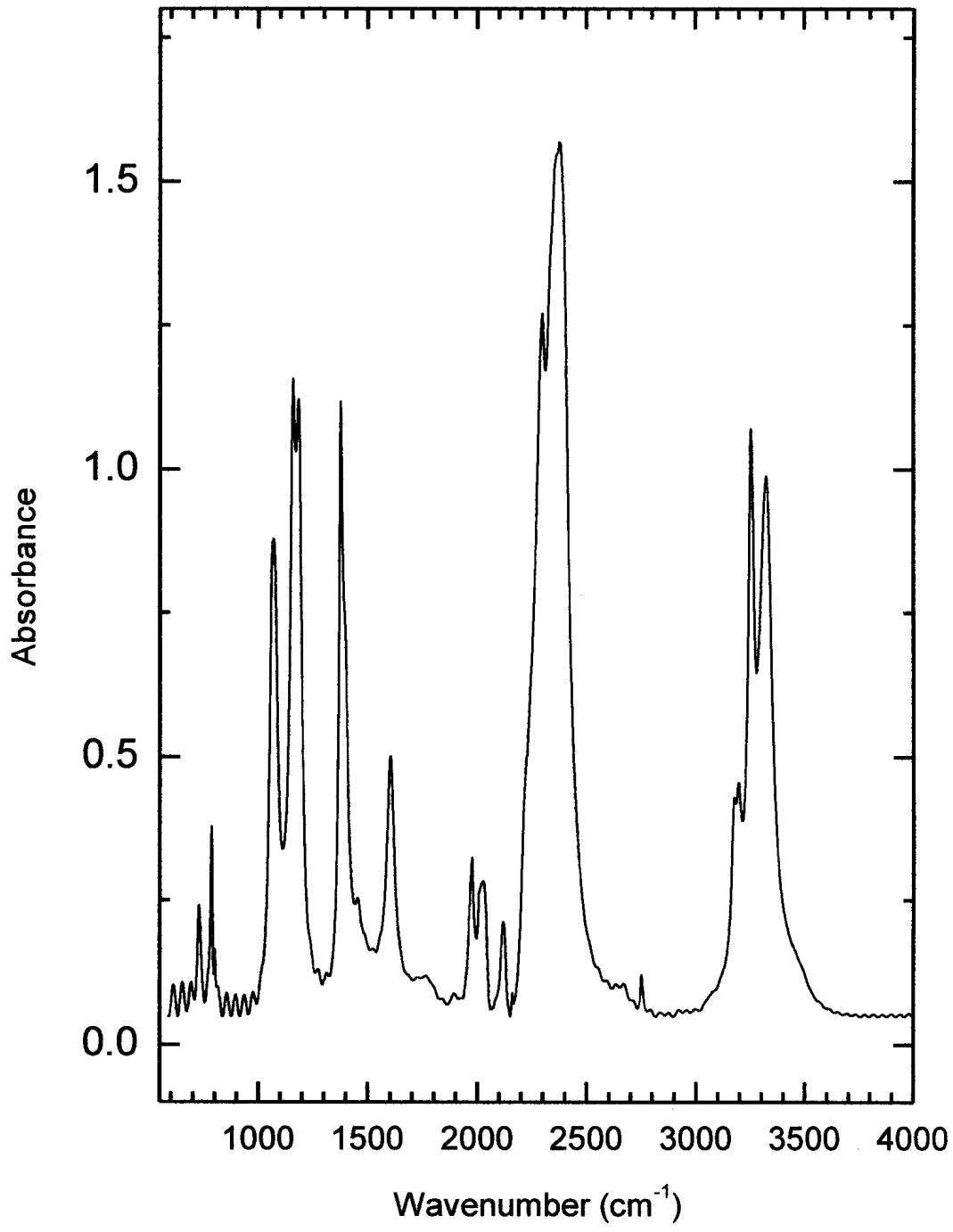

Fig. A1. Ambient-pressure IR spectrum of $NH_3 \cdot BH_3$ collected with the FTIR system in our lab in the region of 600 - 4000 cm^{-1}.

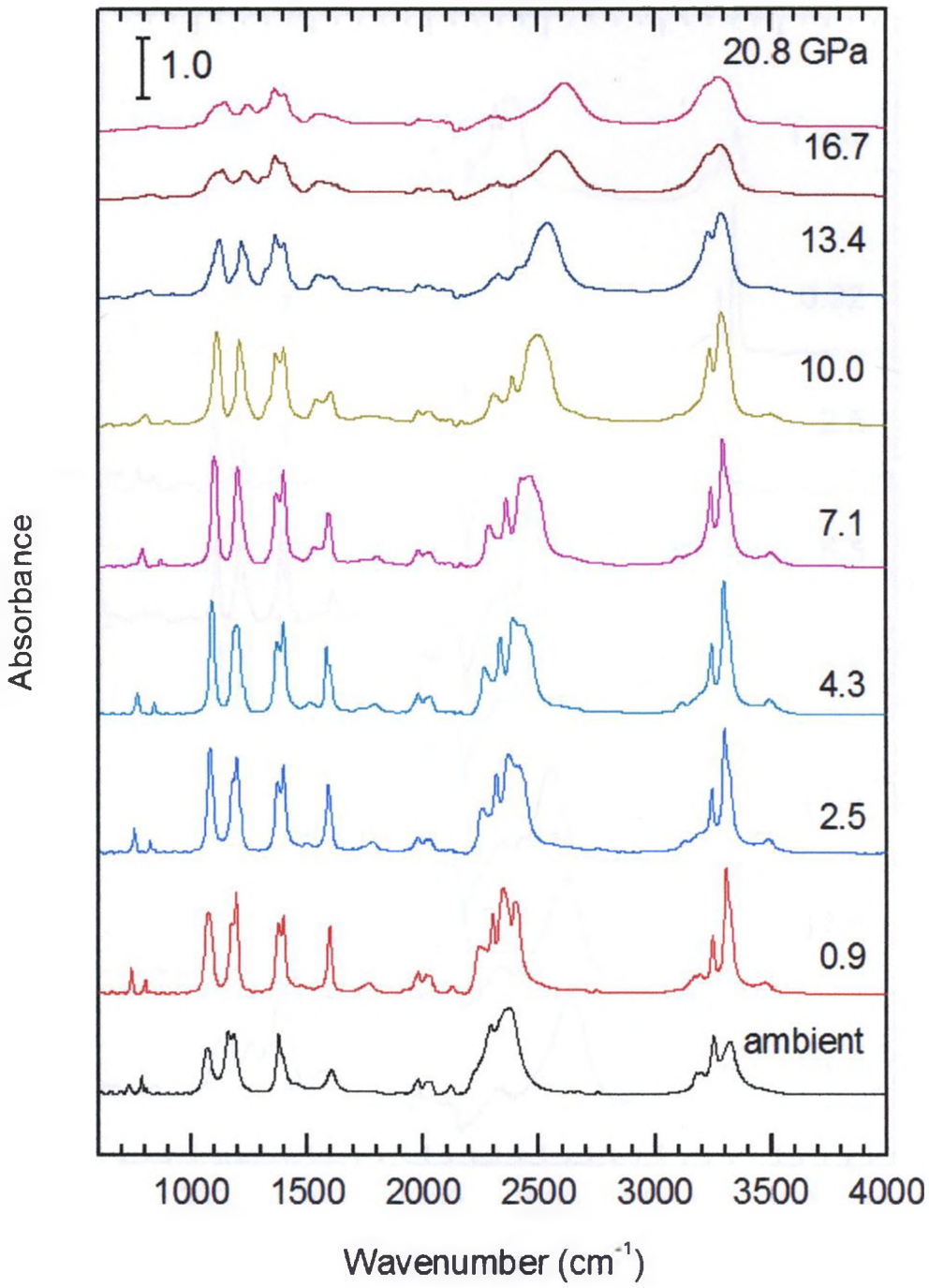

Fig. A2. Selected IR spectra of $NH_3 \cdot BH_3$ in the region of 600 – 4000 cm^{-1} on compression.

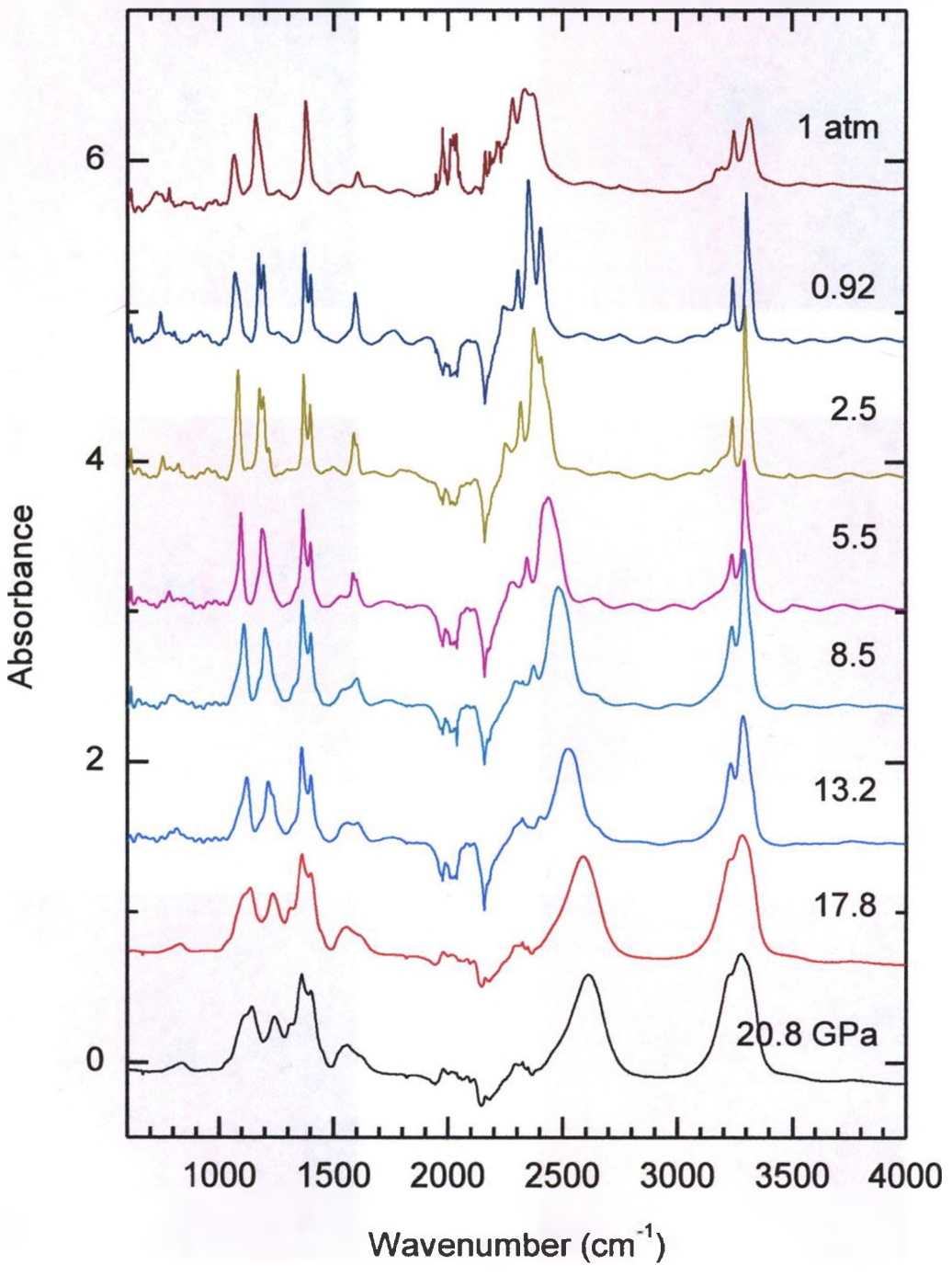

Fig. A3. Selected IR spectra of $NH_3 \cdot BH_3$ in the region of 600 – 4000 cm^{-1} on decompression.

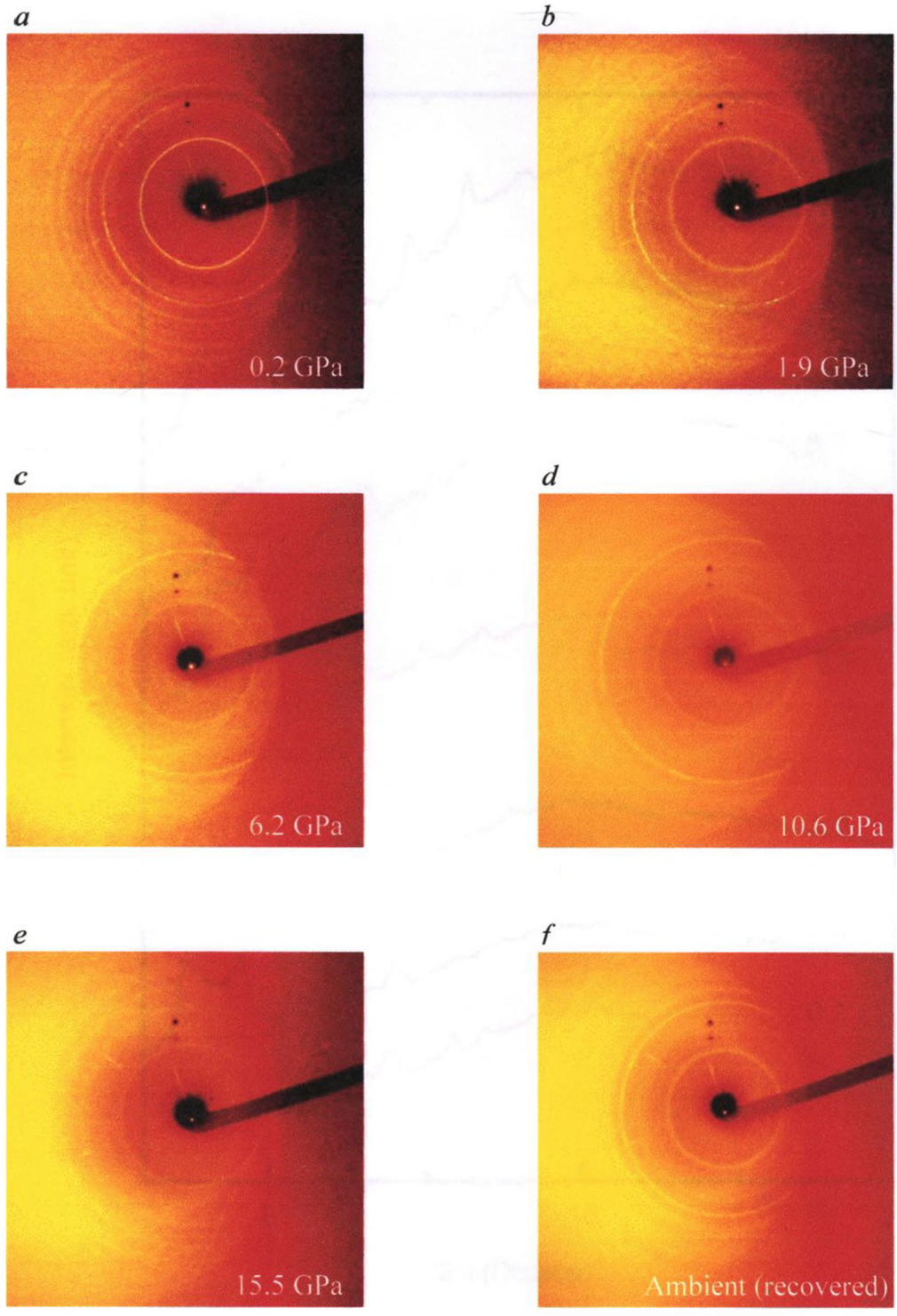

Fig. A4. Debye-Scherrer 2D X-ray diffraction patterns of $NH_3 \cdot BH_3$ on compression at pressure (*a*) 0.2 GPa, (*b*) 1.9 GPa, (*c*) 6.2 GPa, (*d*) 10.6 GPa, (*e*) 15.5 GPa and after decompression at pressure (*f*) ambient pressure.

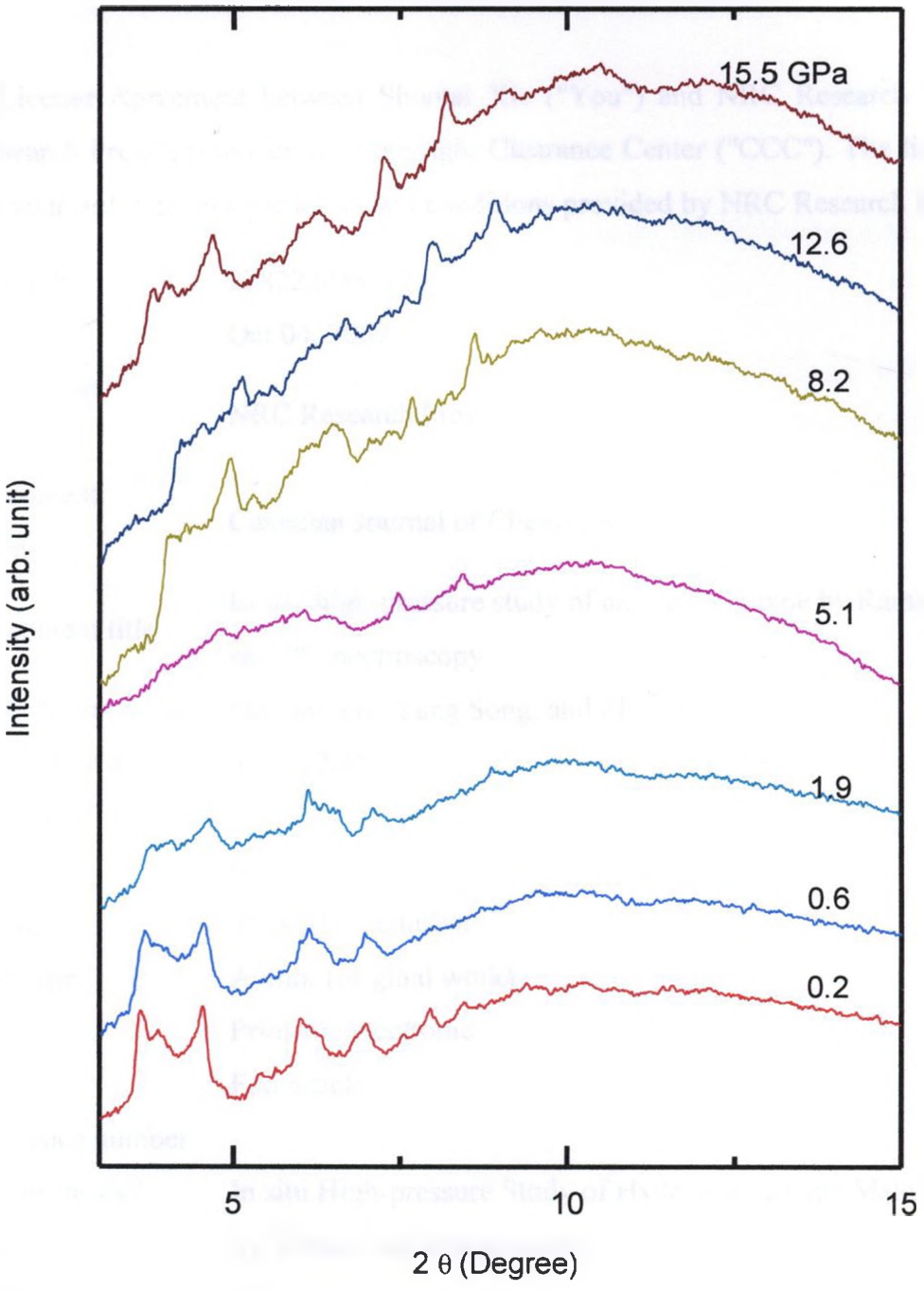

Fig. A5. 1D X-ray diffraction patterns of $NH_3 \cdot BH_3$ on compression. The pressure in GPa are labeled for each spectrum. The patterns are offset vertically for clarity.

NRC RESEARCH PRESS LICENSE TERMS AND CONDITIONS

This is a License Agreement between Shuntai Xie ("You") and NRC Research Press ("NRC Research Press") provided by Copyright Clearance Center ("CCC"). The license consists of your order details, the terms and conditions provided by NRC Research Press,

License Number	2282220469138
License date	Oct 04, 2009
Licensed content publisher	NRC Research Press
Licensed content publication	Canadian Journal of Chemistry
Licensed content title	In situ high-pressure study of ammonia borane by Raman and IR spectroscopy
Licensed content author	Shuntai Xie, Yang Song, and Zhenxian Liu
Licensed content date	Sep 1, 2009
Volume number	87
Issue number	9
Type of Use	Thesis/Dissertation
Requestor type	Author (original work)
Format	Print and electronic
Portion	Full article
Order reference number	
Title of your thesis / dissertation	In situ High-pressure Study of Hydrogen Storage Materials by Vibrational Spectroscopy
Expected completion date	Oct 2009
Estimated size(pages)	115
Total	0.00 USD
Terms and Conditions	

and the payment terms and conditions.

All payments must be made in full to CCC. For payment instructions, please see information listed at the bottom of this form.

General Terms & Conditions

Permission is granted upon the requester's compliance with the following terms and conditions:

1. A credit line will be prominently placed in your product(s) and include: for books the author, book title, editor, copyright holder, year of publication; for journals the author, title of article, title of journal, volume number, issue number, and the inclusive pages. The credit line must include the following wording: "© 2008 NRC Canada or its licensors. Reproduced with permission," except when an author of an original article published in 2009 or later is reproducing his/her own work.

2. The requester warrants that the material shall not be used in any manner that may be derogatory to the title, content, or authors of the material or to National Research Council Canada, including but not limited to an association with conduct that is fraudulent or otherwise illegal.

3. Permission is granted for the term (for Books/CDs-Shelf Life; for Internet/Intranet-In perpetuity; for all other forms of print-the life of the title) and purpose specified in your request. Once term has expired, permission to renew must be made in writing.

4. Permission granted is nonexclusive, and is valid throughout the world in English and the languages specified in your original request. A new permission must be requested for revisions of the publication under current consideration.

5. National Research Council Canada cannot supply the requester with the original artwork or a "clean copy."

6. If the National Research Council Canada material is to be translated, the following lines must be included: The authors, editors, and National Research Council Canada are not responsible for errors or omissions in translations.

v1.3

Gratis licenses (referencing $0 in the Total field) are free. Please retain this printable license for your reference. No payment is required.

If you would like to pay for this license now, please remit this license along with your payment made payable to "COPYRIGHT CLEARANCE CENTER" otherwise you will be invoiced within 30 days of the license date. Payment should be in the form of a check or money order referencing your account number and this license number 2275231115908. If you would prefer to pay for this license by credit card, please go to http://www.copyright.com/creditcard to download our credit card payment authorization form.

Make Payment To:
Copyright Clearance
Center Dept 001
P.O. Box 843006
Boston, MA 02284-
3006

If you find copyrighted material related to this license will not be used and wish to cancel, please contact us referencing this license number 2275231115908 and noting the reason for cancellation.

Questions? customercare@copyright.com or +1-877-622-5543 (toll free in the US) or +1-978 -646-2777.